Università degli Studi di Roma "La Sapienza"
Facoltà di Ingegneria

HIGH BRIGHTNESS ELECTRON SOURCE FOR COHERENT RADIATION PRODUCTION

Carlo Vicario

Dottorato in Elettromagnetismo

Coordinatore scuola:
Prof. Giorgio Gerosa

Tutor:
Prof. Luigi Palumbo

Commissione esaminatrice:

Prof. A. Sciubba Prof. B. Crosignani Prof. G. Schettini

Abstract

In this work, the main technological issues to produce an high brightness electron beam for x-ray Free Electron Laser (FEL) application are presented and analyzed. The researches conducted have been done as an R&D activities for the new SPARC photoinjector in Italy. The brightness of an electron bunch means high peak current and low beam's emittance. An UV laser and a photocathode is generally used to produce high density charge in an accelerating structure. To minimize the non-linear space charge forces a temporally square pulse on ps scale is needed. In this thesis we report the experimental results of pulse shaping obtained using an acousto-optic programmable dispersive filter and an high energy Ti:SA laser. Robust photocathodes, such as CVD diamond-based and Mg films, have been studied. Simulations, characterizations and installation of a magnetic chicane compressor is described. The experimental observation of an unprecedented ultra large bandwidth FEL radiation is reported and discussed.

to Barbara for her infinite
patience and continuous support

Contents

List of Figures

Chapter 1

Introduction

The Self Amplified Spontaneous Emission Free Electron Laser (SASE-FEL) are the most promising technique to generate the very intense X-ray radiation. SASE-FEL can have the optical properties characteristic of conventional lasers such as high spatial coherence and almost diffraction limited radiation beam. It differs from conventional lasers in using a relativistic electron beam as its lasing medium, as opposed to bound atomic or molecular states, hence the term free-electron. Because of the active medium, SASE-FEL does not have the limitations in maximum peak power and in short wavelength typical of the conventional laser.

The emitted radiation can be tuned changing the input electrons energy. Currently the FELs operate at wavelengths from millimeter to visible and near ultraviolet, potentially next future developments allow to extend the spectrum to x-ray. To have an efficient SASE-FEL operation, especially at short wavelengths, it is important the quality of the drive electron beam. The merit factors that define the electron bunch quality are low transverse emittance, high peak current and low energy spread. The beam quality is often described in term of brightness. This parameter is defined as the ratio between the peak current and the transverse normalized emittance of the electron beam. The brightness, practically, expresses the property of the electron beam to be focused in longitudinal and transverse directions.

The photo-injectors are the most widespread sources to produce high brightness electron beam. These injectors were introduced in the last two decades, and up to now their use has grown exponentially. The main reason is due to their capability to produce electron bunch with well-confined transverse and longitudinal distribution. The photo-injector's performances, in term of brightness, are several orders of magnitude larger respect to the injector based on other technology.

The scope of this thesis is the study of key issues for the production of high brightness electron beam. The framework of the activities is the SPARC project (Sorgente Pulsata Autoamplificata di Radiazione Coerente). The SPARC photo-injector will be constructed at LNF-INFN (Laboratori Nazionali di Frascati-Istituto Nazionale di Fisica Nucleare) with the aim to

verify some new solutions to minimize the emittance and to drive a SASE-FEL experiment. The FEL process, the photo-injector technology and the SPARC initiative will be described in the chapter 1.

According to the photo-injector scheme an high current beam is generated by a cathode when it is illuminated by an intense UV laser pulse. If the extracted charge is accelerated by high gradient radio frequency (rf) field and an emittance compensation scheme is adopted, the linear space charge forces can be effectively minimized.

The electron beam properties depend on the laser performances: charge, phase and position of the particles are directly related to the laser's energy, stability and reliability. Because the laser system can be synchronized with the rf system the electron can be extracted at a precise phase of the accelerating wave. The usual quantum efficiency of the cathode requires amplified laser source. The laser for high photo-injector application is a complex system that should be accompanied by diagnostics, optics and remote control. The chapter 2 is focused on the laser system scheme to drive the SPARC photo-injector. The laser adopted is a system composed by commercial available components based on the Ti:SA active medium. The laser's pulse specifications on the cathode are defined starting from practical considerations and from beam dynamic simulations. The requirements are very stringent and impose to integrate the laser system, with the design of the optical transfer line to the cathode and the diagnostic for online measurements and control.

Electron beam dynamics predicts that to minimize the non-linear space charge effect, the laser pulse should deliver to the cathode an hard edge uniform photon distribution in space and time.

The laser pulse shows naturally, gaussian or sech^2 temporal distribution and TEM_{00} transverse mode. Therefore an external manipulation should be applied. The transverse uniformity can be achieved using an aperture and a position dependent attenuation.

The longitudinal laser pulse intensity distribution, according to numerical simulations, must be top hat shape with rise and fall time shorter than 1 ps and flat top variable up to 12 ps FWHM. In the chapter 3 we report the results of pulse shaping obtained using an acousto-optic (AO) programmable dispersive filter (DAZZLER). The DAZZLER was used to perform spectral amplitude and phase modulation of the incoming 100 fs, 800 nm Ti:Sapphire pulses.

The preliminary studies has been conducted at the ULTRAS laboratoy of the Politecnico di Milano using the DAZZLER after a laser source. Because the pulse shaper has to be placed before the laser amplification and the ultraviolet conversion the device should pre-compensate the following distortions. This considerations motivated the successive experiment conducted at the Brookhaven National Laboratory (BNL). In this experiment the filter is placed before the amplification and the ultraviolet conversion.

In the photo-injector one of most critical component is the photocathode. In fact it does not exist a photocathode with enough high efficiency and robustness to high field and high laser power density. Moreover the photoemissive properties can be degraded by contaminants in moderate vacuum conditions. Finally cathode's dis-homogeneities and dark current cannot be always controlled. Worldwide photocathodes research and development programs are going on. In the chapter 4 we present the studies conducted on poly-crystalline diamond films synthesized by chemical vapor deposition with different dopants and various amount of carbonaceous species. The diamond films are very robust to high laser density and they can work for long time in poor vacuum conditions. An unusual linear relation between the emitted charge versus the incident laser energy has been observed and investigated. The major limit of these photocathodes is their low quantum yield when are stimulated by laser radiation at wavelength of 266 nm. This motivated the study of Mg films cathodes. The Mg is known to be a discrete emitter but showed limits on uniformity of emission, substrate adhesion and, beside, they have a very high velocity of contamination. This limits motivated the study of Mg film obtained by sputtering and by pulsed laser ablation (PLA). For the PLA films we tested a graphite termination as protective layer from contaminants. The results are reported in the chapter 4.

High electron beam brightness can be achieved by increasing the bunch peak current. To produce high current an electron beam shortening technique can be implemented. The charge pulse compression can be achieved by imposing to the electron beam an appropriate phase-energy correlation, and then drive the particles at the head of the bunch along a path longer than those at the tail. The position-energy correlation is introduced by acceleration of the beam off-crest of the rf wave. The control of the relative path lengths is carried out using the dispersion of a series of dipoles. In the chapter 5 we will describe the experiment on magnetic chicane compressor at the Accelerator Test Facility at BNL. The chicane has been constructed and it has been characterized by beam dynamics simulations.

The calculations conducted show that the chicane will significantly increase the beam brightness. The chicane will be integrated by electron beam diagnostic to study the compression process effectiveness and the coherent radiative phenomena associate with short pulse acceleration.

In the last chapter we report the measurements on the FEL radiation at the Visible-Infrared SASE Amplification (VISA) experiment at BNL. The measurements were done using an unusual electron beam compression mechanism. In fact, highly chirped electron bunch has been sent through the dispersive section that is used to share the beam to different beamlines. In this way we been observed a non-linear bunch compression and the produced FEL radiation showed a very large bandwidth. The very large bandwidth is

an interesting property and can be used to temporally compress the radiation pulse to tens of fs. We present the measurements performed on the electron beam, and the developed diagnostics for spatial and spectral characterization of the SASE radiation.

Chapter 2

Free electron laser and high brightness photoinjector

Free electrons laser (FEL) are the most promising new devices for creating very short wavelength coherent electromagnetic radiation. The FEL employs relativistic electron beams as its source of energy. Because quantum-based systems, i. e. the conventional laser, using bound electrons have limitations on both intensity (due to material breakdown) and minimum wavelength (due to available transition energies), the FEL is viewed as the most likely technique to development of "lasers" in the deep ultraviolet to X-ray range.

In this chapter we discuss the physics of the FEL process. The effective radiation production has to be accomplished using high brightness electron beam. In the following we review the FEL's requirements for the electron beam. The high brightness can be achieve only by using advanced electron source: the photo-injector. This machine provide generation, acceleration and manipulation of the electron bunch. We will recall the basis of the photo-injector theory and the features that make this source the essential requirement for producing high brightness beam. In the last part of the chapter we introduce the SPARC project(Sorgente Pulsata Autoamplificata di Radiazione Coerente)[1]. It consists of a series of parallel activities directed toward the realization in Italy of an X-ray FEL for the next decade. Because this thesis is intended to explore the key issues related to the high brightness electron beam production, we will focus only on the SPARC photo-injector and undulator.

2.1 Free electron laser theory

In order to understand the basic physical mechanisms upon which the FEL is based, we must first begin with undulator radiation, which is generated by an electron that performs small amplitude oscillations in a magnetic periodic structure: the undulator. The total power emitted by an electron as it oscillates in the undulator can be deduced from the synchrotron radiation

formula. For the purpose of this section, we simply state that the power emitted by a relativistic charge due to the transverse Lorentz force $\mathbf{F}_\perp$ is:

$$P = \frac{\gamma^2 q^2 \mathbf{F}_\perp^2}{6\pi\varepsilon_0 m_0^3 c^3} \tag{2.1}$$

where γ is the particle energy q_0 its charge, ε_0 is the vacuum dielectric constant c is the light speed in the vacuum. The emitted spectrum is broad-band and the angular emission is confined to an angle proportional to γ^{-1} in the particle motion direction.

However, the wavelength spectrum of the undulator radiation is quite different than the broad-band radiation characteristic of simple bend magnet excited synchrotron radiation. In the case of undulator radiation, the spectrum collapses to narrow bands about a certain undulator radiation frequency and its harmonics. Consider the emission of light of a given frequency $\omega_r = \mathrm{k}_r\mathrm{c}$ at a finite, small, angle θ from the electron at the first bend, refer to the Fig. 2.1. In order the radiation interfere constructively the wave-front emitted at the various bends should have a 2π phase shift:

$$k_r c(\cos\theta - \beta_z)t = 2\pi \tag{2.2}$$

Equation 2.2 indicates that the radiations phase front outruns the electron by one wavelength $\lambda_r = 2\pi/\mathrm{k}_r$ every undulator wavelength $\lambda_u = 2\pi/k_u$.

β_z is the longitudinal velocity if the particles and is expressed as:

$$\beta_z = 1 - \frac{1 + K_u/2}{2\gamma^2} - \frac{K_u^2}{4\gamma^2} cos(2k_u z) \tag{2.3}$$

In the follow we neglect the third oscillating term. For relativistic longitudinal velocities, small wiggle motion and $\theta \ll 1$, Eq. 2.2) can be expressed as:

$$\lambda_r \cong \frac{\lambda_u}{2\gamma^2}(1 + K_u^2 + (\gamma\theta)^2) \tag{2.4}$$

K_u is the undulator strength parameter expressed for planar magnetic field B_0 as:

$$K_u = \frac{qB_0}{\sqrt{2}k_u m_0 c} \tag{2.5}$$

where k_u is the wavenumber associated to the undulator period λ_u. Equation 2.4 indicates that the undulator radiation spectrum has a shift towards longer wavelengths for off-axis ($\theta \neq 0$) emission. However, as was stated above, most of the radiation intensity is located in angles $\theta < \gamma^{-1}$ and as such this effect, which may be named off-axis Doppler shift, does not introduce significant problems when one wishes to create nearly monochromatic photon beams from undulator radiation. Harmonics in the radiation appear

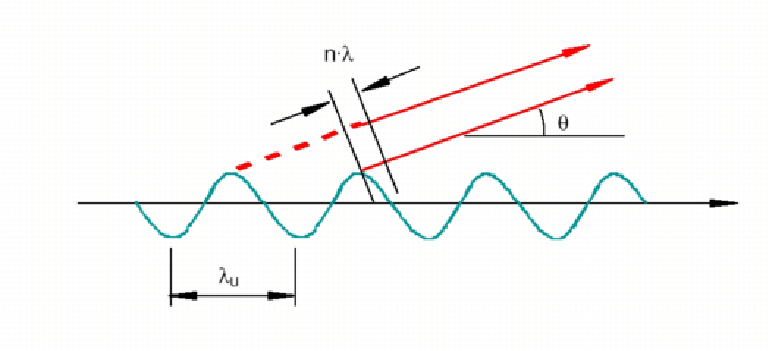

Figure 2.1: Picture of the FEL radiation production

due the fact that, for K_u=1 or larger, the transverse oscillation is relativistic in the beam frame, and therefore not simple harmonic. The resulting nonlinear motion contains Fourier components that have odd harmonics of the fundamental frequency λ_r. Thus, odd harmonics of the fundamental radiation wavelength (Eq. 2.4) are introduced into the emission spectrum. The strength of the harmonics is a function of K_u, and when this parameter is much larger than unity, large powers emitted in the higher harmonics is expected. Note that such harmonics appear for planar undulators, but not for helical undulators, where the transverse momentum is constant, and the problem of relativistic oscillations is avoided.

The physical picture of the how coherent light is amplified by a beam of electrons in an FEL is the follow. The beam of electrons is initially unbunched, having a spatial density distribution that is essentially uniform in z, the propagation direction. The interaction of the wiggling electrons with a light wave of correct wavelength λ_r causes the beam to bunch at a spatial periodicity equal to this wavelength. As the beam becomes increasingly well micro-bunched by this effect, the undulator radiation is enhanced because the phase relationship of the light emitted within a microbunch is constructive. In this scenario, the radiated electric field scales as N_μ, the number of particles in the microbunch, and the radiation intensity scales as N_μ^2 . This enhancement of radiated power at the appropriate wavelength λ_r obviously serves to strengthen the wave that caused the bunching interaction, and so a positive feedback system (or instability) is established. This feedback mechanism leads to exponential gain behavior, just as in a standard quantum level system laser.

For a low-gain system, realized by an FEL oscillator placed inside an optical resonator and fed by a pulse train of electron bunches synchronized to the round-trip frequency of the circulating photon pulse, the relative growth of the radiation field is small over the length of the interaction. In this case, the electron beam is injected slightly above the resonant value (for a specified injected light wavelength, $\gamma_0 \cong \sqrt{\lambda_u(1+K_u^2)/2\lambda_r}$), and the beam

undergoes roughly one half of a synchrotron oscillation, with most of the electrons ending up below the resonant energy. Even though the bunching induced is large, the growth in the radiated field due to the bunching is small.

However, in a very high gain system, the amplification of the field itself, with its associated longitudinal bunching of the electrons, takes place over a short time, roughly a quarter of a beam synchrotron oscillation period, $\int \omega_s(t)dt \cong \pi/2$. The field growth associated with this process turns on exponentially. In addition, the exponential growth of the field arises from the beam's radiation, and this causes a non-negligible phase shift in the total radiation. This phase shift allows the particles to lose net energy to the wave more effectively. In a system starting from noise in the spontaneous undulator radiation spectrum (self-amplified spontaneous emission, or SASE), there is no external signal that defines the amplified wavelength, it is simply that of the resonant undulator radiation. Thus, one would expect as many particles to absorb energy (accelerate) as radiate energy, and the gain to be therefore zero. The phase shift associated with the radiation process ensures that this does not happen, by shifting the phase of the wave continually backwards in the frame of the particles $z - v_\phi t$. At the point where small amplitude electrons have undergone approximately one-quarter of a small-amplitude synchrotron oscillation, the beam is as tightly bunched as it can be, and the high-gain FEL amplifier is saturated.

Free-electron lasers, in particular, those based on the high-gain SASE process, are of potentially enormous importance in future light source production. The fact that radiation can be tuned to arbitrary wavelengths by simply changing the beam energy means that existing electron linacs can be used to create FELs operating, in principle, from the millimeter to Angstrom wavelength regions of the spectrum.

X-ray lasers are naturally based on the SASE FEL concept, because there are no mirrors in the X-ray region to build a FEL oscillator, or no good sources of external signals for FEL standard amplifier.

2.1.1 SASE FEL requirements on the electron beam parameters

Here we discuss the requirements for the electron bunch to have an effective SASE FEL process. The electron beam parameters most critical to the FEL performance are transverse emittance, energy spread, and beam peak current. Other quantities, such as intra-undulator size and launching angle are, in general, adjustable with the beamline optics and steering magnets.

The beam transverse emittance is parameter that describe the quality of the electron bunch and is defined as:

$$\epsilon_q \equiv \sqrt{\langle q^2 \rangle \langle q'^2 \rangle - \langle qq' \rangle^2} \tag{2.6}$$

for q=x,y, and q' is the derivative of the transverse dimension respect

to the time and therefore, they are associated to the momenta in the transverse axes. Usually a general accepted way to express the emittance is the normalized form:

$$\epsilon_{n,q} = \gamma\beta\epsilon_q \tag{2.7}$$

Another often used figure of merit is the beam brightness [2]. A common definition is given by:

$$B_n = \frac{2 \cdot I}{\epsilon_{xn}\epsilon_{yn}} \qquad [\frac{A}{mm^2 \cdot mrad^2}] \tag{2.8}$$

where I is the peak current. The brightness is a practical measurement of the the ability of a beam to be focused. The energy spread defined as the dispersion of the particle energy around their nominal value $\delta\gamma/\gamma$ is another important properties for the FEL application.

For the FEL, among the parameter of most interest we find the so called ρ parameter [3, 4]. This parameter can be deduced from one dimensional Lorentz-Maxwell treatment of the electromagnetic interaction of the electron beam within an undulator structure. The ρ parameter determines the acceptance of the main electron beam and the photo-injector's parameter, and can be defined as follow:

$$\rho = \left(\frac{1}{64\pi^2}\left(\frac{K_u\lambda_u f_B}{\sqrt{2}\gamma}\right)\frac{I}{I_A\beta\epsilon_n}\right)^{\frac{1}{3}} \tag{2.9}$$

where I_A=17 kA is the Alfven current; ϵ_n is the normalized emittance, K_u and λ_u are, the undulator parameter and the magnetic period, γ is the relativistic factor, f_B is the decoupling parameter and β the beta function of the electron beam during the interaction with the undulator field.

The emitted SASE FEL wavelength can be expressed as the resonance condition, assuming stationary the undulator and the radiated field. The resonance condition is:

$$\lambda_r = \frac{\lambda_u}{2\gamma^2}\left(1 + \frac{K_u^2}{2}\right) \tag{2.10}$$

In the case the electron beam emittance and energy spread is negligible this is the resonant wavelength. In the real SASE FEL the radiated wavelength shifts to a value slightly larger than the resonant λ_r. Anyway the Eq. 2.10 fixes the electron beam energy requirements. To produce short photon wavelengths, high electron energy is required. Because accelerating gradient is limited by the breakdown in the accelerating structure, Xray FEL experiment has to be driven by large machine. It is important to point out that the main difference with the conventional lasers is that the wavelength is continuously tunable by changing the beam energy.

One important parameter depending on ρ is the gain length,

$$l_g = \frac{\lambda_u}{4\pi\sqrt{3}\rho} \tag{2.11}$$

for a mono-energetic beam, this quantity expresses the radiated power P(z) exponential grown in the propagation along the undulator z:

$$P(z) = P_0 e^{\frac{z}{l_g}} \tag{2.12}$$

The FEL exponential gain is defined as the undulator length L in units of the gain length, is:

$$\tilde{L}_u = \frac{L}{l_g} = \frac{4\pi\rho L}{\lambda_u} = 4\pi\rho N_u \tag{2.13}$$

The peak power of the FEL saturation scales with ρ:

$$P_{sat} = \rho P_{beam} \tag{2.14}$$

where $P_{beam}[GW] = I_p[A]E[GeV]$ is the electron power. In this sense the ρ parameter is referred as the FEL energy conversion efficiency. In addition the beam relative energy spread should be smaller than ρ, to don't depress the SASE process. The Eq. 2.11, 2.13 and 2.14 show that to produce shorter gain length, higher exponential gain and efficient SASE process the ρ parameter should be set as high as possible. From the definition of the ρ parameter it is clear that the higher peak current and low normalized emittance are conditions that have to be pursued. Moreover, according to the one dimensional treatment, to obtain SASE operation at a given wavelength the following condition should be fulfilled:

$$\epsilon_n < \frac{\lambda_r \gamma}{4\pi} \tag{2.15}$$

This equation leads to a direct, crude estimation of the emittance requirement. It is clear that the operation at short wavelength imposes more challenging requirements on the emittance. A final issue that has to be consider is the influence of the diffraction on the field. If the analysis is extended to the tridimensional effects we get the same results except for the normalized emittance. In fact the emittance's requirement become more stringent:

$$\epsilon_n \leq \begin{cases} \frac{\lambda_r B^{1/3}}{4\pi} & for B \geq 1 \\ \\ \frac{\lambda_r B^{1/2}}{4\pi} & for B \leq 1 \end{cases} \tag{2.16}$$

where B is the so-called diffraction parameter and is defined as the ratio between the Rayleigh length and the gain length 2.11: $B = l_R/l_g$. Fortunately, the SASE positive interference process occurs not on the total length of the bunch but on the so called cooperation length.

$$L_c = \frac{\lambda_r}{2\rho_{3D}} \tag{2.17}$$

Therefore the Eq. 2.16 fixes the requirement locally and the emittance for a slice of the bunch becomes the most important parameter. We refer to a local emittance as the slice emittance.

ρ_{3D} is the saturation parameter defined as:

$$\rho_{3D} = \frac{\Gamma \lambda_u}{4\pi} \tag{2.18}$$

where Γ is the gain parameter [5] whose definition is:

$$\Gamma = \left(\frac{8\pi^2 f_B^2}{\gamma \lambda_u} \frac{I_p}{I_A} \frac{K^2}{1 + K^2/2} \right)^{1/2} \tag{2.19}$$

The efficiency of the SASE process at the saturation $\eta_{sat} = P_{sat}/P_{beam}$ is given as function of the saturation and the diffraction parameters by:

$$\eta_{sat} \cong \begin{cases} \rho_{3D} B^{-1/3} & for B \geq 1 \\ \\ \rho_{3D} & for B \leq 1 \end{cases} \tag{2.20}$$

To obtain the maximum efficiency and reduce the undulator length it is necessary to focus the electron beam to provide a value for the diffraction parameter B$\cong$1. When decreasing the electron beam size, i.e. reducing B, the requirements on the value of the energy spread become less severe, as shown in the equation:

$$\frac{\delta\gamma}{\gamma} \leq \begin{cases} 0.5 \cdot \rho_{3D} B^{-1/3} & for B \geq 1 \\ \\ 0.5 \cdot \rho_{3D} & for B \leq 1 \end{cases} \tag{2.21}$$

To summarize the results of this section we can state that the effective SASE-FEL process requires high ρ parameter. The requirements are therefore, low normal emittance and high peak current. These requests are especially stringent to obtain the short wavelengths operation. The high current can be achieved with several compression techniques and we will present the compression based on magnetic chicane. The importance of the high current is shown in Fig. 2.2 where it is reported the simulated SASE gain versus different slice's current for the SPARC FEL [1]. The simulation tool is the numerical code GENESIS [6]. As shown in the figure higher current produce the gain saturation within shorter length.

2.1.2 Status of the SASE FEL experiments

Most of the theoretical understanding of SASE-FEL process, partially summarized in the previous section, had been developed during 1980s [3, 7]. However, significant experimental progress did not follow until a decade later. The main reason for the delay was the stringent requirements on the quality of the electron beam necessary for an effective single pass SASE amplification.

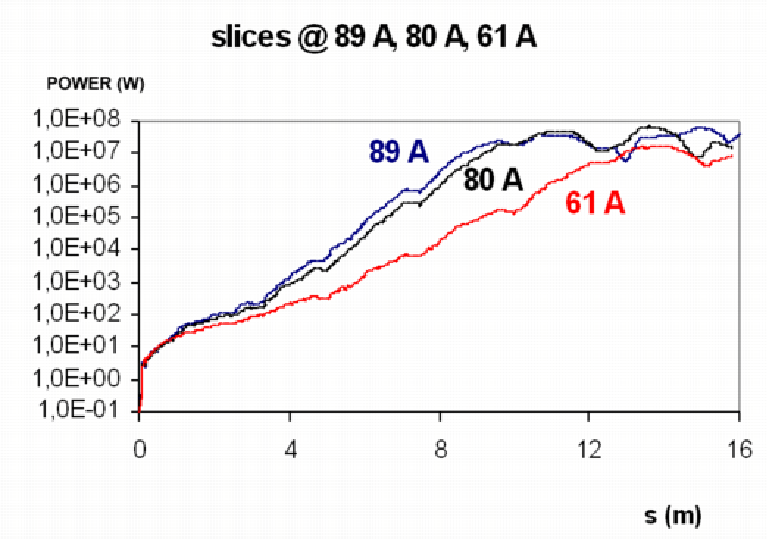

Figure 2.2: Genesis simulation of the gain versus the position in the undulator for three different current for the SPARC SASE-FEL.

The required beam brightness exceeded the capabilities of thermionic guns, and only the invention of photo-injector based electron beam sources [8], followed by the development of emittance compensation methods [9, 10, 11], enabled the transformation of the SASE FEL field into experimental science.

Using photo-injector sources, experimental work at UCLA [12] and BNL [13] reported observation of SASE signal at 16 m and 1.2 m respectively. In 1998 at LANL, gain of 300 was achieved at 15 m [14]. In the same year, in a LANL/UCLA experiment [15] a SASE gain of larger than 10^5 was reported at 12 m, providing the FEL community with the data on SASE intensity, fluctuation and spectral properties. In the same experiment, electron beam microbunching was observed directly by evaluating the coherent transition radiation at the FEL fundamental frequency, emitted by the electron beam from a target after the undulator [16]. The next set of experiments was designed to expand SASE FEL techniques to lower wavelengths, aiming to test the feasibility of proposed X-ray FEL projects [17, 18]. In the LEUTL experiment, at Advance Photon Source (Argonne National Laboratory), a SASE FEL saturated at 530 nm, for the first time, and later on at 385 nm wavelengths [19]. At BNL, an alternative approach to achieve short wavelengths, by high gain FEL harmonic generation, was studied experimentally [20]. The FEL program at DESY [21] advanced SASE wavelength into deep UV at 109 nm, and recently achieved saturation at the wavelength of 93 nm. The VISA experiment has demonstrate SASE FEL operation at near-infrared wavelengths, with saturation in less than 4-m using low emittance electron beam [22]. The high brightness beam is key factor to push the emitted wavelengths toward the X-ray. The SPARC design and construction is directed to the study of high brightness beam issues and a SASE FEL experiment at

530 nm [23].

2.2 Photo-injector to generate high brightness electron beam

The photo-injector was introduced in 1985 [8] and from that time its use has grown exponentially. The main reason is due to its capability to produce transversely and longitudinally well-confined electron beams. The operating principle of a photo-injector is very simple: electron bunches are generated by laser pulses illuminating a photocathode. The photoemitter is installed inside an RF gun structure where the charge is extracted and violently accelerated by an electric field. At the gun exit the beam is boosted to high energy in a linear accelerator structure.

In general an electron injector can be considered as a machine that perform three successive operations on the electron beam: extraction, acceleration and manipulation of an electron bunch. We will discuss the photo-injector advantages respect to the traditional injectors within these three steps.

2.2.1 Photo-injector theory

We will provide a quick overview of the photo-injector beam dynamics. A basic theory has been proposed by Kim [10]. In this theory we consider the beam properties of a simple rf gun consisting of n+1/2 cells with a pure sinusoidal accelerating field. No transverse solenoid focusing is included. The longitudinal accelerating field envelope is expressed by:

$$E_{acc}(z) = E_0 cos(kz) sin(2\pi ft + \phi_0) \tag{2.22}$$

where k is the rf wave number and z the longitudinal coordinate. Under the assumption that there is no beam expansion and that the bunch is short compared with the rf wavelength, Kim derived an analytical formula for the main beam parameters. If ϕ_0 is the phase of the central particle in the bunch when it leaves the cathode its asymptotic phase at the gun exit is expressed by:

$$\phi_\infty = \phi_0 + \frac{1}{2\alpha sin(\phi_0)} \tag{2.23}$$

where α is a dimensionless parameter representing the strength of the accelerating field given by:

$$\alpha = \frac{eE_0}{2mc^2k} \tag{2.24}$$

e is the electron charge and m its mass. Kim shows that the minimum emittance and the maximum energy are obtained when:

$$\phi_\infty = \frac{\pi}{2} \tag{2.25}$$

To obtain the expression for ϕ_∞ it is assumed that the electron energy increase very rapidly near the cathode. The condition of validity of the Eq. 2.25 has been demonstrated [31] to be equivalent to:

$$\alpha \geq 0.9, \qquad \phi_0 \geq \frac{\pi}{4} \tag{2.26}$$

This conditions give a value of 2 for the relativistic factor γ which corresponds to $\beta = v/c = 0.9$. Thus the physical meaning of the condition above is that the electron should be relativistic before reaching the middle of the first cell. Kim provides the analytical formula for the emittance in the assumption of short bunches and gaussian distribution in the transverse and longitudinal directions. The emittance can be defined as the contributions of the space charge, the radio frequency field and the thermal emittance of the cathode.

$$\epsilon = \sqrt{\epsilon_{sc}^2 + \epsilon_{rf}^2 + \epsilon_{th}^2} \tag{2.27}$$

The thermal emittance is an intrinsic parameter of the beam and depends on the the photocathode's work function and the drive laser radiation wavelength. It will discussed on the chapter 4, which is dedicated to the photoemission. Here we can state only that it represents a sort of theoretically minimum for the emittance. Other emittance contributions that are not explicitly expressed are caused by electromagnetic field cylindrical asymmetry and by magnetic field component at the cathode [32]. The Kim's theory shows that the space charge emittance ϵ_{sc} and the radio frequency emittance ϵ_{rf} ca be expressed as:

$$\epsilon_{sc}(\phi_0) = \frac{c^2}{8\alpha f sin(\phi_0)} \frac{I}{I_A} \frac{\sigma}{3\sigma_x + 5c\sigma} \tag{2.28}$$

$$\epsilon_{rf} = 4\sqrt{2}\pi^3 c^{-1} \alpha f^3 \sigma_x^2 \sigma \tag{2.29}$$

being σ the rms bunch length and σ_x the rms transverse size. I is the peak current and I_A, as said before is the Alfven current.

According to the Eq.2.28, 2.29 and the definition in Eq. 2.24 it is clear that ϵ_{sc} and ϵ_{rf} term compete with each other respect with the accelerating field gradient, because the space charge term scale as $1/E_0$ and the rf term as E_0. In principle the rf term cannot be compensated and its contribution is smaller compared to the space charge contribution.

2.2.2 Electron extraction

The traditional electron extraction process is based on the thermionic effect. In this source the emission is stimulated by heating an appropriate cath-

ode material. This effect is simply the escape of the electrons with higher energy from the emitting surface of the cathode. Integration of the Fermi-Dirac distribution over particle with a velocity perpendicular to the emitting surface yields the expression for the thermionic current, for instance see reference [24]. The emitted charge shows long temporal distribution and very large thermal emittance. The bunch length is controlled by accelerating and manipulating scheme. For instance if the emission is stimulated by a radio frequency field the electron are emitted over the half-wave where the positive field. In principle, in a DC gun the emission extends on an indefinite time and to bunch the electrons it is often used a triode gun where the emission was controlled by a pulsed high voltage between a grid and the cathode. Depending on the solution adopted and on the acceptable emittance, the pulse length was limited from tens to hundreds of ps [26].

The main consequence is that, in the thermionic injector the current density is limited to density of 100 A/cm^2 [25]. The lower normalized emittance produced of a beam from a thermionic cathode is 6 π mm-mrad with bunch charge of 1.2 nC [27].

In the photo-injector the charge's extraction is based on the photoelectric effect. A laser pulse illuminating a photocathode can stimulate the charge emission with a precise duration and at a well defined time. Nowadays solid state lasers represent a consolidated technology to generate reproducible picoseconds and sub-picoseconds electron pulse. Moreover the laser pulse can be synchronized within less than 1 ps respect to a proper phase of the RF accelerating field. By photoemission effect it is possible to produce a current density at least four orders of magnitude greater than thermionic emission up to 10^5 A/cm^2 [28]. As discussed in the following the thermal emittance is very low and is fixed by the photons' energy and the photocathode bands structure.

Using the photo-injector higher current density and lower emittance can be achieved. The best achieved brightness values are in the range of 10^{13} A m^{-2}rad^{-2} in an operational photo-injector, refer to [29] for instance. While the thermionic sources performances are limited to few 10^{10} A m^{-2}rad^{-2}.If the electric field is strong enough to cancel the space charge forces, a very high brightness density is achievable, up to $5 \cdot 10^{15}$ $A \cdot m^{-2} \cdot rad^{-2}/cm^2$ [30].

2.2.3 Electron beam acceleration

The space charge effect are generated by the Coulomb repulsive forces inside the electron bunch and contributes to emittance growth. The effect of the the space charge is especially harmful at low energy. Therefore to obtain high charge density it is important to accelerate the bunch with high electric field. Particle acceleration techniques fall simply into categories: DC acceleration, in which the beam moves in a constant potential gradient, and RF acceleration, in which the beam is driven by an electromagnetic wave slower than light velocity . The disadvantages of the DC system are low accelerating

gradient and the difficulty of working with high DC voltage. Pulsed DC are implemented by complex acceleration scheme but are not able to produce pulses shorter than 1 ns. The radio-frequency is the preferred technology to produce high gradient high brightness beam. According with the application of the photo-injector normal or superconductive technology can be adopted. The superconductive structures allows long radio-frequency pulses up to hundred of μs or even in CW and therefore they can achieve high average current. Their drawback are a peak field limited to 35 MV/m. In the normal conductive photo-injector peak field up to 125 MV/m has been reached [17]. Their disadvantage is the that the RF pulse is limited to few μs. Normal conductive photo-injector are low duty cycle high brightness machine.

2.2.4 Beam manipulation

The space charge is the net effect of the Coulomb repulsion forces that acts between the electrons within the bunch volume. It is useful adopt the phase space representation to describe the emittance dynamics during the bunch propagation. The field can be expressed as function of the particle distribution. If we don't consider to collision between the electrons the beam dynamics is governed by collective effects and the bunch can be assimilated to a series of slices. The emittance is equal to the integral of the slices' contributions.

For an indefinitely long uniform cylindrical distribution the produced field is proportional to the radius and the force produced by the single slice is constant along the longitudinal direction z. To compensate the space charge therefore contrast the beam expansion a constant magnetic field can be used. Instead for an uniform distributed electron bunch with finite length σ_z the radial field is the contribution of the single slices and the peak field is located at the central slice. The non-uniform field distribution produce a defocusing stronger at the central position in the bunch. The radial field is still linear with the radial dimension. In the transverse phase space picture the slices are segments and the propagation induces a rotation that is different for each slices. These radial linear space charge forces applied to different longitudinal slices in the beam lead to a fan-like behavior of the transverse phase space.

In 1987 Carlsten propose a scheme to align the different slices of the electron beam in such a fashion to minimize the transverse normalized emittance of the beam [9]. The technique is termed "linear space charge emittance compensation". If properly implemented, this technique can effectively counteract emittance growth generated primarily by the linear space charge emittance dilution processes.

Space charge emittance compensation is a three step process which involves a drift and one solenoid. The transverse phase space distortion is reversible with careful selection of drift length and focusing parameters. Because optical component induce a kick to the particles proportional to their

radial position the central slice suffers a stronger focus than the outer slices and the transverse phase space tends to reduce its area. As the beam passes through another drift, the radial space charge forces eventually counter the negative radial momentum that was previously imparted on the beam by the lens.

Following a drift a particle which has experienced higher radial forces due to being in the dense center of the bunch, has acquired more radial momentum and has consequently been pushed further out radially than a particle on the edge. The beam propagation induce successive oscillations of the emittance.

On the other hand if the beam is now accelerated as it approaches the radial minimum (the waist of the beam), where the emittance itself is minimized, this emittance can effectively be maintained due to γ^{-2} dependence of the space charge forces. The generalization of this model to the case of a beam which is accelerated after the drift has been developed by Serafini and Rosenzweig [11]. They provide an analytical solution to achieve emittance compensation.

A new working point very suitable to damp emittance oscillations has been recently found [33] and adopted by several new high brightness photo-injector [1, 17, 34]. By a proper choice of rf gun and solenoid parameters, the emittance evolution shows a double minimum behavior in the drifting region. If the booster is located where the relative emittance maximum and the envelope waist occur, the second emittance minimum can be shifted at the booster exit. Additional compensation of the space charge is obtained with distributed solenoid around the first acceleration stage [1] In the Fig. 2.3 is reported the simulated emittance and beam envelope for the SPARC photo-injector performed with HOMDYN code [49]. In the case of the linear acceleration is placed at the emittance local maximum the emittance and the envelope are minimized at the linac exit. For comparison it is reported also the case when the beam propagate without acceleration at the gun exit.

It is important to note that the space charge compensation technique only reverses the effects of radially linear forces.

The non-linear space charge effect arises when the beam density is not uniform. Laser beam display naturally a gaussian temporal profile and a TEM_{00} bi-dimensional spatial intensity. The emitted charge reproduces the laser's photon tridimensional distribution. To compensate the non-linear space charge it would be needed a non-existent optical component with non-linear focusing. The not linear space charge effect compensation can be correct only by manipulating the spatial and temporal profile of the photocathode drive laser pulses. The transverse manipulation techniques are reported in the following chapter. The time domain laser pulse manipulation is extensively described in the chapter 3. An R&D program has been started to produce the uniform density temporal pulse and the experimental results are reported in the following.

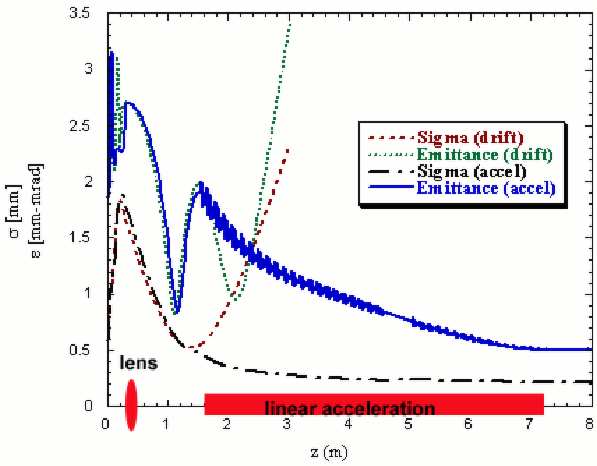

Figure 2.3: HOMDYN simulation of SPARC injector transverse rms beam size and normalized emittance, in two TW linac configuration. Thermal emittance of 0.3 mm-mrad is assumed; additional focusing is provided around the first linac.

2.3 The SPARC project

In March 2002 the SPARC proposal, born from a collaboration among ENEA, INFN, CNR, University of Rome "Tor Vergata", Sincrotrone Trieste and three units of the INFM. The SPARC project has been started with the aim to explore the scientific and technological issues for the construction of short wavelength source. The project is a long term initiative devoted to the realization in Italy of a coherent X-ray SASE-FEL in the next decade.

The overall SPARC project consists of four main lines of activity directed towards several goals. These activities are: an advanced photo-injector, a SASE-FEL experiment, the development of X-ray dedicated optics and a soft X-ray compact source. We quickly describe the four activity and then more details will be provided on the photo-injector design and the FEL experiment.

150 MeV Advanced Photo-Injector

Since the performances of X-ray SASE-FEL's are critically dependent on the peak brightness of the electron beam delivered at the undulator entrance, this activity was conceived with the purpose of investigating two main issues:

- generation of a high brightness electron beam by means of an innovative scheme of space charge compensation, able to drive an FEL-SASE experiment at 530 nm [23].

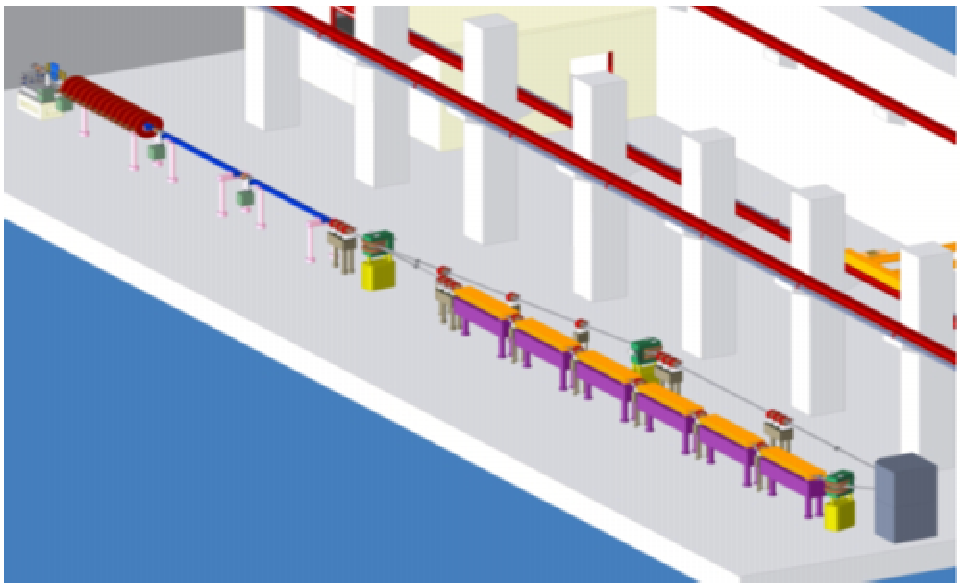

Figure 2.4: SPARC machine layout in the LNF bunker

- generation of a ultra high brightness, high peak current beams, via RF and/or magnetic compressors, suitable for future X-Ray sources.

The first task was given the priority inside the project, and forms what we will refer to as SPARC Phase 1. Nevertheless, the latter task is of strategic importance for the development of ultra-brilliant electron beams for future short wavelength FEL.

This activity is performed under the responsibility of INFN (Instituto Nazionale di Fisica Nucleare). At the moment the design of the accelerator is almost concluded and the acquisition of the hardware components is going on. The machine will be constructed at the National Laboratory in Frascati of the INFN . The SPARC layout and the bunker where it will be constructed are shown in fig 2.4.

SASE-FEL Visible-VUV Experiment

The SASE-FEL experiment within the SPARC initiative foresees:

- performance of a SASE FEL experiment with the 150 MeV photo-injector-derived beam, using a segmented undulator with additional strong focusing, to observe FEL radiation at 530 nm and at below [36];
- investigation of the problems related to matching the beam into an undulator and keeping it well aligned to the radiation beam, as well as the generation of non-linear coherent higher harmonics.

X-ray Optics/Monochromators

Radiation emitted from an X-ray FEL will provide photon beams to users that are unique in terms of peak brightness and pulse time duration (100 fs). Such beams pose severe challenges in implementing the optics necessary to guide and handle the intense radiation. This project will pursue also an R&D activity on the analysis of radiation-matter interactions in the spectral range typical of SASE X-ray FEL's (from 0.1 to 10 nm), as well as the design of new optics and monochromators compatible with these beams.

Soft X-ray table-top Source

In order to test the optics developed for X-ray SASE FEL sources, and to begin R&D on ultra-short X-ray-based applications, the project will undertake an upgrade of the presently operated table-top source of X-rays at INFM-Politecnico Milano. This source will deliver 10^7 soft X-ray photons in 10-20 fs pulses by means of ultra-high harmonic generation of an ultra-fast intense laser pulse in a gas [37].

Beams with the features anticipated in the SPARC project are also of strong interest for beam physics experiments into other cutting edge research fields. The SPARC injector may allow investigations into the physics of ultra-short beams, plasma wave-based acceleration, and production of X-ray Compton back-scattering [38], [39].

This thesis will focus on the first two activities, descriptions of technical components will be given only for the photo-injector and undulator.

2.3.1 SPARC photo-injector layout

The proposed system to be built consists of: a 1.6 cell RF gun operated at S-band (2.856 GHz, based on the BNL/UCLA/SLAC gun design) [32], and high peak field on the cathode (120 MV/m) with incorporated metallic photo-cathode (Copper or Mg). The gun will generate a 5.6 MeV beam which will be properly focused and matched into 3 accelerating sections of the SLAC type (S-band, travelling wave) which accelerate the bunch up to 150 MeV.

The production of high brightness electron beams in the photo-injector requires that a temporally-flat, picosecond laser source be used to drive the photo-cathode. The square pulse can be obtain performing a manipulation in the spectral domain. The laser system driving the photocathode will therefore employ high bandwidth Ti:Sa technology with the oscillator pulse train locked to the RF. The Ti:Sa mode locked oscillator and amplifiers able to produce the requested energy per pulse (500 μJ at 266 nm) are commercially available. Instead the pulse manipulation device and its integration

on the laser system require a dedicated activity of research and development. For frequency manipulation, we plan to use a liquid crystal mask in the Fourier plane of the non-dispersive optic arrangement or a acousto-optic programmable dispersive filter (AOPDF). To obtain the desired time pulse shape we have conducted preliminary tests on the AOPDF in order to produce the 10 ps long flat-top shape. In the following chapter 3 we will extensively discuss this point reporting also some experimental results.

The SASE FEL experiment will be conducted using a permanent magnet undulator made of 6 sections, each 2.13 m long, separated by 0.36 m gaps, and including single quadrupoles which focus the electron beam in the horizontal plane. The undulator period is set at 3.0 cm, with an undulator parameter $K_u = 1.4$. A simulation performed with GENESIS numeric simulation code, shows the exponential growth of the radiation power at 530 nm along the undulator; almost 10^8 W can be reached after 14 m of total undulator length . Preliminary evaluations of the radiation power generated into the non-linear coherent odd higher harmonics show that 10^7 and $7{\cdot}10^5$ W can be reached on the third and fifth harmonics, respectively [1].

A second beam line is under design to by-pass the undulator, thus allowing experiments on magnetic pulse compression. In particular in next development of the SPARC photo-injector it is foreseen to investigate emittance degradation due to CSR (Coherent Synchrotron Radiation)[43] and the surface roughness wake-field effects .

The radio frequency gun

The RF photocathode gun and the associated systems are meant to reliably produce, at the most critical point in the injector, the extremely high quality beam demanded by the SPARC photo-injector. A critical accompanying component is the photocathode drive laser. The design and the construction of the electron gun is made by the UCLA Particle Beam Physics Laboratory. The gun will be a copper rf structure at 1.6 cavity cell with the high-gradient working at 2856 MHz (according to the design developed in at BNL/SLAC/UCLA)[32].

We discuss below the overall philosophy of the gun design, and details of the design including photocathodes, gun manufacturing and tuning methods, and the emittance-compensation solenoid design that allows for flexibility not only in the focusing strength of the magnet, but in its longitudinal center.

The parameters of the SPARC RF gun are summarized in the table 2.1. These parameters are consistently derived from both previous experience at existing labs that have used versions of the 1.6 cell gun ,and from detailed numerical simulations [1].

The maximum power foreseen for exciting the gun (15 MW) is based on this maximum quoted field 140 MV/m while the present plan for SPARC running is only at the 120 MV/m level. This peak power yields an average power at the design duty cycle (repetition rate limited by the laser system)

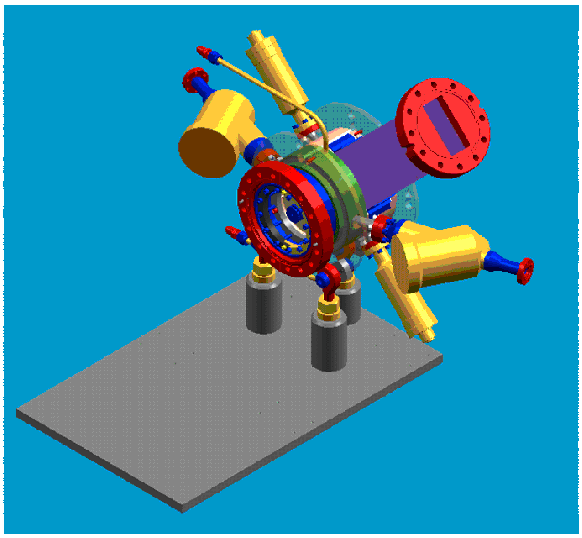

Figure 2.5: 3D-dimensional rendered drawing (rear view) of ORION version of the 1.6 cell RF photocathode gun and related vacuum and waveguide components and ports. All access flanges removed for viewing purposes. (courtesy D. Palmer, SLAC)

Parameter	Value	units
Peak electric field on cathode	120-140	MV/m
Beam pulse duration (FWHM)	3-12	ps
Output energy	7	MeV
Frequency	2856	MHz
Repetition (max)	10	Hz
RF pulse duration	4.5	μs
RF peak power	15	MW
RF average power	700	W
Temperature	45	°C
Vacuum (RF on)	10^{-9}	Torr
Cathode insert diameter	12	mm
Laser spot diameter	2	mm
Cathode material	Cu(Mg)	
Q.E. at λ=266 nm	$10^{-5}(10^{-4})$	electrons/photons
Charge	1	nC
Laser incidence angle	72	deg
Peak solenoid field	3.1	kG
Solenoid current (with cooling on)	200	A
Solenoid dissipation	4	kW

Table 2.1: SPARC rf-gun operating parameters

which is well within the standard 1.6 cell gun design thermal handling capabilities. The quantum efficiency (QE) of the Cu and Mg photocathode has a wide built-in safety margin. In fact the assumed QE is lower than the data reported in literature.

Figure 2.5 shows a schematic 3D rendered drawing of the most recent generation of 1.6 cell S-band RF gun, a model developed for the ORION project that corrects some known deficiencies in previous performance of the original BNL/SLAC/UCLA version. The RF power waveguide, visible on the upper right, is coupled to the full cell, and vacuum is pumped through a symmetrizing port. Also symmetrically placed in the full cell are the two frequency tuners, at 90 degrees with respect to the waveguide (the upper one is visible), and the entrance and exit laser ports, half way between waveguide and the vacuum ports. The beam exit port is on the front of the picture.

The symmetry of the structure determines that of the electromagnetic field distribution avoids dipolar excitation components; the lowest perturbation of the RF mode is limited to quadrupole components, with negligible effect on the beam dynamics.

The photocathode is inserted in the center of the flange that terminates the half-cell. In the first phase of the project it is planned to use a single-crystal Cu cathode insert, a material with well proven photo-emissive behavior that guarantees good uniformity and high field operation. Its drawback is the low emission efficiency, which entails large laser pulse energy. The Mg cathode foreseen for use in the later phase of the project has larger emission efficiency but lower distribution uniformity, it is more difficult to handle and it supports lower electrical gradient [17].

Some studies on the quantum efficiency of the magnesium cathode will reported in the following. The measurement were done on Mg film. Film synthesis technique assure more control on the uniformity of emission and could improve the adhesion on the copper substrate.

Both types of cathodes demand very good vacuum, at the level of 10^{-9} Torr during the rf-gun operation. These demands are to be met by stringent control of the gun manufacturing process, and by implementing as much pumping systems on the gun as possible. The vacuum pump are installed through the direct pumping port, through the waveguide, at the beam port, and behind the cathode plate through an array of small pumping holes.

The laser injection can be done from the 70° port o from the electron beam output port, see fig. 2.5. We choose to use the first solution because it has demonstrated to produce higher cathode quantum efficiency [40]. This scheme, as discussed later, requires wavefront correction of the laser pulse. It has the advantage to simplify the beam-line downstream of the RF gun, allowing more room for pumping and beam diagnostics. Moreover the laser injection from the beam output port require a mirror that is source of wake-fields on the electrons and compromise the beam emittance.

The SPARC gun is similar to the ORION version of the 1.6 cell gun shown in fig. 2.6. This version represents a recently implemented effort to improve

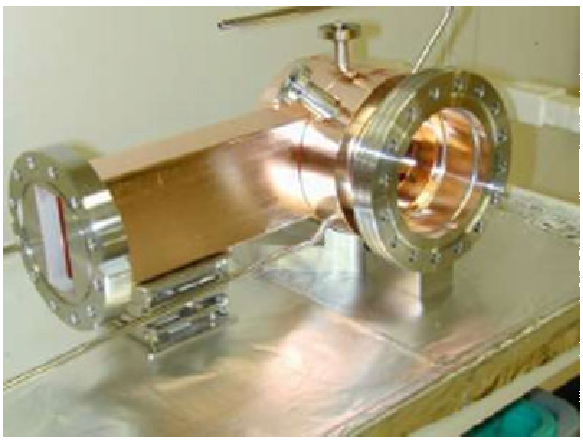

Figure 2.6: UCLA Neptune spare RF gun after recent (10/02) final brazing at SLAC.

the performance of the device. By using brazed-on stainless steel holding rings to attach to a three-point kinematic support, much more rigorous control over the electromagnetic axis is obtained.

The emittance compensation solenoid The RF gun is followed by the emittance-compensation solenoid, as shown for the ORION case in Fig. 2.7. The solenoid assembly is a large, multi-coil (8 pancake device) with field-stiffening inserts and a large yoke. For the SPARC project it has been decided to explore a new solenoid design. The reasons for this change are both in the SPARC beam dynamics experimental program, which requires the possibility of adjusting the longitudinal position of the solenoid field, and in practical construction considerations. The most compelling feature of this new design is the adjustability of the longitudinal position of the lens center, by introducing unequal currents in each coil, linearly ramping them up or down. The current gradient can produce a shift of over 2.2 cm in the center of the lens for the relatively modest asymmetry in the coil currents [1]. Introduction of this type of tunability by physically moving the entire heavy solenoid assembly was studied, but the adopted scheme was found to be more flexible, and more robust from the viewpoint of maintaining gun EM axis to solenoid magnetic axis alignment.

Accelerating structure

After the rf gun, post-acceleration is provided by two travelling-wave constant-gradient accelerating guides operating at 2856 MHz and composed by 86 cavity cells coupled in the $2\pi/3$ electromagnetic mode. These accelerating sections are known as the SLAC-type structures. To reach the required nominal energy of 150 MeV, the accelrating section must provide at least 72 MeV each whit a field gradient of 25 MV/m. This is a rather high value for the

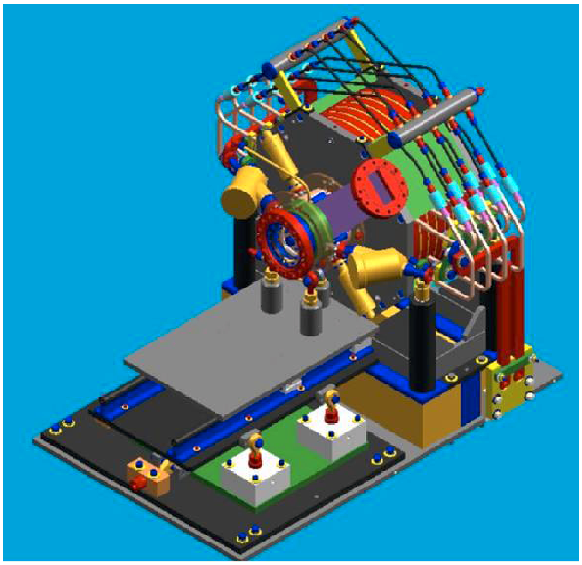

Figure 2.7: 3Dimensional drawing of the SPARC gun including the magnetic solenoid and the alignment system

SLAC-type sections, and as such demands careful manufacturing, excellent internal surface finishing and cleaning treatments, and good vacuum performance. The beam loading is negligible due to the very small average beam current (energy extracted by the beam is 70 mJ per section, the average stored energy in each section is 50 J).

The linac will be feeded by two klystrons as high power RF power sources. These sources can generate RF pulses of 45 MW saturated power for 4.5 sec at 50 Hz. The modulators must generate pulses of 100 MW peak and 4.5 sec flat-top (310 kV-330A) at the repetition rate of 10 pulse per second. The SPARC linear accelerator will work under ultra-high vacuum condition (P$\sim 10^{-7}$ Pa). The electron beam parameter at the linac exit are summarized in the table 2.2.

The SPARC machine will be integrated with diagnostics of the electron beam properties: charge, energy, energy spread, beam trajectory and transverse distribution. Particular attention will be devoted to low energy emittance measurement. This measurement will be done with the aim to reconstruct the emittance oscillation as predicted by the simulation [41]. This task will be accomplished using a movable system. At high energy the emittance will be diagnosed with the quadrupole scan technique. The temporal distribution of the beam will be based on some new ideas as the radio frequency deflector [42] and the interferometric measurement of the coherent transition radiation [43].

Electron beam parameter	Value	units
Beam energy	155	MeV
Bunch charge	1.1	nC
Repetition rate	10	Hz
Frequency of the accelerating structure	2856	MHz
Peak solenoid field	0.273	T
Central RF launch phase	33	degree
Laser pulse duration flat top	10	ps
Laser pulse rise time	1	ps
Laser spot size at cathode	1.13	mm
Bunch peak currrent at linac exit	100	A
rms transverse normalized emittance at linac exit	<2	mm-mrad
rms slice (300 μm) norm. emittance	<1	mm-mrad
rms longitudinal norm. emittance	1000	deg-keV
rms total correlated energy spread	0.2	%
rms incorrelated energy spread	0.06	%
rms beam spot size at linac exit	0.4	mm
rms bunch length at linac exit	1	mm

Table 2.2: SPARC nominal electron beam parameters at the linac exit.

Chapter 3

The SPARC Laser system

3.1 Introduction

Laser to drive the photocathodes for high brightness electron beam applications must show very specific capabilities driven by two major considerations: the low photo-emission efficiency for robust photocathodes requires high UV pulse energy; the emittance compensation process is most successful with uniform temporal and spatial laser energy distribution. More demands are placed on the longitudinal (time) laser profile by the requested capability of changing the pulse length over a range from 2 to 12 ps to control the charge and peak current. Additionally, low amplitude and time jitters from pulse-to-pulse, as well as pointing stability are needed to assure repeatable SASE-FEL performance. The laser pulses have to be synchronized with the radio frequency master oscillator, in order to extract electrons at the specified phase of the RF accelerating wave. The requested features restrict the choice for the source at the solid state amplified laser.

In this chapter we will define the SPARC laser specifications starting from beam dynamics simulations with the aim to verify as non ideal laser pulse features influence the electron beam's properties. In the next section we describe the laser's technical features to meet the requested performances. The laser chosen is a commercially available system. Anyway it should be noted that an external device, that in the following is named as pulse shaper, is needed to achieve the required temporal laser distribution. The pulse shaper requires a dedicated experimental program and it will be extensively discussed in the next chapter.

Because the laser system will be placed in a dedicated environment several meters far from the gun, an optical transfer line is needed. This transport should be capable to preserve as much as possible the radiation quality coming out the source. The laser and the transfer line should be integrated by a diagnostics and control system that allows to remotely control the most important attributes of the laser pulse up to the cathode.

3.2 Laser system specification and tolerance study

The drive laser supplies photons that are absorbed by electrons within the RF gun cathode, producing via the photo-electric effect electrons if the absorbed energy exceeds the material's work function. The energy required can be calculated when the photocathode quantum efficiency (QE) is known. The quantum efficiency is defined as the number of emitted electrons divided by the number of incident photons. A cathode's quantum efficiency depends on many conditions, such as material, preparation, excess of photon energy over the work function, RF field and vacuum levels. The emission threshold for metallic photocathode is between 4.2 and 4.6 eV, and therefore a UV light is required. Usually, from practical considerations the photon energy is set at 4.66 eV with wavelength of 266 nm. This wavelength can be produced by non-linear optical phenomena using the harmonics generation crystals, see for instance [44].

In the SPARC photo-injector the nominal charge is 1 nC, and therefore assuming a QE of 10^{-5} for the copper cathode the required energy is 500 μJ. This required value at the photocathode, must be considerably larger at the harmonic-generator's exit, as light will be absorbed by various optical elements needed for pulse transport an manipulation to the photocathode. Beside the harmonics generator has typically efficiency on the order of 10-20%, therefore the energy requirement in the fundamental harmonic becomes tens of mJ. The QE value assumed is less than the data reported in the literature but in the energy budget we preferred to over-specify the laser performance. The energy jitters from pulse to pulse should be avoid because they induce charge and, therefore, space-charge variations and change the matching conditions. To achieve reproducible SASE-FEL performances the energy jitter has to be limited at less than 5% rms. The SPARC photo-injector repetition rate is 10 Hz and sets the laser system pulse repetition.

Recalling the previous discussion, the need to minimize nonlinearities in the space charge field of the electron bunch, in particular at low energy, leads to a request for generating uniform cylindrical photoelectron distribution. This result is confirmed by numerical simulations [1] and experiments [45] that have demonstrated the uniform spatial and temporal laser distribution produces lower emittance than the natural gaussian temporal and TEM_{00} transverse mode. Because metal photocathodes have a temporal response on the femto-seconds scale the electron temporal distribution is controlled by the laser pulse. On the other hand the spatial charge uniformity comes out from the combination of an uniform laser intensity and the cathode homogeneous QE.

To obtain cathode material with uniform photoelectric properties, special care should be devoted on the cathode preparation, on the surface cleaning and on the control of the surface damage during the operation. Single crystal

copper cathode is often used for its absence of defects in the bulk and on then surface. In the chapter 4 we will describe the experiment conducted on Mg films deposited with the aim of increase QE uniformity. A study on the on the effects of cathode's non homogeneity is reported in a recent works [46] [47]. The transverse laser intensity can be obtained by using an iris to filter out the tails of the expected TEM_{00} mode. Perhaps besides the iris, it is possible to use an inverse gaussian filter to improve the laser uniformity. The iris should should be imaged to the cathode with the Fourier relay imaging, as are discussed in the following section.

In order to define in details the operational performances of the SPARC laser system we carried out beam dynamic simulations. Using the PARMELA [48], HOMDYN [49] and TREDI [50] codes we have investigated the effects of non-ideal characteristics of the laser pulse on the emittance growth. The correlation between the emittance performance and the variation from ideal parameters were studied in details. A definition of the tolerances on the laser beam attribute such as energy jitters, elliptical laser spot on cathode, and time jitters, has been done.

Cathode non-uniformity study The transverse photoelectron uniformity at the cathode surface is an important parameter. Here we present some simulations that model the laser or cathode not uniformity as a variation of the QE. The effects of cathode's inhomogeneities have been simulated using TREDI numerical code. The calculations assumed a circular off-center "hole" of depressed QE, with a surface $S \approx 10\%$ of the nominal spot on the cathode. The results suggest that this kind of localized inhomogeneities does not dramatically degrade the emittance, that grows by 10% and 15% for hole QE degradation of 50% and 70% respectively. In the real cathode the non homogeneities are likely random distributed spots and they increase due to hot spots of the laser beam or the high power density used for the activation process.

Effects of the laser elliptical spot on the cathode As said before to improve the QE and to preserve the electron beam quality we chose to inject the laser at 72° respect to the cathode's normal. For off-normal incidence the circular laser becomes an ellipse on the cathode, losing the symmetry with the electric field in the gun. To compensate this effect a cylindrical lens can be used. The analysis was done with the aim to quantify the influence of an eccentric ($\alpha = \sigma_x/\sigma_y \neq 1$) laser spot on the cathode on the beam quality at low energy. The simulations were made with the three dimensional TREDI Monte Carlo code shows that the beams may not be significantly out of round. The results indicated that $\alpha = 1.2$ causes a qualitative change in the emittance compensation dynamics at low energy.

A numerical study of the effect of the laser spot ellipticity on output beam emittance at high energy has been done using the PARMELA code.

Calculations for an elliptical cross section input beam have been performed for different values of the ratio of the two semiaxes of the ellipse in order to preserving the beam density. One can see that for $\alpha \leq 1.1$ the emittance compensation process still works in both planes, while for larger values the emittance control is lost.

From these results we can conclude that in order to keep stable control of the beam emittance in both planes and to limit the emittance degradation with respect to the symmetrical case to 15%, the transverse ratio of the laser spot should not to be larger than 10%.

Definition of the time profile requirements As said before the emittance minimum can be obtained using a square pulse. The square or flat top pulse's quality is individuated essentially by two important parameters: the rms rise or fall time defined as the time the pulse profile goes from 10% to 90% of its maximum and viceversa, and, the ripples that account the oscillations' depth on the top of the pulse. The target pulse is symmetric and therefore in the following when we talk about the rise time we implicitly refer also to the fall time.

PARMELA simulation on the effects of non zero rise-fall has been performed starting from a thermal emittance of 0.3 mm-mrad, a peak field on cathode 120 mV/m and a magnetic field 0.27 T.

The simulations reported in Fig. 3.1 refer to an optimized temporal pulse length of 11.65 ps FWHM, they show that the normalized projected emittance deteriorates as the laser pulse rise time increases. As results from these studies, flat top pulses with rise times shorter than 1 ps are required in order to avoid noticeable emittance degradation. Slice emittance analysis points out that the SASE saturation is achieved within the foreseen 10 m undulator length for 81% of the beam for 1 ps rise-fall time, and 94% in the case of no rise time.

As discussed in the upcoming chapter 3, laser pulse shaping with short rise time may result in the formation of longitudinal ripples due to the limited bandwidth of the optical signal. Therefore, the effect of a laser pulse with longitudinal ripples has been investigated and compared to a plain square pulse with no ripples. We have performed simulations with a temporal pulse length of 11.65 ps FWHM, 1 ps of rise time and we have assumed the presence of uniform distributed ripples of 30% ptp (peak-to-peak) of the nominal amplitude. The beam is assumed to be transversely uniform in these studies. The striking result is that even with a 30% of longitudinal irregularity the beam emittance does not appear to be strongly affected. This result is displayed in Fig. 3.2, where it is evident that the presence of ripples does not affect either the emittance or the rms transverse beam envelope. At the end of the photo-injector (8 m), with a 1 ps rise and fall time, the emittance grows to 1 mm-mrad, which still an acceptable value. The effect induced by the ripple is almost negligible because the density's modulation in the

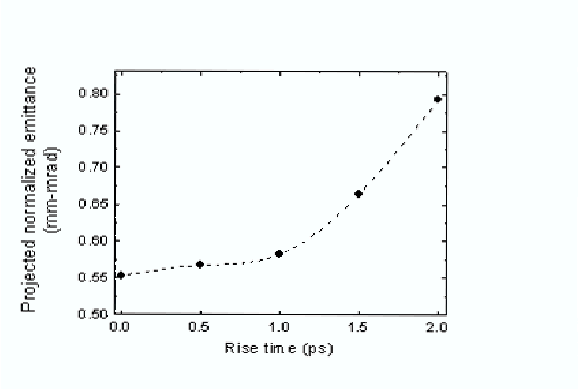

Figure 3.1: Study of the effect of the laser pulse's rise time on the normalized emittance dilution. For the calculation thermal emittance of 0.3 mm-mrad, an electron beam of 1 mm radius and uniform transverse distribution are assumed

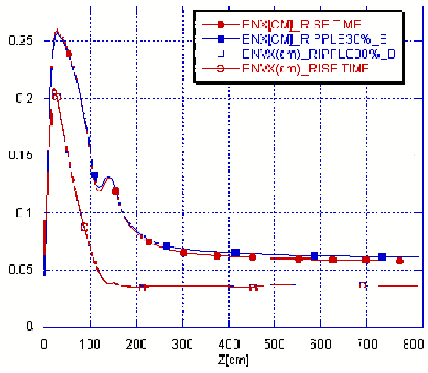

Figure 3.2: Study of the effect of the laser pulse's ripple on the normalized emittance and beam envelope: with (blue squares) and without (red dots) 30% amplitude ripples.

electron bunch is compensated by the space charge effect that brings it back to an uniform longitudinal distribution. The crucial parameter seems the fast rise time. The compensation induces a modulation of the energy in the electron slices. Energy modulation can be more deleterious in the future developments of the SPARC photo-injector when a compression of the beam is foreseen.

Phase jitter Synchronization between laser and accelerating wave is needed to control the electron beam charge, the energy spread and the matching condition in the accelerator. The variation of the output rms normalized emittance with the laser-to-gun jitter phase indicate that for 4 RF phase degree (about 4 ps) variation the projected emittance growth is 4% for a uniform longitudinal distribution and rises to 6% for a 1 psec rise time pulse. From these results we can conclude that a tolerance of 2° around the optimal phase is acceptable in order to limit the emittance growth to less than 10%. The issue of timing jitter becomes more critical when one considers magnetic and velocity bunching, however.

Pointing stability analysis The long optical transport line of the UV radiation from the laser room to the photo-cathode may produce a misalignment of the beam that gives rise to cathode illumination jitter. The centroid's random position induces a pointing instability and divergence on the electron beam at the entrance of the SPARC undulator. The estimated maximum undulator acceptance respect to the beam position is 60μm. In addition the beam divergence at the entrance of the undulator has to be less than 57 μrad to prevent walk-off in the undulator. It should be noted that the electron beam acceleration and transport can magnify the original misalignment at the cathode. A preliminary study of this effect has been done by the code HOMDYN, it indicates that initial centroid offsets of 33μm and 100 μm becomes at the undulator entrance 40 μm and 120 μm with a divergence of 20 μrad and 65 μrad respectively. The simulation puts a stringent requirement for the pointing stability introduced by the laser system and the optical transfer line: the acceptable offset is 33μm.

In the table 3.1 we summarize the requirements for the laser parameters on the photocathode. Some of this parameters like the energy, temporal stability pointing stability are worsen by the long optical transfer line from the laser system. Therefore the performances required are more challenging.

3.3 Laser system description

To achieve simultaneously the energy level the pulse duration and the stability summarized in table 3.1 the only laser sources that can be adopted

Parameter	**Requirement**
Operating wavelength	266 nm
Pulse energy (for QE=10^{-5})	500μJ
Energy jitter (in the UV)	5% rms
Temporal pulse profile	Uniform (30% ptp)
Pulse rise time	<1 ps
Transverse distribution	Uniform (30% ptp)
Pulse duration	2-12 ps
Repetition Rate	10 Hz
Laser-RF jitter	< 2ps rms
Spot diameter	2.26 mm
Ellipticity $\alpha = \sigma_x/\sigma_y$	<1.1
Pointing jitter	33 μm

Table 3.1: SPARC laser system requirements

are those based on solid state active medium. The photon's energy required impose the use of higher harmonics generation starting from the fundamental wavelength centered in general in the near IR region.

The pulse time profile produced by commercial laser system has generally gaussian or Lorentian distribution. As reported in the next chapter, to generate the target profile and external device is required. The high resolution required in time implies a broad spectrum. In the last decade the technology of ps and sub ps laser was consolidated and today Ti:Sa, Nd:glass and Nd:YAG laser represent a reliable photon sources to drive a photocathode in an high brightness photo-injector. The limitation of the Nd:YAG laser system is in the very narrow bandwidth less than 0.5 nm, more than an order of magnitude smaller than the value needed for obtaining the necessary rise time. The glass based lasers have on the other hand a larger spectral components but, because the glass has a thermal conductivity one order of magnitude lower respect to crystal, these systems don't achieve very reliable performances at the high energy required in the SPARC case [44].

The optimum choice that we have found for satisfying the required laser performances is to use a commercial, frequency-tripled Ti:Sapphire laser. In fact the Ti:Sa ($Ti{:}Al_2O_3$) crystal is able to produce a bandwidth large enough to perform the time pulse shaping, and can support the high energy required in SPARC application [51, 52]. The Ti:Sa crystal has the optical absorption peak between 490 and 540 nm, which sets the pump requirements. Flashlamp or diode pumping is very difficult to achieve in Ti:Sa because a very high pump flux is required. The reason for that is the short life-time fluorescent time, about 3.2 μs [44]. Commercial Ti:Sa laser at the beginning were pumped with Argon laser but in the recent year it is preferred to employ frequency double Nd:YAG or Nd:YLF for pulsed or CW operation. Moreover

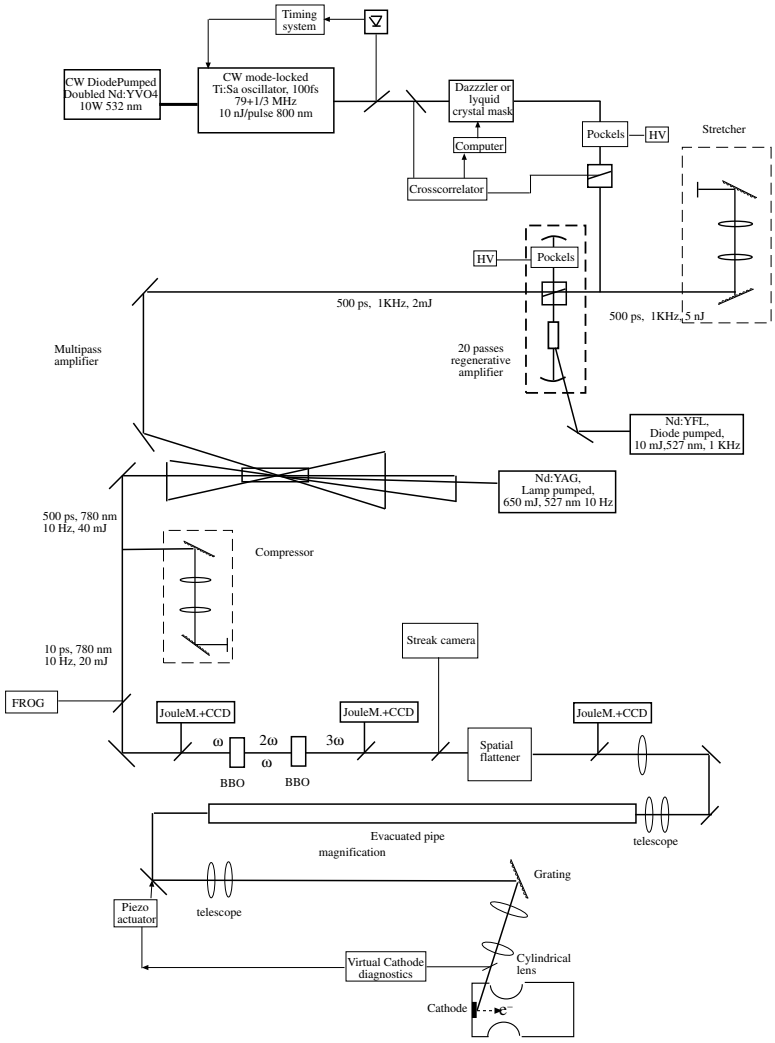

Figure 3.3: SPARC laser system conceptual layout

the new available Nd-based laser pumped by diodes improved the stability of the pumps and therefore of the Ti:Sa systems.

The emitted wavelength can be tuned with optical filters or narrow bandwidth mirror on the large fluorescence band of the material (700 to 1100 nm) but the most efficient wavelengths are between 780 and 800 nm. The bandwidth of the emitted pulse depends on the set-up of the oscillator cavity. Since the duration of the emitted pulse is inversely proportional to the bandwidth, the Ti:Sa laser is capable of producing pulses from 10 fs to picoseconds scale.

The proposed layout for SPARC [53] laser consists of a frequency-doubled CW 10 W diode-pumped $Nd:YVO_4$ to pump the Ti:Sa oscillator, see Fig. 3.3. The oscillator is chosen to work in a mode locking regime at 800 nm, with 100 fs transform-limited pulses and therefore a bandwidth of about 10 nm. The typical energy per pulse is 10 nJ at the exit of oscillator. The repetition rate of the oscillator is chosen by varying the cavity length, this can be accomplished by mounting the end mirror on a piezo actuator. For a mode-locking laser process the oscillator's repetition rate ν_r is inversely proportional to the cavity optical length L: $\nu_r = c/2L$. The oscillator imposes the temporal frequency of the system and thus it is the stage to synchronize with the accelerating field in the photo-injector for extraction of the photoelectrons at a stable RF phase. We propose to use an optical cavity length of 1.8 m with a repetition rate of $79+\frac{1}{3}$ MHz. This frequency corresponds to the 36^{th} sub-harmonic of the S-band RF accelerating field. A dedicated synchronization system must lock the repetition rate to an external master clock moving the oscillator's end mirror by a piezo transducer. Using a mixing electronics scheme with high harmonics of the oscillator frequency it is possible to lock the pulse emission to an external clock with high stability and to restrict the jitters within 250 fs.

After the oscillator it will be placed the pulse shaping devices. This arrangement is motivated by two considerations: the low damage threshold of the pulse manipulator and its insertion losses that can be recovered only if it is installed before the amplification. The devices it the topic of the next chapter.

Two Ti:Sa amplification stages are needed to enhance the energy up to 20 mJ at the 800 nm wavelength, with a gain approaching 10^8 when one takes into account losses in the pulse shaping process and in the stretcher-compressor.

The energy level is fixed from the required energy at the cathode see the table 3.1. In fact, we have estimated that the losses from 3^{rd} harmonic generation, the transfer line optics and the following pulse manipulations reach 97.5%, giving maximally 0.5 mJ on the cathode. This value is larger than the specification, thus allowing the nominal charge even for unanticipated losses and/or anomalously poor quantum efficiency.

A regenerative pre-amplifier and a multi-pass stage compose the most reliable scheme for the high power section of the laser system. A 1 KHz diode

pumped, frequency-doubled, Nd:YLF with energy of 10 mJ per pulse is used to pump the first amplifier stage. The multi-pass amplifier will excited by the second harmonic of lamp-pumped Nd:YAG laser, at 10 Hz with 600 mJ of energy per pulse and 7 ns of duration. According to the energy request the maximum repetition rate of the regenerative and the multi-pass amplifiers are limited at 1KHz and 10 Hz, so that a pulse picker between these two stages is needed. The first pump has a better energy stability because is pumped by diode, it reaches about 1% rms. The second laser has to produce very high energetic pulses and therefore it requires flashlamp pump that limits the energy stability to 3.5% rms.

The regenerative amplification is based on the pulse trapped in a laser resonator. The pulse is kept in the cavity until it has extract all the energy stored in the amplifier medium. Trapping and releasing the pulse is done using a Pockels cell and a polarizer. The synchronizing of the Pockels cell is done measuring the pulse's energy grown in the amplifier and setting the pulse releasing when the gain reaches the saturation. The working principle of the regenerative amplifier assures high pulse to pulse energy stability and transverse TEM_{00} mode purity. This kind of amplifier is very insensitive to energy variation of the input pulse, we observed in a laser similar to the SPARC system that the output energy does not vary even for reduction of the input energy of 90%. This kind of amplifier have some limitations for ultrashort pulse because of the large number of round trips in the crystal and in the Pockels cell. This limitations don't apply for the specific application we are considering.

The multi-pass amplification is based on a bow-tie type amplifier in which the different passes in the amplifier medium are geometrically separated. Usually the number of passes is four to eight. Higher the number of passes higher is the complexity of the laser alignment. The multi-pass is the only usable technique to produce energies above tens of mJ or pulse of tens of fs.

The pulse-to-pulse energy jitter produced by commercial high-energy amplifier is about 1.5% rms this limit is set especially by the high energy pump.

In amplifiers for sub-picoseconds pulses, the peak power must be limited to avoid non linear effects and damages to optical components using a technique CPA (chirped pulse amplification) [54]. For this purpose, a grating pair is used to introduce a high linear dispersion for the different frequency components of the pulses. In this way, the 100 fs from oscillator can be stretched up to 500 ps. After the amplifiers a grating pair in parallel arrangement provides complete compensation of the dispersion introduced by the stretcher. In the ideal case at the exit of the compressor the pulse has the same duration as at the input. Because of the high diffraction orders generated by the grating the compressor introduces a 50% energy loss. The commercial laser systems provide a pointing stability less than 2 μrad per hour with proper temperature stabilization.

3.4 Optical transfer line

We foresee the use of a circular aperture and a position-dependent attenuation filter to reduce the Gaussian transverse profile usually produced by the commercial laser to a near-uniform profile. This technique obviously introduce large energy losses. Other technique have been proposed to produce a uniform distribution starting from an arbitrary input transverse intensity. These techniques have the advantage of high energy transmission but are not applicable to our case. The use of micro-lens arrays are in fact not possible because this method reconstructs the uniform beam on a plane perpendicular to the beam axis [57]. In the SPARC RF gun, however, it has been chosen to illuminate the cathode at near grazing incidence. A new transverse homogenizer system is based on the a pair of aspherical lenses with a curvature appropriate for defocusing the higher density central part of the gaussian beam and focus the outer part [58]. This system produce a uniform distributed beam but few meters propagation worsen the flatness. In SPARC the propagation is foreseen over several meters.

The photon frequency has to be tripled by two non-linear crystals to obtain photons with energy above the photoemission threshold for copper. The large bandwidth of pulse limits the efficiency of third harmonic conversion. In fact the bandwidth of the non-linear crystal is inversely proportional to its thickness. But the efficiency of the frequency conversion process is proportional to the crystal's thickness. The efficiency of a non-linear process is proportional to the power density of the optical beam. After the UV conversion it will place an extra grating compressor change the pulse length over the desired range. In this way the IR power density is kept constant and the efficiency of the harmonic generator should be more stable.

The damage threshold of the crystal is 5 GW/cm^2 and that means the laser spot's diameter has to be larger than 4 mm. Typically, with the maximum power density, the third harmonic conversion is 5% for KDP-BBO crystals, and 10% for two BBO crystals with large bandwidth pulses. Additionally, the nonlinearity of the harmonic-generation process can enhance all initial energy jitters, as well as ripples in time or transverse spatial distribution. These considerations imply a more stringent set of parameters for laser system at the fundamental frequency. For instance the UV energy requirement corresponds to amplitude jitter of 1.5-2.5% at the fundamental frequency.

As said the laser beam impinge on the cathode at near grazing incidence. However the 72° incidence geometry induces two unwanted effects: a circular beam at grazing angle becomes an ellipse and the cathode side closer to gun entry will emit earlier. Corrections of both of these effects are required to minimize the emittance.

The temporal effect has to be corrected by controlling the optical path of the various rays within the beam.

At the cathode the delay Δt is proportional to the difference of the optical

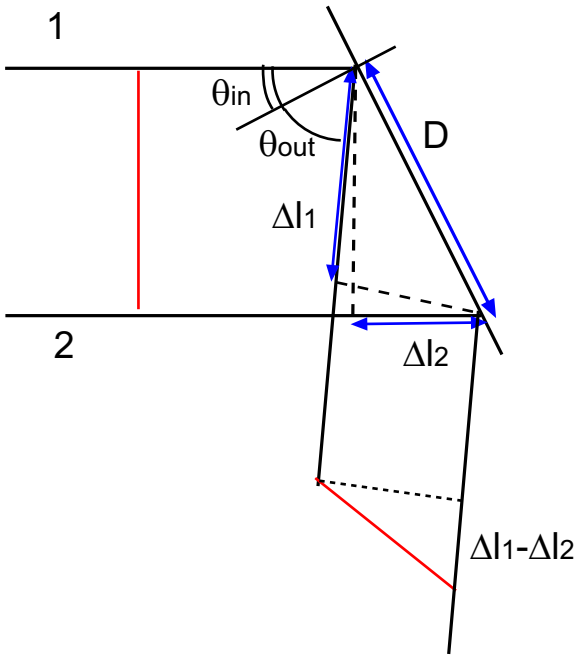

Figure 3.4: Sketch of the grating based wavefront tilt

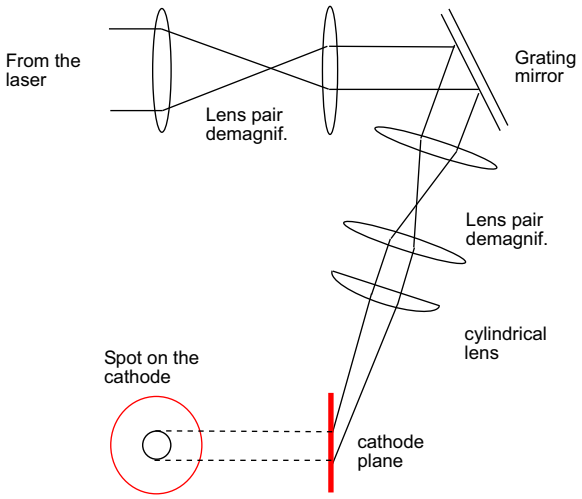

Figure 3.5: Arrangement of the optical components near the gun

path between the extreme rays ΔL_c that depends on the spot diameter on the cathode D_c, $\Delta t = \Delta L_c/c = D_c sin72°/c$. D_c=2.26 mm, c is the light velocity in the vacuum and $\Delta t = 7.16ps$. Therefore this effect changes radically the cylindrical distribution and nullifies the emittance compensation.

To counterbalance this effect, a proper reflective blazed grating can be employed.

The groove spacing of the grating have to be chosen to impose the same optical length to the cathode at all the optical rays. Since gratings are lossy in the ultraviolet care must be taken to make the beam size on the grating large enough to avoid damage.

The equation that expresses the output angle respect to the normal θ_{out} as function of the input angle θ_{out} is [56]:

$$sin\theta_{out} - sin\theta_{out} = \frac{m\lambda}{d} \qquad (m = 0, \pm 1, \pm 2 \dots) \tag{3.1}$$

where m is the diffraction order, d is the period of the grating often expressed as the spatial frequency T=1/d, groove's spacing and λ is the wavelength. We chose to work on the first diffraction order because the efficiency lower for higher order and the angular dispersion becomes significant $d\theta/d\lambda \propto m$. According to the scheme in the Fig. 3.4 the optical path difference is:

$$\Delta l = \Delta l_1 - \Delta l_2 = D(sin\theta_{in} - sin\theta_{out}) \tag{3.2}$$

the compensation is achieved when it is equal to the optical path difference at the cathode $\Delta l = \Delta l_c$. For a normal number of grooves per mm the complete compensation can be done if the beam's dimension at the grating is larger than the spot on the cathode. Therefore we propose to place the grating between two demagnifier zooms: the first reduce the laser beam diameter from 10 mm to 4.7 mm and the second to the required dimension to the cathode see fig 3.5. To obtain a circular spot at the cathode a cylindrical lens must be used. This optic focus the beam only in the plane that contains the beam axis and the cathode normal. Using the scheme proposed we have studied the compensation using a package in Mathematica software. The software allows a three-dimensional ray tracing and take in account the optical path in the lenses. The results indicate that using a grating with 1400 lines/mm at 22.7° an a 4.7 mm spot on the grating it is possible to reduce the optical path difference to 86 μm rms. With a cylindrical lens with focal length of 50 cm it is possible to obtain an almost circular beam with the ratio between the axes up to 0.98. Perfect circularity cannot be obtained because of the two sides of the beam are at different distances from the cylindrical lens' focus.

A dedicated design of the transfer line from the exit of the laser system to the cathode must be undertaken. Critically, the required performance of the laser on the cathode demands good compensation of the pointing

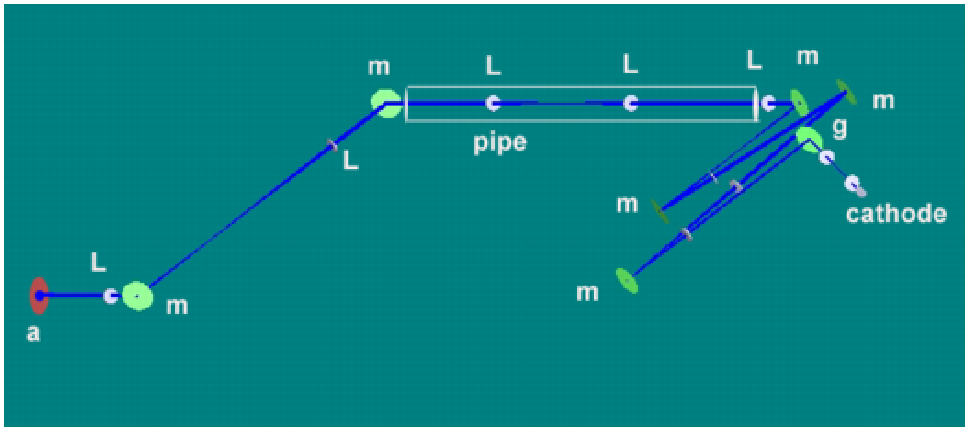

Figure 3.6: Sketch of the optical transfer line from the aparture a) to the cathode. It is possible to see the mirrors m) the lenses L) the grating g) and the evacuated pipe.

instability (we recall that can be accepted at maximum 33 μm). An evacuated beam pipe will be employed for laser transport to the gun for preservation of the spatial and temporal pulse profiles and suppression of steering jitter. Additionally, it has been demonstrated that Fourier relay optics can mitigate the effects of the angular jitter from the laser. We foresee to use a spatial flattener aperture as a stable object plane. The Fourier optical system is composed by a lenses' pairs. A lens of focal length f_1 will be inserted a distance f_1 from the pin-hole, at a distance f_1+f_2 will be placed a second lens with focal f_2 that will image the object at distance f_2. This basic element can be repeated several time to cover the distance between the laser exit to the cathode that is 8 meters. Because the complexity of the system we performed simulation using the Zemax optical design program. This powerful software includes the aberrations, the physical optical approximation and a detailed model for most of the common optical elements. The optical transfer line is reported in the figure 3.6. It includes two mirrors at the beginning to steer the beam in the pipe. The mirrors and the lenses after the pipe are used to obtain on the grating the right angle and the correct dimension respectively.

The study of the sensitivity to pointing instability from the laser, indicates that angular displacement of 100 μrad rms produces at the cathode only 20 μm rms shift of the centroid. The effect of temperature change over 80 $^\circ$ is negligible. In the Fig. 3.7 is reported the transverse intensity distribution as false color scale assuming a top hat transverse pulse at the input. As it can see the spot is very uniform and slightly enlarged in the vertical direction that is caused by chromatic effects from the grating. The simulated input beam has a bandwidth of 5 nm centered at 266 nm, three time larger than the bandwidth expected in the experiment. In this case the centroid shift covers about 80 μm rms and indicate a acceptable displacement for the narrow

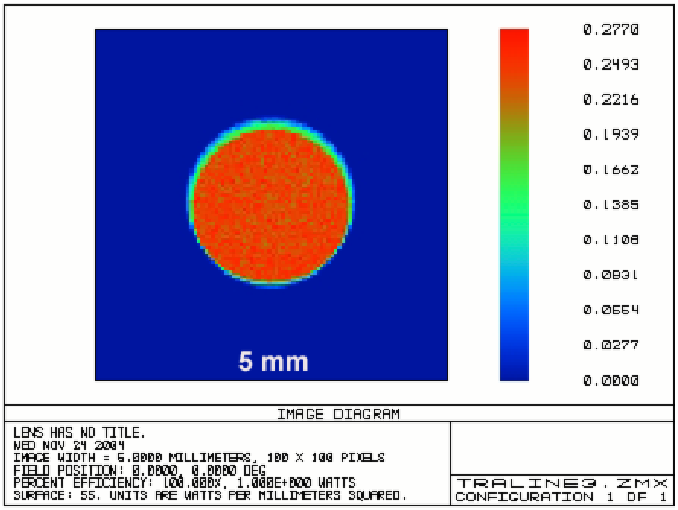

Figure 3.7: Sketch of the grating based wavefront tilt

bandwidth beam expected. Further studies are needed to include alignment errors and diffraction effects and to simplify the optical transfer line.

To improve the time and the energy stability of the system it is necessary to control the temperature of the environment. We plan to build a dedicated class 10^4 clean room with temperature stabilization to better than $\pm 1°C$.

3.5 Laser diagnostics

The monitoring of the laser system's performance and active control feedbacks are a prerequisite for optimal laser operation. Here we report the measurements and controls that we intend to perform on the most important laser pulses' characteristics.

Time profile diagnostics The temporal characteristic of the pulse of interest from the photoemission point of view is the beam intensity. In fact the phase of the pulse does not influence the photoemission process. The measurement will be used as a feedback for the pulse temporal manipulation.

To measure the 2 to 12 ps flat top pulse's intensity profile, a streak camera can be used. This diagnostic tool allows the direct measurement of the temporal distribution of the photons from infrared to ultraviolet with energy even at laser oscillator level. Typically, the streak camera has 1 ps of resolution, but recently for expensive streak cameras the resolution has been increased to 0.5 ps. Thus this technique needs integration with optical-based diagnostics. Because the pulse is chirped it has a large spectrum and a long

duration compared to the hundred of fs. Therefore techniques most used in the ultrashort pulse diagnostic cannot be easily used. For instance the FROG (Frequency Resolved Optical Gating)and SPIDER (Spectral Phase Interferometry for Direct Field Reconstruction) [59, 60] show problem to measure pulse larger than 1 ps.

Optical cross-correlation and auto-correlation techniques can be used to obtain resolutions down to 100 fs. The correlation signal is obtained by mixing two collinear and delayed replicas in a non-linear material (such as a thin piece of fused silica) to produce an up or down conversion of the pulse [44]. To measure the correlation signal a photodiode or a CCD have to be used. Starting from the correlation signal, information on the input signal can be obtained with numerical calculations. If the two replicas are produced by splitting the same pulse one obtains the autocorrelation signal. Instead if the pulse is mixed with a short reference pulse the result is the cross-correlation signal. With the autocorrelation technique it is not possible to detect the asymmetry of the pulse and, assuming the input pulse shape, only the duration can be calculated. The cross-correlation allows the signal reconstruction by numerical calculation if the reference beam is short enough. We plan to use a cross-correlation between the 100 fs at $\lambda = 800$ nm pulse from the oscillator and the 2-12 ps amplified square pulses at $\lambda = 266$ nm. Because the harmonic generation crystals absorbs wavelength shorter than 200 nm, the mixing should produce the difference between the frequencies according to the down conversion scheme. In this way the mixing produce a signal centered at 400 nm proportional to the pulse product. This technique can produce a multi-shots reconstruction of the temporal intensity. In principle the cross-correlation technique can be extended to a single-shot by mixing the two wavelengths in the crystal with a crossing angle different from zero. In this way it is introduced a spatial temporal correlation and a CCD can be used to reconstruct the cross-correlation signal. To implement this diagnostic further studies are needed.

The measurement of the temporal profile before the amplifiers, will assure the correct operation of the oscillator. For this diagnostic a auto-correlator can be used.

The temporal diagnostic should be integrated with spectral domain measurement in the IR and in UV.

Energy and power measurement To satisfy the energy amplitude requirements on the cathode it is mandatory to control the pulse energy in different points in the laser system and the transfer line. The pulse energy can be measured with pyro-electric joulemeter or calibrated photodiode on a fraction of the laser beam reflected by a beam splitter. Joulemeters and photodiodes will work from infrared to ultraviolet, and show linear response over up to two orders of magnitude. The pulse energy will be monitored at the exit of the oscillator, after the third harmonic generator and on the

virtual cathode. To measure the pulse energy at high repetition rate such as at the level of the oscillator or the regenerative amplifier it is conceptually correct to perform a power measurement. For this purpose it can be adopted thermal detector as the power meter. This detector based a thermocouple, produce a output voltage proportional to the average power and, therefore, heat impinges on the sensitive area. To change the pulse energy on the cathode, a proper choice of variable neutral density filter can be adopted. But is more appropriate to use a quarter-wave waveplate and a polarizer. The first element can rotate continuously the laser polarization. The attenuation of the pulse energy has been done after the UV generator to have a more precise control of the energy on the cathode.

Spatial properties monitoring For the diagnosis of the laser spatial characteristics, CCD cameras at different positions are useful tools. Special care must be given to the measurements of the centroid position of the transverse profile, and spot diameter jitter especially at the cathode's conjugate plane. Commercial CCDs without the usual UV-protective windows can be used for the UV pulse. Recently we have tested a scintillator that absorb the UV radiation and emits visible light at 550 nm in the sensivity range of the CCDs.

The used scintillator screen is 100 μm thick of a YAG:Ce crystal($Y_3Al_5O_{12}$: CeO_2 0.15%). This screen, used also for e-beam diagnostic, absorbs UV light and emits radiation, with a decay time constant of 70 ns.

A computer with a digital frame grabber can be used to record the video image and calculate the centroid location and the dimensions of the beam. The resolution of the spatial measurements is set by the pixel dimensions. The commercial CCDs have an active area 4 by 10 mm and the pixel dimensions are 8 by 11 μm. A quadrant photodiode in the virtual cathode is useful for fast feedback for spot centroid positioning. The feedback loop will drive the a piezo-actuators of the last mirror.

Laser to master oscillator phase measurement The laser time jitter is mainly introduced within the oscillator. To measure it a fast PIN photodiode (a sandwich of intrinsic semiconductor between n- and p-doped semiconductors) will be placed just after the oscillator. The fastest photodiode are available with time response down to 7 ps rise time. Using an equivalent-time oscilloscope triggered by the RF system it is possible to increase the resolution to 3 ps. This means that one must use other techniques for less than 1 ps time jitter diagnostic and compensation. The synchronization system is based on a phase locked loop (PLL) to control the oscillator frequency. The 79.333 MHz repetition rate pulses will be detected with an InGaAs diode with a bandwidth of 3.5 GHz. The 100 fs pulses contain harmonics up to a very high order that allow extract the 2856 MHz with a band-pass filter. The frequency difference with respect to the RF can be measured by mix-

ing with the RF signal. The frequency error will drive the end mirror by a piezo-electric actuator and a picomotor. On the other hand, the phase error between optical pulse and RF oscillator will control the RF phase shifter. With this technique a resolution of hundreds of fs can be obtained. The time jitter that will be introduced by the amplifiers and the transfer line will be measured just before the gun. Because here the pulse repetition rate is 10 Hz a dedicated diagnostic system has to be developed. An indirect measurement of the laser pulse jitter with respect to the RF system is also possible at a BPM or resonant cavity on the beam line after the gun.

Chapter 4

Laser pulse manipulation in the time domain

4.1 Introduction

As said before to produce high brightness electron beam an energetic UV squared pulse is required. The pulse optimal shape for SPARC photo-injector has been determined by electron beam simulation codes. The required pulse profile should have rise and fall time less than 1 ps and ripple on the top less than 30% peak to peak. The length of the pulse should be variable from 2 to 12 ps.

The pulses delivered by commercial lasers naturally display a sech^2 or a gaussian temporal profile. Therefore to generate the target profile and external device is required. Because of the time resolution needed, it is not possible to work in the temporal domain. The fastest electro-optics devices, such the Pockels cells, are able to control the interaction with a optical pulse over some ns. This is the reason why the problem to generate flat top laser pulse is tackled by manipulation of the spectrum of the pulse. The high resolution requested in time implies a broad bandwidth pulse input pulse. This considerations and the high energy required lead to the choice of the Ti:SA laser technology.

The pulse shaper devices have large insertion losses and low damage thresholds: therefore the filtering has to be applied before amplifying the laser pulse to recover the losses. Beside, the spectral manipulation has to retain almost all the spectrum of the incoming pulse because otherwise it would induce problems for the chirped pulse amplification process [45]. In fact with a narrow bandwidth the stretching is no more effective to lengthen the oscillator's pulses. The short pulse can be amplified to power density higher than the damage threshold of the optical components in the amplifier.

It is well-known that the Fourier transformation of a square pulse of duration τ corresponds to the function $\sin(2\pi \cdot \tau f)/f$, where f is the frequency. As a matter of fact, if amplitude modulation were applied, filtering out spectral

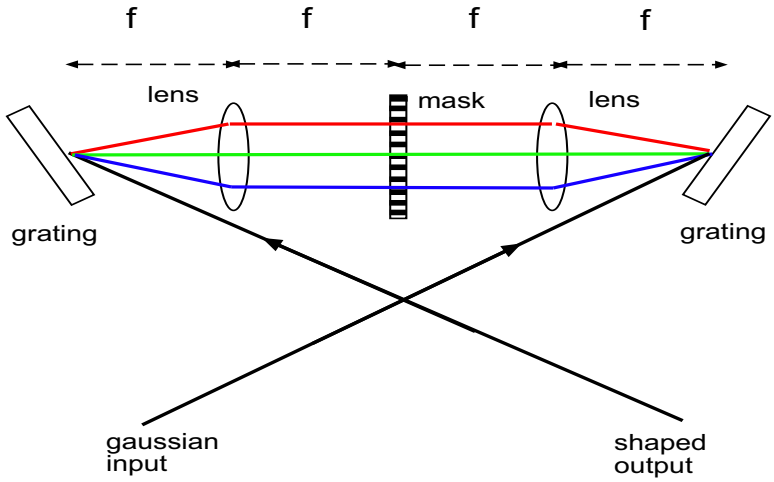

Figure 4.1: Liquid crystal based pulse shaper. The input optical wavelengths spatially dispersed by the first grating are incident on the liquid crystal active mask where experience different phase shifts or amplitude attenuation. The second grating recombines the wavelengths.

components and reducing the spectral bandwidth, for τ=10 ps and a transform limited 100 fs input pulse, the spectrum of the $\sin(2\pi \cdot \tau f)/f$ would be reduced by two orders of magnitude. In order to amplify the laser pulse in safe conditions a stretcher as long as tens of meters would be needed.

On the other hand, applying just phase modulation and a gentle amplitude filtering makes possible to retain the almost full spectral bandwidth of the laser pulse produced by the oscillator. Some experiments indicated that the required profile can be approached with only a phase modulation system [45]. Only phase modulation is applicable because only the intensity profile of the output pulses must be specified (not the output phase): this is actually the only important factor since the phase profile has no consequence in electron photoemission. In general, because we used shaper capable to modify both the amplitude and the phase of the input pulse we preferred to work on both the features to have more degrees of freedom. The phase-only filtering is energetically more efficient (i.e., results in minimal power loss), but the experiments conducted indicated the amplifier, because work in saturation, is insensitive to energy losses over a large range.

In order to perform such a phase manipulation two different techniques have been proposed based on a liquid crystal mask or an acousto-optic birefringent crystal [69, 70].

To produce the desired pulse shape it was proposed a mask placed between two gratings [71] called spatial light modulator (SLM). In the late 1980s experiments were done with fixed mask. After, using a liquid crystal array as the mask, the device allows programmable transfer functions [70]. The mask is placed in the center of two gratings in the focal plane of a 1:1 telescope

and can introduce phase delays or amplitude attenuation to different spatially dispersed frequencies, see Fig 4.1.

The commercial liquid crystal, used in this application, consists of an array of 100 μm vertical cells that introduce a delay that is proportional to a DC voltage applied to its sides. In fact the applied voltage change the refraction index of the liquid crystal in the cell. The space between the cells is 3μm and the number of the pixels is 128 or 512. The amplitude modulation can be achieved placing two crossed polarized on the front and on the rear of the liquid crystal. With computer addressing is possible to produce a large set of waveforms. Recently some results on pulse shaping using a 128-pixel liquid crystal mask have been reported [45]. A extended review on the SLM is reported in the article [72].

Instead we tested a new technique based on a programmable AO dispersive filter produced by FASTLITE (named DAZZLER). This device is able to perform simultaneously amplitude and phase modulation [69].

For the acoustic-optic technique, a chirped acoustic wave and the optic pulse linear polarized interact in a TeO_2 crystal. The acoustic perturbation in the crystal, produce an amplitude and phase filter.

A comparison between the two techniques shows that the acousto-optic solution performs a continuous frequency modulation, and is able to allocate a bandwidth one order of magnitude larger than the capability of liquid crystal technique. The alignment of acousto-optic crystal is less critical than liquid crystal mask. Both the types of shaper can be driven dynamically by measuring the pulse profile after the amplifier to pre-compensate gain and conversion distortions.

As said before the sinc modulation cannot be implemented in our system. In general there isn't any simple analytical solution to obtain the desired temporal profile at the cathode. In fact one has to consider the pulse shaper's non idealities, the distortion that the pulse undergoes in the chirped pulse amplification, the non linear behavior introduced by the UV conversion and following manipulation to the cathode. Therefore, it is welcome a optimization procedure to gradually achieve the flat top pulse. In our experiment we implemented a feedback loop using the measured temporal profile to optimize the filter function. A general comment is that the proposed solution probably cannot obtain the most squared pulse profile. Improvements can be obtained by implementing genetic algorithm optimization. This optimization procedure generates filter functions with random amplitude and phase change at each iteration and the change is accepted if it produces a better approximation of the target pulse and rejected otherwise.

4.2 Acusto optics interaction

When an acoustic wave is propagating in a medium it induces a deformation in the molecules distribution and thus a local change of the index of refrac-

tion. This effect is called photo-elastic effect. The refractive index's change has the same periodicity of the acoustic wave. In this section we ignore the non linear terms of the linear acousto optics effect.

The linear photoelastic effect involves the first order change of the optical properties of a medium due to an acoustic strain S_{kl}. The effect is characterized by the 4^{th} order tensor p_{idkl}. When an acoustic perturbation is applied the phenomenological relation proposed by Pockels [73], that expresses the change of index of refraction tensor n is:

$$\Delta\left(\frac{1}{n}\right)_{id} = p_{idkl}S_{kl} \tag{4.1}$$

where *idkl* refer to a the spatial coordinate system chosen. The $\Delta(1/n)_{ij}$ and S_{kl} are both symmetric tensor and p_{idkl} is symmetric upon interchange of *id* and *kl*. The change of the index of refraction induces a change in the index ellipsoid or in other word produces an optical anisotropy. To understand the effect of a acoustic perturbation one can refer to the new index ellipsoid and find the new optical axes. Here we consider the problem using the dielectric permittivity.

In general, the components of the relative dielectric tensor can be expressed in terms of index of refraction as, [74]:

$$\begin{aligned}\left(\frac{1}{n^2}\right)_{i\neq j} &= -\frac{\epsilon_{r_{ij}}}{\epsilon_{r_i}\epsilon_{r_j}}\\ \left(\frac{1}{n^2}\right)_{ii} &= \frac{1}{\epsilon_{r_i}}\end{aligned} \tag{4.2}$$

where $\epsilon_i = \epsilon_{ii}$. Therefore the photo-elastic effect of Eq. 4.1 can be reexpressed as:

$$\Delta\epsilon_{r_{id}} = -\epsilon_{r_i}\epsilon_{r_j}p_{idkl}S_{kl} \tag{4.3}$$

This equation is formally identical to the 4.1 and it allows to write the polarization vector ΔP when the optical field and the strain coexist in the medium. We assume that the optic wave is polarized along the d direction E_d:

$$D_i = \epsilon_0 E_i + P_i = \epsilon_{id}E_d \tag{4.4}$$

D is the displacement electric field. The electric polarization induced by the acoustic strain is:

$$\Delta P_i = -\frac{\epsilon_i\epsilon_d}{\epsilon_0}p_{idkl}S_{kl}E_d \tag{4.5}$$

The Eq. 4.5 shows that the electric field polarized along d and the strain vector polarized along *kl* induce together a polarization vector along a different direction *i*. This anisotropic effect is caused by the nature of the acoustic wave.

We discuss now the conditions are needed to efficiently couple two generic optical waves under the influence of the acoustic wave.

We start writing the wave equation in the presence of the polarization term generated by the acoustic strain:

$$\nabla^2\mathbf{E} = \mu\epsilon\frac{\partial^2\mathbf{E}}{\partial t^2} + \mu\frac{\partial}{\partial t}(\Delta\mathbf{P}) \tag{4.6}$$

We assume the optical field composed by two plane waves: one polarized along i and one along d. The two waves propagate along $\mathbf{k}_i$ and $\mathbf{k}_d$, which in general are not parallel. The plane waves are:

$$E_{i,d}(\mathbf{r},t) = \frac{1}{2}E_{i,d}(r_{i,d})\exp i(\omega_{i,d})t - \mathbf{k}_{i,d}\cdot\mathbf{r}) + c.c. \tag{4.7}$$

r_i and r_d are the distance measured along the wave vector $\mathbf{k}_i$ and $\mathbf{k}_d$ respectively. We can think one of the plane wave is the input optical beam and the other gain energy from the acousto-optic interaction. We will ignore which is the input beam and this will be established when the boundary conditions are applied to the general solution. Two differentiations applied to the plane wave lead to:

$$\nabla^2 E_i \cong -\frac{1}{2}\left(k_i E_i + 2ik_i\frac{dE_i}{dr_i}\right)\exp i(\omega_i t - \mathbf{k}_i\cdot\mathbf{r}) + c.c. \tag{4.8}$$

where we assumed the so called slow wave approximation: $\nabla^2 E_i \ll k_i dE_i/dr_i$. The same expression can be written for the E_d. Considering that $k_i = \omega_i\sqrt{\mu\epsilon_i}$ the first right side term of Eq. 4.8 cancels the first term on the right side of the wave equation.

The acoustic wave is assumed propagating along an arbitrary direction $\mathbf{K}$, and the strain is expressed as pure sinusoidal function at the frequency Ω:

$$S_{kl}(\mathbf{r},t) = S_{kl}/2\exp[i(\Omega t - \mathbf{K}\cdot\mathbf{r})] + c.c. \tag{4.9}$$

we include the strain in the expression of the polarization vector of Eq. 4.5. The polarization induced in the i direction is proportional to the product of two exponential function the optical plane wave and the acoustic plane wave.

In order ΔP_i acts as a synchronous driving term for the second optical field E_i, it must, like E_i, have a term varying like the $\exp(i(\omega_i t - \mathbf{k}_i\cdot\mathbf{r}))$, otherwise the contribution by the polarization vector when averaged over long time or distance is zero. The following conditions have to be fulfilled:

$$\omega_i = \omega_d \pm \Omega \tag{4.10}$$

$$\mathbf{k}_i = \mathbf{k}_d \pm \mathbf{K} \tag{4.11}$$

The first condition is justified by the consideration that to have an exchange of energy between the two optical waves the polarization vector should

have the same frequency of the field E_i. The second condition, called often phase matching condition, will be clear soon.

The acousto-optics interaction can be thought as the collision between two particles that produce a third particle. A photon with energy $\hbar\omega_i$ and momentum $\hbar k_i$, interact with a phonon of energy $\hbar\Omega$ and momentum $\hbar K$ to produce a second photon of energy $\hbar\omega_d$ and momentum $\hbar k_d$. The equalities 4.10 and 4.11 express the energy and the momentum conservation.

Assuming the + term in the above equations and after some simplifications we obtain from the Eq. 4.6,4.8 and 4.5 the coupling equations, that take in account the energy exchange along the propagation of the two optical waves:

$$\frac{dE_i}{dr_i} = i\eta_{id} E_d \exp^{i(\mathbf{k}_i - \mathbf{k}_d - \mathbf{K})\cdot\mathbf{r}} \tag{4.12}$$

$$\frac{dE_d}{dr_d} = i\eta_{di} E_i \exp^{-i(\mathbf{k}_i - \mathbf{k}_d - \mathbf{K})\cdot\mathbf{r}} \tag{4.13}$$

where the coupling coefficient is:

$$\eta_{id} = \eta_{di} \cong \frac{\pi n^3}{2\lambda} p_{idkl} S_{kl} \tag{4.14}$$

Because the acoustic frequency is much smaller than the optical ones that: $\lambda_i \cong \lambda_d = \lambda$.

The phase matching condition in Eq. 4.11 should be satisfied otherwise the contribution from the field E_i to E_d reverse sign according with a spatial period $l_c \equiv \pi/|\mathbf{k}_i - \mathbf{k}_d - \mathbf{K}|$. Therefore the cumulative interaction between the optical waves cannot take place over a distance larger than the l_c, named coherence length. The phase matching equality is similar to the Bragg condition for the first order scattering of a grating. In fact the acoustic wave induces a periodic oscillation of the index of refraction like in the case a diffraction grating.

At the phase matching the coupling equation can be simplified as follow:

$$\frac{dE_i}{dr_i} = i\eta E_d \tag{4.15}$$

$$\frac{dE_d}{dr_d} = i\eta E_i \tag{4.16}$$

We took $\eta_{id} = \eta_{da} = \eta$. The Eq. 4.15 and 4.16 can be simplified assuming a new coordinate ζ that is the bisector of the angle θ formed between $\mathbf{k}_i$ and $\mathbf{k}_d$:

$$r_i = \zeta\cos\theta \qquad r_d = \zeta\cos\theta \tag{4.17}$$

so that the Eq.4.15 and 4.16 become:

$$\frac{dE_i}{d\zeta} = i\eta E_d \cos\theta \tag{4.18}$$

$$\frac{dE_d}{d\zeta} = i\eta E_i \cos\theta \tag{4.19}$$

whose solutions are:

$$E_i(r_i) = E_i(0)\cos(\eta\zeta\cos\theta) + iE_d(0)\cos(\eta\zeta\cos\theta) \tag{4.20}$$

$$E_d(r_d) = E_d(0)\cos(\eta\zeta\cos\theta) + iE_i(0)\cos(\eta\zeta\cos\theta) \tag{4.21}$$

The equations 4.20 and 4.21 describe the interaction between the two optical fields with arbitrary phase and amplitude as long as the Eq. 4.10 and 4.11 are fulfilled. The solution presented should be adapted to the case of an acousto-optical device where often the diffracted beam at the input is zero, for instance assume $E_d(0)$ is the diffracted beam.

$$E_i(r_i) = E_i(0)\cos(\eta\zeta\cos\theta) \tag{4.22}$$

$$E_d(r_d) = iE_i(0)\cos(\eta\zeta\cos\theta) \tag{4.23}$$

The number of photon is conserved and because $\omega_i \cong \omega_d$ the optical power is conserved: $|E_i(r)|^2 + |E_d(r)|^2 = |E_i(0)|^2$ The fraction of power of the incident wave transferred in a distance l to the diffracted beam is given by:

$$\frac{I_{diffracted}}{I_{incident}} = \frac{E^2_{diffracted}(l)}{E^2_{incident}(0)} = \sin^2(\eta l) = \sin^2\left(\frac{\pi n^3}{2\lambda} pSl\right) \tag{4.24}$$

where $pS \equiv p_{idkl}S_{kl}$. The total transfer of power occurs for $\eta l = \pi/2$. It is useful to express the coupling efficiency in term of acoustic intensity I_{ac} $[W/m^2]$ that is related to the strain by the relation:

$$S = \sqrt{\frac{2I_{ac}}{\rho v_s^3}} \tag{4.25}$$

being ρ the medium density and v_s the sound velocity.

$$\frac{I_{diffracted}}{I_{incident}} = \sin^2\left(\frac{\pi l}{\sqrt{2}\lambda}\sqrt{\frac{n^6p^2}{\rho v_s^3}I_{ac}}\right) = \sin^2\left(\frac{\pi l}{\sqrt{2}\lambda}\sqrt{M \cdot I_{ac}}\right) \tag{4.26}$$

M is called figure of merit and is defined as $M \equiv \frac{n^6p^2}{\rho v_s^3}$.

In the case of birefringent crystal, the two mode propagate with different velocity and therefor k_i and k_d have different length. When the acoustic wave is collinear with the input optical beam, like the DAZZLER, the phase matching condition becomes:

$$\frac{\omega}{c}(n_o - n_e) = \frac{\Omega}{v_s} \tag{4.27}$$

In this case the acousto optic interaction introduce a phase shift because the different phase velocities of the two modes. In the DAZZLER the acoustic wave is chirped: different acoustic frequencies are dispersed in time and thus in space. The frequencies of the input optical beam are diffracted in different position when the Eq. 4.10 and 4.27 are satisfied. Therefore for different input wavelengths a different phase delay and amplitude modulation can be obtained controlling the acoustic wave.

4.3 Acousto Optic Programmable Dispersive Filter: operation theory

The "DAZZLER" is a system designed by FASTLITE to filter ultrafast laser pulses. This system allows to program an arbitrary shape of the ultrafast laser pulses as well in amplitude as in phase [75, 76].

In the "Acousto Optic Programmable Dispersive Filter", AOPDF, a chirped acoustic wave and the optic pulse linear polarized interact in a TeO_2 crystal. Because the sound velocity v_s is much smaller than the optical one, c/n, and because we operate with short laser pulse in the scale of few ps, the acoustic strain can be though as a fixed perturbation of index of refraction. The acoustic-optic interaction occurs for different optical wavelengths, at different depths, where the phase matching conditions are satisfied, see Fig. 4.2. The input beam and the diffracted beam are the ordinary and the extraordinary modes of the tellurium dioxide crystal. The acousto-optics interaction induces the rotation of part of the input beam toward the extraordinary axis polarization. The acoustic and the optical waves propagate along the same direction z. Because the refraction index along the extraordinary axis is different from that along the ordinary one and a frequency dependent phase delay is obtained. A radio frequency generator (with spectrum between 40 and 55 MHz) drives a piezo-transducer to produce the acoustic wave.

Amplitude modulation The acousto-optic device performs a convolution between the amplitude of the input optical signal $E_{in}(t)$ and a programmable acoustical signal $S(t/\alpha)$ proportional to the electrical signal S_t(t) applied to the piezoelectric transducer of the device.

$$E_{out}(t) = E_{in}(t) \otimes S(t/\alpha) \tag{4.28}$$

In the frequency domain, this convolution relation can be written:

$$E_{out}(\omega) = E_{in}(\omega) \cdot S(\alpha\omega) \tag{4.29}$$

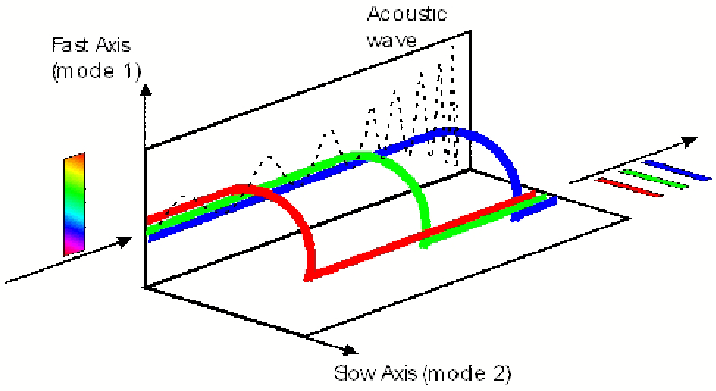

Figure 4.2: Dazzler operation's conceptual picture. Because the acoustic wave the different optical wavelengths are scattered at different depths. In this way an arbitrary phase and amplitude filtering can be produced.

α being a scaling factor equal to the ratio of the speed of sound v_s to the speed of light c in the crystal. The quantity reported in the equation 4.28 and 4.29 are complex therefore they express the amplitude and the phase properties of the DAZZLER transfer function. This formulas are valid at low diffraction efficiency ($\ll$100%) where the photo-elastic effect is essentially linear. The small value of α, enables the control of optical signals in the hundreds of THz range with electrical signals in the tens of megahertz range. α is also the ratio of the acoustic frequency f to the optical frequency ν. For example, if $\lambda = 800nm$, the optical frequency is $\nu = 375$ THz and the matched acoustical frequency is f = 52,5 MHz, $\alpha = f/\nu = \Delta n \cdot v/c = 1.4 \cdot 10^{-7}$. Therefore a commercial rf generator can be used to drive the acoustic wave through a piezo-electric transducer. The acoustic wave is imposed using a control software provided by the FASTLITE. The software has an user interface and allows to synthesize basic transfer function such as flat acoustic wave with central wavelength and width variable. It is possible to add an hole in the spectrum with variable depth, position and width. The software can control polynomial phase modulation up to the forth order. The control software can load a data file for arbitrary phase and amplitude modulation. We used this tool to obtain the flat top pulse.

The acoustic wave distribution along the crystal axis, z, can be express as:

$$S(z) = A(z)cos[\psi(z)] \tag{4.30}$$

We will discuss how to calculate the amplitude and phase term for a given transfer function.

The general formula giving the output optical power density $E_{out}(\omega)$ for the monochromatic case (frequency ω) come from the Eq. 4.26:

$$I_{out} = I_{in}(\omega) \cdot \frac{P(z)}{P_0} \cdot \frac{\pi^2}{4} \cdot sinc^2 \left[\frac{\pi}{2} \sqrt{\frac{P(z)}{P_0} + \Delta\phi^2} \right] \tag{4.31}$$

where $I_{in}(\omega)$ is the input optical power density, P the actual acoustical power density related to the amplitude of the acoustic wave $P(z) = |A(z)|^2$. The dependence from $z(\omega)$ expresses that the relation can be generalized to all the input wavelengths. Therefore to control the scattering efficiency for a certain wavelength we can control the amplitude of the sound wave at the corresponding acoustical wavelength. $\Delta\phi$ is an asynchronism factor dependant on the crystal interaction length L (in our case is 25 mm) and phase mismatching. The acoustic power P_0 depends on the wavelength and the crystal length and it is 3.8 mW/mm^2.

When $P = P_0$ and $\Delta\phi$=0, the transfer coefficient to the diffracted wave should be 100 %: $Iout(t) = I_{in}(t)$. But the AOPDF response is no longer linear with P. For sufficiently low values of P compared to P_0, the AOPDF response is linear with P and:

$$I_{out} = \frac{P}{P_0} \cdot \frac{\pi^2}{4} \cdot I_{in}(\omega) \tag{4.32}$$

Phase modulation The acoustic wave used to drive the DAZZLER crystal is chirped and therefore the phase matching occurs at different positions for different input wavelengths and the relation 4.11 is dependent on the propagation axis z:

$$0 = k_i(\omega) - k_d(\omega) \pm K(z) \tag{4.33}$$

If we assume a $K(z)$ monotone respect to z, it is related to the phase of the acoustic wave by:

$$\psi(z) = \int_0^z K(z)dz \tag{4.34}$$

The phase matching condition imposes that the an input frequency ω is scattered at the position $z(\omega)$.

$$K[z(\omega)] = k_i(\omega) - k_d(\omega) = \frac{\omega}{c}[n_1(\omega) - n_2(\omega)] \tag{4.35}$$

where n_1 and n_2 are the index of refraction of the ordinary and extraordinary axes. The group delay at the crystal exit L, for the frequency ω is calculated by:

$$\tau(\omega) = \frac{z(\omega)}{v_{g1}(\omega)} + \frac{L - z(\omega)}{v_{g2}(\omega)} \tag{4.36}$$

v_{g1} and v_{g2} are the group velocities for the two modes. Practically the for the given frequency, the propagation is associated to the velocity v_{g1} up to

the scattering position, and then to the velocity v_{g2} to the end of the crystal. The relation 4.36 fixes the maximum delay achievable within the length L. In the case of the DAZZLER crystal we used L=25 mm and the maximum delay is 6 ps. To simplify the above equation we introduce the differential group velocity quantity as:

$$\Delta v_g(\omega) = \left[\frac{1}{v_{g1}(\omega)} - \frac{1}{v_{g2}(\omega)}\right]^{-1} \tag{4.37}$$

and then the function $z(\omega)$ becomes:

$$z(\omega) = \Delta v_g(\omega)[\tau(\omega) - \frac{L}{v_{g2}(\omega)}] \tag{4.38}$$

The equation 4.38 explains that when a group delay is required the spatial acoustic wave, related to $z(\omega)$, should be produced. According to the expression of the 4.34 the acoustic phase can be unambiguously calculated. In the case the function $z(\omega)$ is not monotone there are more solution and the diffracted beam in the position 1 can be diffracted back to the input mode in a different position 2.

At the central wavelength of the Ti:SA, 800 nm the crystal second order phase is $12 \cdot 10^3\ fs^2$ and the third order is $8 \cdot 10^3 fs^3$, $n(\omega) = n_0 + n_1 + n_2^2$. In the application of the AOPDF it is correct to pre-compensate the intrinsic dispersion of the tellurium dioxide, $\partial n/\partial\omega$. The condition for a complete compensation, is that all the input frequencies experience the same group delay and the Eq. 4.38 becames:

$$z(\omega) = \Delta v_g(\omega)[T - \frac{L}{v_{g2}(\omega)}] \tag{4.39}$$

that becomes for $\Delta v_g(\omega) > 0$

$$\frac{L}{v_{g2}(\omega)} \leq T \leq \frac{L}{v_{g1}(\omega)} \tag{4.40}$$

this inequality is equivalent to:

$$max[v_{g1}(\omega)]_\omega \leq min[v_{g2}(\omega)]_\omega. \tag{4.41}$$

We can find a solution for T, and therefore obtain a the correction of the $Te0_2$ dispersion if the above is satisfied on all the input optical frequencies.

Interaction geometry in the tellurium dioxide. In the figure 4.3 is reported the geometry of the interaction in the TeO_2 crystal [77]. The phase matching condition is represented as the sum of the incident optical beam and acoustic wave vectors. The input optical beam is an ordinary mode and the diffracted wave is an extraordinary beam. The angle θ_o and θ_a are 38.5° and 3.9° respectively. This geometry assure high resolution but narrow

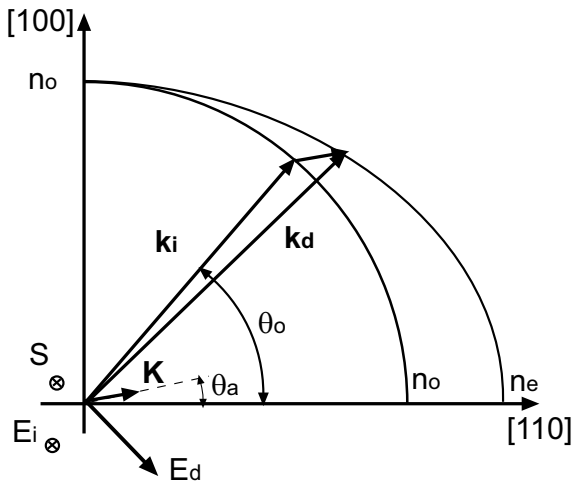

Figure 4.3: Geometry of the acousto-optics interaction in TeO_2 respect to the crystal crystallographic axes. The input optical wave and the acoustic wave are polarized along the $[\bar{1}10]$ direction.

optical bandwidth of the acousto-optic interaction [78]. The angle between the input and the diffracted beam is 1.6°

In this geometry the effective photo-elastic coefficient can be calculated as [79]:

$$p = -0.17 sin\theta_a \cdot cos\theta_o + 0.09 sin\theta_o cos\theta_a \tag{4.42}$$

The tellurium dioxide shows a positive optical dispersion $\partial n/\partial\omega$. This has two important effects on the Dazzler operation. The accessible optical bandwidth is reduced because of the non linear relationship between optical and acoustical frequencies. The spectral delay introduced by the material becomes important and the Dazzler may not be capable to correct it (auto-correction) by programming of a negative dispersion, because of the maximum delay. At 800 nm, it is possible to correct for the second order dispersion of the material over a relative range of wavelengths of about 12% (or 100 nm) and this is the maximum operating optical bandwidth. The third order phase dispersion can be neglected.

The resolution can be derived by the phase mismatching term of Eq. 4.31. It can be demonstrated that the resolution is 0.25 nm. The number of independent programmable points depends on the laser input pulse spectrum and the resolution of the crystal. In the experiment conducted the input spectrum was 10 nm and therefore the number of points are 40. The divergence of the laser input should be lower than 0.04°. The alignment of the input beam leads to a less stringent condition.

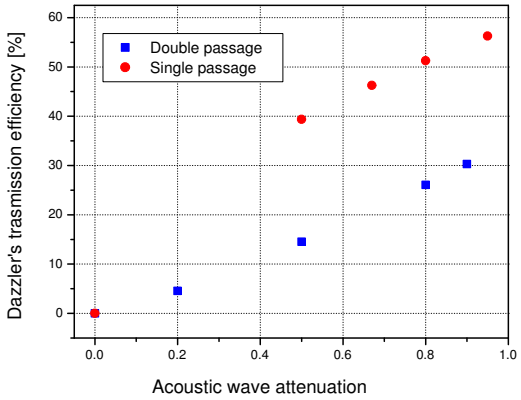

Figure 4.4: Measured DAZZLER efficiency for single and double passages configuration

4.4 Dazzler experiment

In SPARC laser system layout the dazzler acousto-optics crystal will be mounted upstream the amplifier. This choice is forced by two considerations. The first is the maximum power density that the the TeO_2 crystal can support, the value is 100 MW/cm^2 [77]. If we assume the laser spot of 10 mm^2 and the pulse duration of 100 fs, typical number at the amplifier output, the damage threshold value set a limit for the pulse energy at 1 μJ. The amplifier required for photo-injector application has to deliver at the fundamental wavelength, tens of mJ and therefore the dazzler cannot be placed at the exit of the amplifier. The second consideration is related to the acousto-optics interaction efficiency. In fact the measured crystal energy transmission is reported in the Fig. 4.4. The measurements were done for different radio frequency energy levels sent to the DAZZLER crystal. The measurements were performed with two possible configurations one and two passages in the crystal. The optimal operating point is obtained for an RF level around 0.5, beyond this level the DAZZLER response is not more linear.

As shown in the plot the energy transmission of the dazzler is about 0.4 at the normal operating level of the radio frequency intensity. This means if the DAZZLER is place downstream the amplifier more than half of the energy per pulse is lost. Instead, because the Ti:Sa amplifiers usually work in saturation, the energy insertion losses before the amplifier don't affect the energy per pulse is delivered by the laser system.

The DAZZLER crystal has to be aligned for optimal operation. The crystal has to be aligned to have uniform intensity acoustic wave and to have the phase matching condition. We mounted the crystal so as to have rotational control in the diffraction plane with about 1 mrad accuracy and translational control along the transverse directions (0.1 mm accuracy).

To have flat acoustic wave the acousto-optics interaction area should be at the same distance from the piezo-electric transducer. We moved the crystal in the transverse direction to have a flat response when a uniform acoustic wave is induced. To do this alignment a photodiode was installed on the diffracted beam.

For frequency calibration we used a calibrate spectrometer with resolution of about 0.3 nm . We sent the diffracted beam into a detector and check the calibration by applying and hole in the spectrum. If the hole in the output is shifted an adjustment of the crystal angle by rotating it in the diffraction plane can correct the effect. Indeed the phase matching condition depends on the angle between the input optical vector and the sound propagation direction. If the angle is not correct the period of the acoustic perturbation experienced by the laser pulse is shifted.

We tested the AOPDF also in double passages configuration as reported below. In this case the alignment is more complicate. To obtain a double passage in the crystal a mirror was mounted very close to the DAZZLER output face. At the exit of the crystal there were many beams (reflected on the input face, reflected on the exit face, the beam un-diffracted in the first pass, the diffracted and un-diffracted beam on the second pass). The useful beam was very close to the input beam and can be detected measuring the polarization. If there is a 'frequency' misalignment in the two passages the optical pulse experiences a phase matching for two different wavelength so that two valleys appear in the beam spectrum.

Simulations of the optimal transfer function

As said before the sinc modulation is not applicable because it involves a cut of large part of the spectrum. We developed the numerical code, in Labview environment, to simulate the optimal phase and amplitude modulation for the DAZZLER. The program simulates the behavior of the DAZZLER: it allows the modification of the amplitude and the spectral phase of a gaussian input spectrum, and then, through the FFT, calculate the output temporal profile.

The desired square pulse can be obtained with a square spectrum and a second order phase. In fact the second order phase linearly maps the spectral distribution in the time domain. The second order phase shift can be obtaining using the DAZZLER or by not compress the pulse after the amplification. In the calculations, the second order phase shift is obtained controlling that output pulse duration is 10 ps. To approximate the square spectrum we adopted a supergaussian function:

$$S(\nu) = S_0 \cdot \exp\left[-\left(\frac{\nu - \nu_0}{\Delta\nu}\right)\right]^n \tag{4.43}$$

In the Fig. 4.5 are reported the simulations done with an input 100 fs transform limited pulse and ν_0=384 THz corresponding to λ = 800nm and

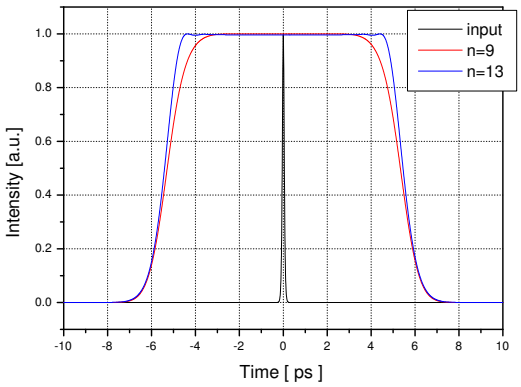

Figure 4.5: Simulated temporal intensity is obtained producing an output supergaussian spectrum of the 9^{th} an 13^{rd} order and a second order phase red and blue curve respectively. The input pulse is a transform-limited 100 fs gaussian pulse black curve.

we assumed $\Delta\nu_0$=2.83 THz. If the transform limited input pulse is longer and consequently the spectrum is narrow the results show overshoots and ripples.

The results are calculated imposing a amplitude mask that give an output supergaussian spectrum. The plot contains the input pulse intensity, the pulse obtained with a n=9 and n=13. The rise time for n=9 the rise time is 1.85 ps and for n=13 it is 1,34 ps. Higher supergaussian order would be needed. For the supergaussian order n=13 the spectral modulation has a edge of 1 nm. Therefore because the maximum resolution of the DAZZLER is 0.25 nm the programmable points, on the spectrum edge are only 4, thus it can be considered as the maximum order can be obtained with the AODPF.

To reduce the rise time higher phase orders are needed. To produce the phase function we adopted a polynomial expansion containing only the even orders, in fact the odd orders introduce asymmetry in the output time profile. We add to the curve of Fig. 4.5 for n=13 the6^{th} and the 8^{th} phase orders. As shown in Fig. 4.6 rise time is reduced from 1.34 ps to 1 ps. The shorter rise time induces ripples on the top a overshoots due to the Gibbs phenomenon [80] for finite bandwidth spectrum. Better result can be obtained using an amplitude filter to produce larger bandwidth. This can be achieved by reducing more the central wavelength respect to the tails. The simulations reported are intended to just introduce the guidelines followed in the experiment. The filter function could be optimized but the DAZZLER has to compensate non-ideal effects and distortions coming out from the amplification process and the stretcher and compression. Therefore an feedback loop optimization has to be used from the diagnostics.

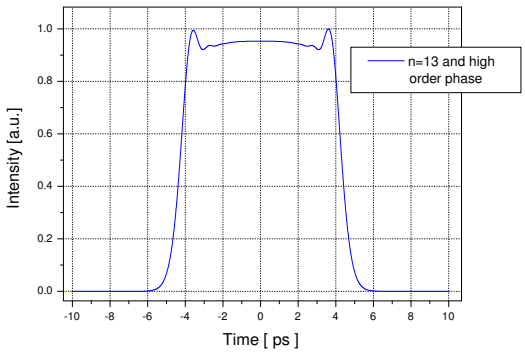

Figure 4.6: Simulated output time intensity including the higher order phase terms in the filter function.

4.4.1 Pulse shaping experimental measurements

We tested the DAZZLER at the ULTRAS laboratory of the Politecnico in Milan [81]. The source used for the experiment was an amplified Ti:Sapphire laser. The system consists of an ultrafast oscillator able to produce 20 fs pulses pumped by 5W green laser. The oscillator pulse is amplified in a standard chirped pulse amplification scheme in 1 KHz regenerative Ti:Sa module. The experimental apparatus is reported in Fig. 4.7

The laser delivered 20 fs FHWM, 1 mJ pulses at 1 kHz repetition rate with the central wavelength at 800 nm, in horizontal linear polarization. A small fraction of the laser beam (20 μJ) was sent to the experimental setup; here the beam was divided in two arms by a 50% beam splitter. In the first arm the beam was sent through a 10-nm band pass spectral filter, to obtain 100 fs FWHM pulses (as we expect for the SPARC laser), and then through the DAZZLER crystal. The band-pass filter we used had a central wavelength at 780 nm slightly different from the central wavelength of the laser system at 800 nm therefore the output spectrum, as reported later is not perfectly symmetric. The second pulse (gate pulse) was sent to a delay line controlled by a 100 nm linear resolution stepper motor. The delay line was used to assure the overlap of the two pulses. For the measurement the shaped pulse and the gate signal overlapped in a non linear BBO crystal with 200 μm thickness producing a second harmonic signal. We used 50 cm lens to increase the efficiency of the non linear mixing and to realize a not collinear crossing in the BBO. In this way the gate pulse the DAZZLER beam and the cross-correlation signal emerged from the non-linear crystal with different angles, and therefore the right beam was easily measurable. The emerging double frequency pulse was proportional to the cross-correlation of the two pulses, and it was measured by a photodiode. The measurement was based on the lock-in technique to suppress the 50 Hz noise. The AO shaper was

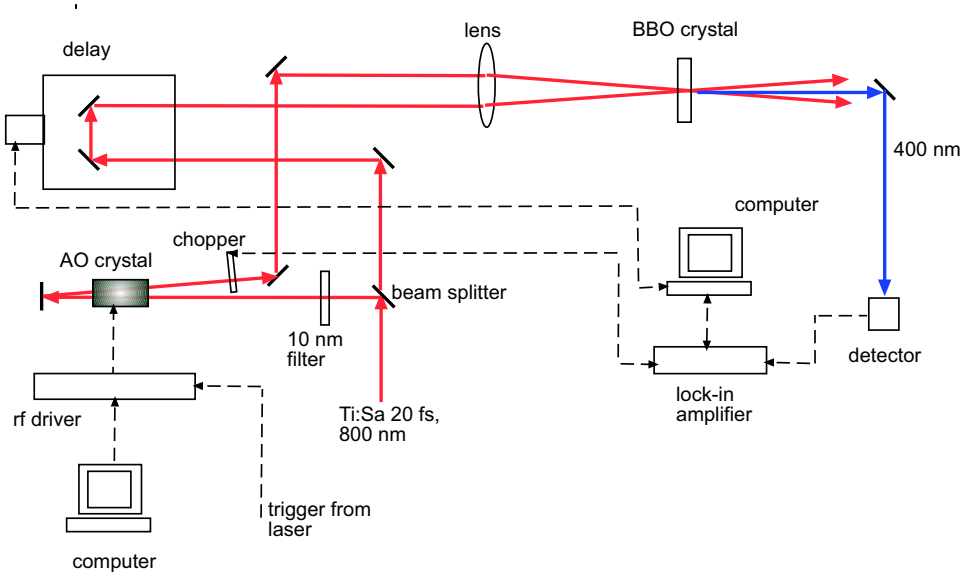

Figure 4.7: Drawing of the experimental apparatus developed for the DAZZLER pulse measurements

synchronized to the laser system by the signal that control the Pockels cell in the regenerative amplifier. A appropriate delay was introduced by a time delay generator.

The cross-correlation corresponded in our case to the temporal intensity measurement of the shaped pulses, because the gate pulse was much shorter than the DAZZLER pulse. The resolution was about the duration of the gate optical signal (20 fs). We used the numerical code to calculate the optimal phase and amplitude modulation for the DAZZLER. With the amplitude modulation we corrected also the non-perfect flat response of the DAZZLER.

Before starting the measurements, the intrinsic dispersion of the crystal had to be compensated. In fact the 2.5 cm TeO_2 crystal has a group velocity dispersion of $12 \cdot 10^3 fs^2$ and a third order dispersion of $8 \cdot 10^3 fs^3$. The cross correlation profile between the DAZZLER pulse and the gate optical signal is reported in Fig. 4.8. This profile has been produced by imposing only the compensation of the dispersive effect of the crystal. The duration of the pulse is 100 fs, like the input one. This measurement demonstrated that the crystal dispersion was completely compensated.

We tested also the effect of progressive shift of the delay between the laser pulse and the acoustic wave using the delay generator. In the Fig. 4.9 is reported an not optimized pulse for a delay or 4 μs. It is important to note that the measured temporal intensities are very similar. For much bigger delay the waveform is cut because the acoustic and optical waves don't completely overlap anymore.

Because of the finite length of the crystal (2.5 cm) the maximum theoretical duration of the shaped pulse is 6 ps. To overcome this limitation we used

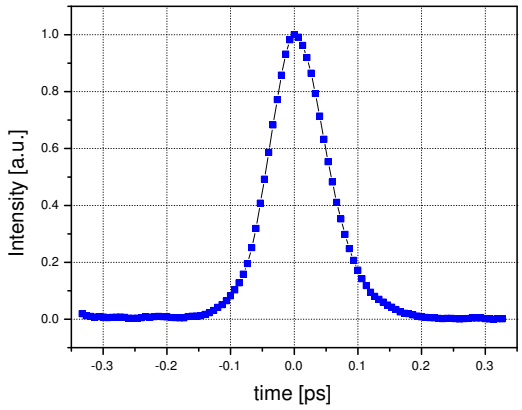

Figure 4.8: Cross-correlation measurement of the temporal profile produced by the DAZZLER when only the crystal dispersion compensation is applied

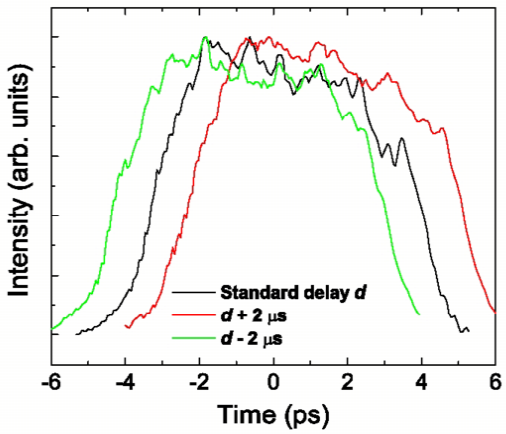

Figure 4.9: Effect of the delay between the acoustic and the optical waves of -2μs (green curve)and 2μs (red curve)respect a reference setting(black curve)

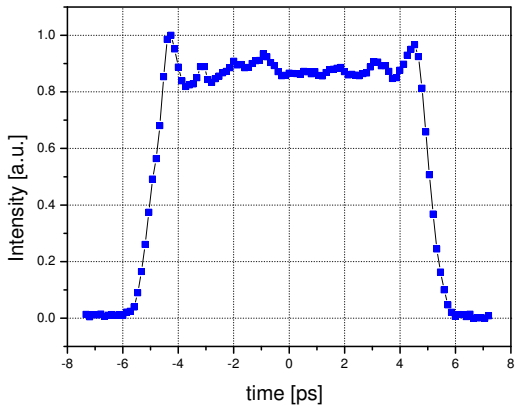

Figure 4.10: Cross-correlation measurement of the temporal profile produced by the DAZZLER for double passage configuration

a configuration in which the laser pulses pass twice through the AO filter. The double passage the AODPF introduces an amplitude modulation that is the square of single pass transfer function. The phase shift, and therefore the maximum pulse length, is doubled.

In this case we observed high energy losses (80%). For this reasons we tested also a configuration with a single pass through the DAZZLER crystal and through 30 cm of dispersive glass (SF57). The glass introduced an extra second order phase modulation. The total dispersion of the glass sections was 0.2 ps^2. In this way the losses were reduced to 50%. The single passage simplified also the alignment of the AO crystal.

In Fig. 4.10 is reported the cross-correlation signal obtained with double passage configuration. The measured pulse shows a very sharp rise and fall time, definitely less than 1 ps, and the pulse duration is about 10 ps FWHM. The ripple on the top of the pulse is very smoothed. The overshoots remains below 15% of the average value of the pulse intensity. The pulse's characteristics obtained are in good agreement with the SPARC requests for the laser pulse profile. In Fig. 4.11 it is shown the input spectral intensity, the phase and amplitude modulation used to obtain the flat top pulse reported in Fig. 4.10. The phase modulation is given by symmetric polynomial expansion up to 8th order centered at 780 nm.

The supergaussian output spectrum has n=9.35, the bandwidth $\Delta\nu$=4.14 THz and the central frequency ν_0=384 THz. The duration of the pulse could be extended up to 12 ps, that is the theoretical limitation of the crystal in double passage configuration. In this case we measured a pulse with large ripple and with rise fall edge overshoots. This effect can be explained by the fact that when the maximum group delay limit is approached the acoustic waveform extends to the edge of the crystal. The acoustic wave truncation

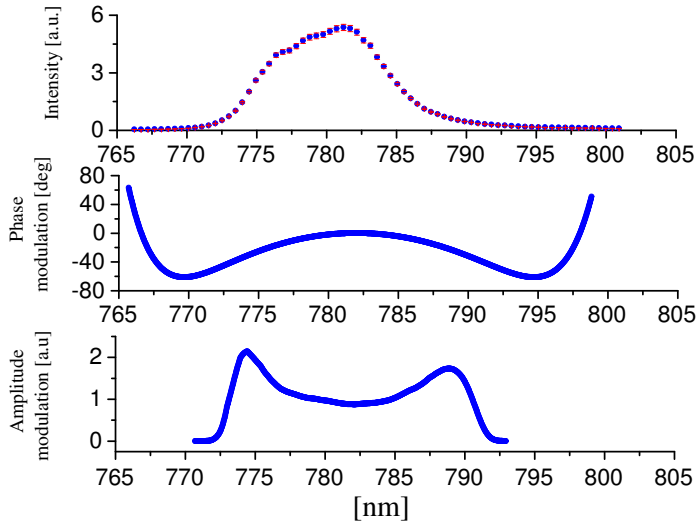

Figure 4.11: In the upper figure is reported the input spectrum. In the middle and the lower plots are reported the phase and amplitude modulation introduced by the AO filter.

can generate deep distortions in the filter function.

In Fig. 4.12 is reported the cross-correlation signal, obtained with single passage through the AO crystal and through the dispersive glass. In this case the rise and fall time is more smooth than the double passage results. The reason is that in this configuration the DAZZLER dynamics is reduced and the glass introduce only second order phase shift without high orders which are responsible for the rise and fall time duration. However the result still satisfies the SPARC requirements. The duration of the shaped pulse is about 6.5 ps; if a longer temporal pulse duration is requested, it is necessary the insertion of additional dispersive glass.

The results were reproducible with not appreciable differences, over a time scale compatible with the laser source stability. We observed also a very low influence by beam pointing instability of few mrad. This value is much larger than the typical Ti:Sa oscillator performances where the AODPF will be installed. Finally measurements showed that the DAZZLER filter is insensitive to microseconds jitters between acoustic wave and laser pulses. In the SPARC laser layout the Dazzler is placed ahead of the laser amplifier, therefore the final temporal profile of the pulse on the cathode is determined by the successive processes that the pulse undergoes. The effects of amplification, UV conversion and propagation through the optical transfer line have to be taken into account.

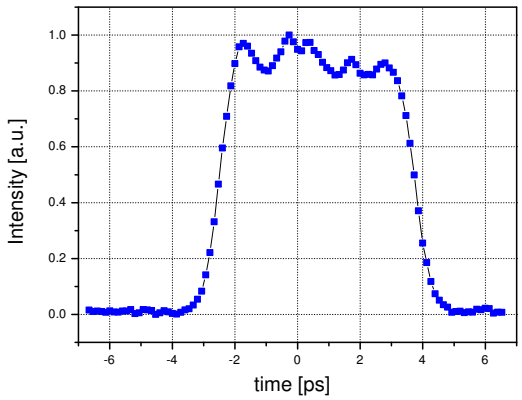

Figure 4.12: Cross-correlation measurement of the temporal profile produced by the DAZZLER for single passage configuration plus external dispersion

4.4.2 Experimental measurement at BNL

With the aim to measure the DAZZLER capability to compensate the distortions introduce by the amplifier and UV conversion, the preliminary measurement have been extended to new tests. They were conducted at the SDL (Source Development Laboratory) at Brookhaven National Laboratory. In this facility there is a Ti:Sa amplified laser system used for drive the photoemission in a rf gun and to produce a seed for the FEL experiment. The laser system is composed by 5W CW diode pumped laser at λ=532 nm to drive the oscillator. The oscillator is a Tsunami by Spectra Physics and produce 100 fs Fourier transform limited pulses at 80 MHz. The central wavelength is 800 nm but the peak emission can be tuned over about 20 nm, the spectral bandwidth can be set between 6 and 12 nm. The oscillator's output energy is 9 nJ per pulse. The DAZZLER crystal was mounted at the oscillator's exit in the single passage configuration with the intent to introduce the external dispersion by not complete pulse compression at the amplifier exit. The stretcher lengthen the input pulse up to 400 ps and the compressor usually is set to produce between 10 to 20 ps pulses. The amplification stage is composed by a 10 Hz regenerative and two multipass amplifiers. Two energetic green pumps are needed to drive the amplifiers. The amplifier's gain is $5 \cdot 10^6$ producing 25 mJ before the compressor. The compressor introduce losses due to high diffraction orders in the gratings and the output energy is 15 mJ. The IR pulse is frequency tripled by two BBO non linear crystals: the first is 0.5 mm long and produces the second harmonic, in the second of 0.25 mm thickness, the fundamental and the second harmonics mix producing the sum frequency at 266 nm up to 1.8 mJ.

For the measurement we used a ps resolution streak camera and a high resolution mono-chromator. The spectro-meter was used to measure the

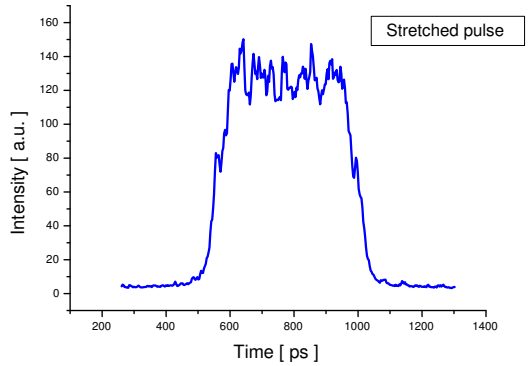

Figure 4.13: Streak camera measurement of the shaped pulse after the stretching.

spectral amplitude of the shaped pulses. In fact as said before the square temporal profile corresponds to a supergaussian spectrum. The steak camera is produced by Hamatsu and has a maximum resolution of 1.5 ps and a spectral response between 250 nm to 850 nm. It can work on 6 time ranges from 10 ps to 2 ns per sweep. We used the Streak camera in synchro-scan mode locking the detector's deflecting rf field to the 80 MHz oscillator pulses. The active detector's gate was synchronized to the synchronization signal sent to the DAZZLER and to the regenerative amplifier's Pockels cell. The temporal intensity measurements have been performed at various position along the amplification chain: after the stretcher, the amplifier and the compressor.

The streak camera measurement was acquired by a computer and the data ware used to improve the DAZZLER's filter function. So far only the amplitude modulation was used, intending to use also the phase modulation for successive fine improvements. The measured temporal intensity corresponds to the spectral distribution because of the external linear of the stretcher and compressor. The second order phase means linear chirp or, in other words, it is the linear temporal dispersion of the spectral components, $d\lambda/dt$=constant. We compared the measured spectrum with the optimal super-gaussian one to produce a new amplitude modulation. To convert the temporal distribution to the spectral intensity we had to calibrate the streak camera to define the coefficient in the relation $\lambda = (d\lambda/dt)\Delta t + t_0$. In fact t_0 and $(d\lambda/dt)$ depend on the position where the measurement is performed, due to the different optical path length to the detector, and on the streak camera scale. To calibrate the streak camera we imposed, in the input spectrum, two holes and then measure their absolute position and distance. In the Fig. 4.13 is reported the time domain measurement after few optimization cycles.

We found the amplifiers and the stretcher-compressor pair introduce distortions on the final time profile. When the pulse in the Fig. 4.13 is amplified

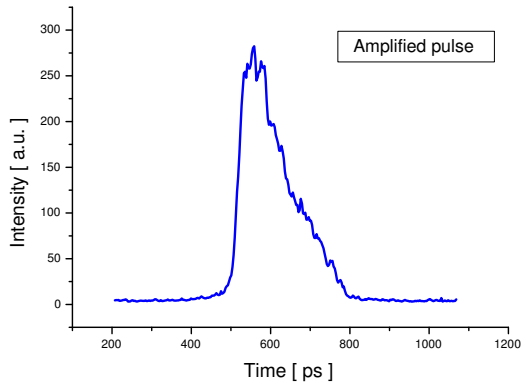

Figure 4.14: Streak camera measurement of the shaped pulse after the stretching and amplification.

we measured the intensity reported in the Fig. 4.14. It is clear the amplification introduce a strong gain narrowing and the lead edge experiences a larger gain that the tail. This behavior is consistent with the amplifier distortion reported in the literature [82]. For a pulse traversing an amplifier its tail sees a inversion of population that has been depleted by its leading part and therefore it experiences lower gain.

We measured also the effect of the compression, using the same input of Fig 4.13 and bypassing the amplification stage. Also the compressor introduced unwanted distortions.

We used the DAZZLER programmable amplitude mask for compensate successfully both the distortions. In the Fig. 4.15 is reported the measurement of the pulse at the exit of the whole chirped pulse amplification chain. The cause of the distortions should be located to obtain better flat top pulse.

As shown in the profile in the Fig. 4.15 the rise time is about 2.5 ps and the ripple are very small. The measured quantity are influence by the streak camera resolution. The measurement of the spectrum showed a strong distortion with two peak at the edges and a noticeable asymmetry. The distortion are found to be introduced by the amplifier and by the compressor's gratings. After their optimization the measurement spectrum downstream the compressor is much more supergaussian, see Fig. 4.16. Up to now we have not measured the intensity profile but according to the simulation presented it should have more shorter rise time than the time profile reported in Fig. 4.15.

Anyway we point out the pulse profile will be optimized with sharper edges with the DAZZLER control of the high orders phase. The results are very promising and should be completed with the measurement after the UV conversion. In the ideal case the frequency tripling produces the cubic power of the input, and therefore should make the rise and fall time shorter.

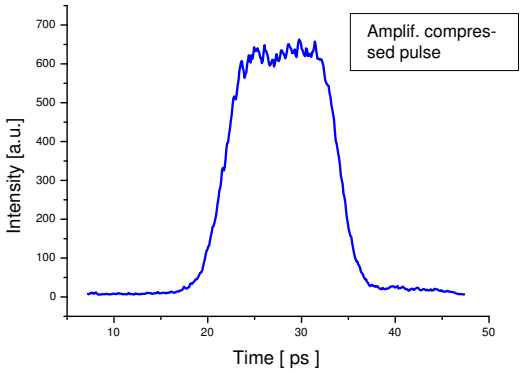

Figure 4.15: Streak camera measurement of the shaped pulse after the stretching and amplification.

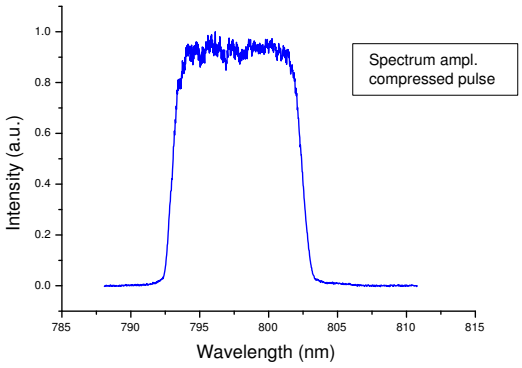

Figure 4.16: Spectral intensity after the amplification and the compression

Obviously the ripple on the top will be enhanced.

To optimized the output UV pulse shape it is required a diagnostic whose resolution is better than the streak camera's one. For this purpose a multi-shot UV cross correlator can be used. This technique is conceptually similar to the one employed in the DAZZLER preliminary measurements but in this case the gate IR pulse from the oscillator should mix with the UV shaped pulse to produce the down conversion frequency.

Moreover it will be useful a complete-automatized control of the DAZZLER using the feedback from the UV diagnostic. The optimization of the filter transfer function based on the genetic algorithm is under development.

Chapter 5

Photocathode Studies

5.1 Photocathode technology for high brightness photo-injector application

The photo-injector is based upon the production of electron bunch via photoelectric effect. A laser pulse impinges on the cathode and stimulates the emission of charge that is quickly accelerated by high electric field. The availability and reliability of the photo-injector are primary concerns and they must be considered before selecting the photocathodes (PC). Depending on specifications high charge per bunch or high mean current, different setups can be chosen, and these are, obviously, defined by the PC materials [28].

The photo-emission threshold is the photon energy required to emit electron from a PC. This parameter will define the laser wavelength. The quantum efficiency or yield (QE) is the ratio of the number of extracted electrons per the amount of the incident photons. This parameter set the laser output power. The PC's vacuum requirements and sensitivity to the electric field will define the kind of gun.

Unfortunately there exists no PC versatile enough to fulfil all requirements. Compromises must be made to suit the particular application. At the present the PC certainly represents the weak point of a photo-injector and a worldwide strong R&D programs are going on to produce an emitter as reliable as a thermionic cathode.

In this chapter we will focus on photocathodes' technology and on the studies conducted on various cathodes for high bright e-beam application. We measured the emission properties of robust photo-emitters: CVD (Chemical Vapor Deposition) diamond-based materials and metal photocathode as well. In particular we tested the emission properties of Mg film. As said before Mg is a metal with an high QE but it has uniformity emission limit, it cannot be easily handled, and there are proofs of adhesion problem on the substrate under high electric field conditions. This limitations motivated an R&D program on Mg film deposited by pulsed laser ablation (PLA) and by

sputtering. The film deposition techniques assure more uniform morphology and they should strongly bonds at between the cathode and the substrate and.

There are many different photo-emitters each combining different processes associated with the photoemission, we will discuss here only the three PC types widely used in accelerator e-sources: metallic, alkali alloys and activated gallium-arsenide.

5.1.1 Metallic photocathodes

These cathodes seem very attractive because they are easy to produce; they can be transported and installed in ambient air; in principle they have an infinite lifetime and a extremely fast relaxation time (typically femtoseconds [83]); in addition, they are able to withstand high electric gradient and poor vacuum conditions. In practice these benefits are not fully realized due to the difficulty to access direct to the metal itself. In many cases it has chemical contaminants on the surface that are detrimental for photoemission properties. An in-situ cleaning treatment, in general with an electric field and laser light must be performed before it can be used. The cleaning must be repeated at a frequency which depends on the vacuum level and the extracted charge.

The low QE (from 10^{-7} to 10^{-3}) observed in these photocathode is limited by various factors. Due to the high reflectivity of metals (30 to 90 %), only a small amount of photons can be absorbed; due to high electron-electron scattering in the conduction band, only a small fraction of created photoelectrons can reach the vacuum interface with sufficient energy (few electrons per thousand). Finally the high work function of metals requires energetic photons to release photoelectrons (3-5 eV). This leads to the use of UV light (200-300 nm) which increases the laser power specifications according to the efficiency of the frequency-conversion process (typically 10-20%). The laser energy density should be maintained below the plasma generation level, therefore the total emitted charge density is limited below few nC/mm^2 in ps laser pulse regime. The emitted mean current is limited to a few μA by the available mean laser power. Currently, in the ps or sub-ps regimes, magnesium with a QE after conditioning greater than 0.1 % seems to be the best metallic PC for producing 1 nC electron beam [84]. Copper cathode demonstrated a QE lower than Mg but higher robustness to high electric gradient. Lead and niobium are studied to develop superconductive RF guns for their superconductive behavior.

5.1.2 Alkali compound photocathodes

In semi-conductors or insulators photocathodes, the conduction band is almost or completely empty. Absorbed photons promote photoelectrons from the valance band to at least the conduction band if the photon energy is larger

than the band gap E_G. Therefore in this material the electron-electron scattering probability is very low. To escape into vacuum the photoelectron must have enough energy to overcome the electron affinity E_A which corresponds to the energy gap between the vacuum level and the conduction band. Then, the photoemission threshold is (E_G+E_A). Qualitatively, the ratio E_G/E_A gives an indication of the QE: in general, the higher the ratio, the better the QE. Therefore, it is desirable to produce insulators or semi-conductors with $(E_G + E_A)$ as low as possible and E_G/E_A as large as possible. This has been done extensively for the last 60 years mainly for photo-tube developments [85]. Some alkali-halides such as caesium-iodide (CsI) have been tested in both DC and RF guns, but the photoemission threshold was too high ($\sim$6 eV) requiring an impractical laser wavelengths. Coating the CsI with a thin layer (2 nm) of Ge has been shown to improve the QE at λ=262 nm [86] however, currently Mg cathode appears to give better results.

The compounds of the alkali-antimonide family (Cs_3Sb, K_2CsSb, Na_2K-(Cs)Sb, etc.) work even with the visible wavelength with a QE approaching 40% and are stable for many years in photo-tubes. Unfortunately it has not been possible to achieve such results in a photo-gun where QE decrease in few minutes down to 1%, producing a significant dark current and limiting the peak electric field.

In spite of a strong R&D program, these drawbacks are not yet overcome. Recently, a new proposal called Secondary Emission Enhanced (SEE) PCs [87] might overcome these disadvantages. It consists of an alkali-antimonide cathode isolated from the rest of the gun by a thin diamond disk, transparent to photons and electrons, and used as an electron multiplication electrode.

Another family, alkali-telluride photocathodes (Cs_2Te, Rb_2Te, RbCsTe, K_2Te, KCsTe etc.) have been demonstrated to behave more favorably in a photo-gun [86] despite requiring UV light (the photoemission threshold is 3.5-4 eV) . These PCs were intensively used at DESY in the Tesla Test Facility about 12 cathodes in 4 years [88], and at CERN in the CLIC Test Facility about 65 cathodes in 10 years [89].

As with the alkali-antimonides, alkali-tellurides must be prepared in an ultra-high vacuum (UHV) environment and they have to be installed without breaking it. This means the use of an UHV transport carrier if the preparation chamber is not attached to the photo-injector.

The preparation consists of firstly evaporating a thin layer of tellurium (about 10 nm) followed by the evaporation of caesium until the photocurrent, produced by the UV light, reaches a maximum. By evaporating both products at the same time following the so-called co-evaporation process [90].

5.1.3 Activated gallium-arsenide Photocathodes

A semi-conductor type III-V with a negative electron affinity (NEA) given by co-adsorption of caesium and oxygen, is well known as an efficient photo-emitter in the visible and near infra-red region [85]. P-doped Gallium-

Arsenide crystals with different doping are the most popular material for producing polarized electrons when they are illuminated with a circularly polarized light.

5.2 Theory of the photoelectric effect

The photoemission effect was observed the first time in the 1897 by Hertz using a simple apparatus composed by two parallel plates in vacuum polarized by DC voltage. When one of the plate was illuminated by radiation at a certain wavelength a current was observed. The experiment contributed to the development of the quantum physics. In fact according to the observation that the electron emission was governed by the radiation wavelength and it was not influenced, as the classical physics postulated, by the radiation intensity, Einstein explained the photoelectric effect by the interaction of a quantized energy, photon, and an electron in the solid. The electron emission is caused by the instantaneous absorption of a photon with energy $h\nu$ larger than the characteristic energy of the material, called work function Φ.

For high intensity coherent radiation the emission of an electron can be produced by the absorption of two or more photons; in this case, the process is called multi-photon photoemission. Thus the emission occurs also with photon's energy lower than Φ. Therefore if the multi-photon effects are included, the emitted charge can be expressed as:

$$Q = \sum_k M_k I^k \tag{5.1}$$

The zero order is the thermionic electron emission and the other terms are the emission contribution of the k order photoelectric process.

The electron, as said before, is emitted when it absorbs energy larger than the work function. To describe this parameter is useful to refer to the band model of a crystalline solid. The work function is equal to the difference between the energy of the vacuum level E_0 and the energy of quantum state where the electron is localized before the absorption. In general it is more practical to refer to a average initial level, as the Fermi's level E_F:

$$\Phi = E_0 - E_F \tag{5.2}$$

The Fermi level is the maximum energy of the electron in the solid a the temperature T=0° K. It is well known that the energy of the electrons are distributed according to the Fermi Dirac function:

$$F(E) = \frac{1}{1 + \exp(\frac{E - E_F}{k_B T})} \tag{5.3}$$

Where k_B is the Boltzmann constant; the change of the temperature induces a tail in the distribution above Fermi's level. The second parameter useful

to characterize the photoemission is the electron affinity defined in the case of the semiconductor as:

$$\chi = E_0 - E_c \tag{5.4}$$

where E_c is the minimum level of the conduction band. For the conductor material the electron affinity is equal to the work function. The band of a crystalline solids are derived by the assumption that the material is a tri-dimensional matrix without boundaries. In the reality the surface of introduced complex structured superficial bands. If the material is terminated with a layer of a different material the band structure are altered and the χ can be reduced. A favorable arrangement for the photoemission is obtained when a p-semiconductor is covered by a thin layer of n-doped material. Because of at the p-n junction the bands are down-bent the electron extraction becomes more probable. In some case it can be produced negative electron affinity (NEA) cathodes.

The phenomena involved in the photoemission from a solid are not completely understood. In this section we will describe two simplified models: the Three Steps model and the Fowler Dubridge theory extended to multi-photon case. The models are very intuitive and introduce strong simplifications. Nevertheless they have been proved to be consistent with the experimental measurement and quantum-mechanics treatments [91, 92].

5.2.1 Three Steps model

The Three Steps model [85] allows to quantify the number and the kinetic energy of the photoelectrons as the probability composition of the three steps involved in the photoemission:

1. the photon absorption by an electron which is promoted to higher energy level,
2. the electron's drift to the vacuum interface,
3. the overcoming of the surface energy barrier.

The emission will result the composition of each step's probability. An useful picture of the three step can be obtained by band model of a solid. The first step can be thought as two particles' collision electron-photon with the conservation of energy and momentum. The excited charge jump from the initial level to final one (E_i, E_f). The probability per unit of time of the transition from the initial state to the final one is associated to the element of the matrix of the electric dipole $m_{i,f}$. For direct transition, absence of reflection, the probability of absorption is the sum of probability on all the possible initial and final states:

$$N(E, k, h\nu) \propto \sum_{i,j} |m_{i,j}|^2 \cdot \delta(E_f(k) - E_f(k) - h\nu) \cdot \delta(E - E(k)) \tag{5.5}$$

E is the kinetic energy of the emitted charge, k is the crystal momentum, the last Dirac functions come out from the energy and the momentum balance.

The second step is related to the energy losses processes that the excited electron can experience in the drift to the surface. In particular it can collide with other electron, especially for the metal, and with atoms, prevailing phenomenon for the semiconductors. According to [92] the probability, or transport coefficient, the electron emerges to the surface can be expressed in term of mean free path λ_c. This parameter is the average length between two collision. Assuming some simplifications [92], the transport coefficient, d, for an electron with kinetic energy E and momentum k , is expressed as:

$$d(E,k) \approx \frac{\alpha\lambda_c}{1+\alpha\lambda_c} \tag{5.6}$$

where α is the radiation absorption length of the material. High efficiency photoemission is achieved when the absorption length equals the free mean path. In general the emission has a very low probability for electrons that suffer for collisions.

In the third step we introduce the probability of the electron to overcome the surface energy barrier. The probability is 1 if the perpendicular to the surface, kinetic energy is larger than the electronic affinity:

$$\frac{\hbar}{2m}\cdot k^2\cos^2(\theta) \geq E_0 - Ec \tag{5.7}$$

being θ the angle between the electron velocity vector and the normal of the surface.

$$\cos^2(\theta) \geq \sqrt{2m\frac{E_0-Ec}{k^2}} = \cos\theta_0 \tag{5.8}$$

The surface electron transmission depends on its kinetic energy and direction:

$$|t(E_f,k_\perp)|^2 = \begin{cases} 1 & if \quad \theta < \theta_0 \\ \\ 0 & if \quad \theta > \theta_0 \end{cases} \tag{5.9}$$

To summarize the total emission probability is:

$$N(E,k,h\nu) \propto \sum_{i,j} |m_{i,j}|^2 \cdot |t(\theta)|^2 \cdot \delta(E_f(k) - E_f(k) - h\nu) \cdot$$
$$\cdot\delta(k_{//} - p_{//}(\theta,\varphi)) \cdot \delta(mv - mv_0 \pm \frac{h}{d}) \cdot \delta(E - E(k)) \tag{5.10}$$

Beside the terms justified before, the equation 5.10 expresses the conservation of the energy and of the momentum law including the quantized phonon of the crystal matrix $\frac{h}{d}$.

5.2.2 Single and multi-photon Fowler Dubridge model

The second model is based on the pioneering works published by Fowler and Dubridge [95, 96]. It is an useful tool to characterize the emission law around the threshold, for a metal. The successive extension to the multi-photon will be presented [97]. The model calculates the emitted charge as function of the incident radiation intensity, the wavelength and the temperature. The Fermi-Dirac electron distribution is assumed. Other semplifications are:

1. the absorption rate is independent on the initial state and it only increases the normal kinetic energy's component;
2. the electron overcomes the surface barrier if the normal component of its kinetic energy is larger than the χ;
3. the emitted charge is proportional to the number of electron with energy in the final state larger than E_0.

Near the emission threshold at ambient temperature the number of emitted electron is:

$$N = \frac{2\sqrt{2\pi m^{\frac{3}{2}}}}{h^3(E_0 - h\nu)} \cdot KT^2 F\left(\frac{h\nu - \phi}{kT}\right) \tag{5.11}$$

where K is the Boltzmann constant, and F(x) is the Fowler function [95]. In the case of single photon emission the current is proportional to the radiazion intensity. For coherent radiation the emission can occur also at $h\nu < \phi$, and the condition 2 becomes:

$$E_\perp \geq E_0 - n \cdot h\nu \tag{5.12}$$

where n is the order of the process. The current emitted is expressed as:

$$J = \sum_{n=0}^{\infty} J_n = \sum_{n=0}^{\infty} \sigma_n I^n \tag{5.13}$$

where σ_n is a semi-empirical coefficient obtained assuming the Fowler Bubridge semplification.

Photocathode parameters for photo-injector application

As said before the emittance of the electron beam is usually expressed as the sum of the radio frequency electric field emittance ϵ_{rf}, the space charge emittance ϵ_{sc} and the thermal emittance ϵ_{th}:

$$\epsilon^2 = \epsilon_{th}^2 + \epsilon_{sc}^2 + \epsilon_{rf}^2 \tag{5.14}$$

The thermal emittance depends on the photocathode material and the laser photon energy. It represents the theoretical minimum, that is possible to achieve in an ideal photo-injector.

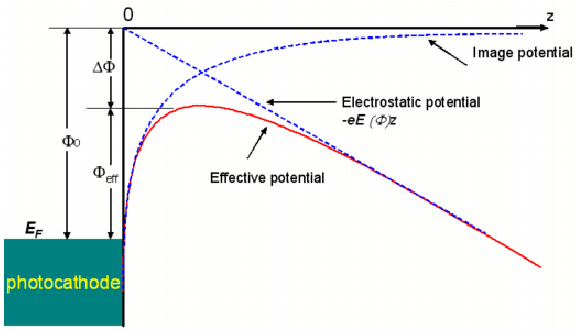

Figure 5.1: Picture of the Schottky effect for a metal photocathode.

$$\epsilon_{th}^2 = \frac{1}{m_0 c}\sqrt{\langle x^2\rangle\langle p_x^2\rangle - \langle x \cdot p_x\rangle} = \frac{x_{rms}}{m_0 c}\sqrt{2m_0 E_{kin}} \tag{5.15}$$

The electron kinetic energy, as shown before, is proportional to the difference between the photon energy $h\nu$ and the PC bulk work function.

$$E_{kin} = h\nu - \Phi \tag{5.16}$$

When an accelerating electric field is applied the surface energy barrier, image potential, is down-bent respect, see Fig. 5.1. This phenomenon, known as Schottky effect, favors the electron extraction [98]. For a sinusoidal accelerating electric field E(φ) whit phase φ the effective work function Φ_{eff} is:

$$\Phi_{eff} = \Phi_0 - \alpha\sqrt{\beta E(\varphi)} \tag{5.17}$$

and the kinetic energy becomes:

$$E_{kin} = h\nu - \phi + \alpha\sqrt{\beta E(\varphi)} \tag{5.18}$$

where β is the field enhancement factor and α is a constant typical of the material. For the PC used in the photo-injector the electron kinetic energy is typically between 0.3 and 2 eV and the corresponding ε_{th} is between 0.3 and 1 $mm{\cdot}mrad$. As shown in the equation 5.18 higher photon energy, or higher accelerating field, produce higher thermal emittance photoelectrons. The Schottky effect partially explains also because the QE increases when the laser injection is obtained at grazing incidence. In the SPARC photo-injector the laser shines the photocathode at 72° respect to the cathode normal.

Experimental results [40] using grazing incidence to shine a metal cathode, in which the UV light was changed from p-polarized (electric field nearly

normal to the surface) to s-polarized (E parallel to the surface), have shown 5 to 6 times more photoemission for p. Part of this improvement, a factor of 2.5, is due to the lower reflectivity for p; the balance is attributed to the Schottky effect. This observation leads to the use of the grazing incidence geometry.

If the charge extracted from the cathode is too high, the space charge field can balance the accelerating field and thus no more particle can be emitted by the PC.

At low energy the pulse, as its duration is infinitesimal, can be assimilated to a superficial charge distribution with density ρ_S. According to Gauss law the electric field generated by the charge Q with a Gaussian distribution over a circular surface with radius radius σ is equal to:

$$E_{dec} = \frac{Q}{2\pi\epsilon_0\sigma^2} \tag{5.19}$$

ϵ_0 is the vacuum permittivity. A more detailed analysis takes into account retardation effect by using Lienardt-Wiechert formalism [99]. This approach shows that, for relatively long pulses (longer than 50 ps) the last emitted photoelectrons do not experience the electromagnetic influence of the electron extracted first due to retardation effects. The extractable current density become constant for long pulses and the result are similar to the ones established for a DC diode [31].

The response time is another important attribute of the photoemitters, and it is related to the escape length L_e and the mean electron velocity $\langle v_e \rangle$ [83]:

$$\tau = \frac{L_e}{\langle v_e \rangle} \tag{5.20}$$

For most metal $L \cong 10 - 50\mathring{A}$ and the response times are very fast, typically femtoseconds, but it can be well into the nanoseconds range for the high QE NEA photocathodes ($L \cong 10^4\mathring{A}$) [100]. In general the response time correlates to the QE: higher QE implies grater escape length and thus longer relaxation time.

Therefore the temporal flat top laser pulse should be coupled with fast response cathode for effective non-linear space charge emittance compensation.

5.3 Quantum efficiency measurements

The photoemission experiment have been performed using a Q-switched mode-locked Nd:YAG amplified laser QUANTEL mod. YG501. This source delivers about 25 ps pulses with maximum energy of 30 mJ at the fundamental wavelength: 1064 nm. The laser consists of a lamp pumped oscillator with electro-optics mode locker and a dye saturable absorber to obtain Q

switched pulses. The oscillator delivers a raster of about ten pulses, with transverse mode TEM_{00} spaced by 12 ns, whose intensity is distributed in the Lorentian bell. A Pockels cell, a $\lambda/2$ waveplate and a Glan-Taylor prism act as pulse picker and select one pulse for the amplification. The Pockels cell is triggered by a photodiode measuring the macropulse from the oscillator. Changing the level of the trigger it is possible to control the delay of the Pockels cell to select the maximum intensity pulse. The amplifier's gain is 12 and produce circular polarized pulses. The repetition rate can be set at 1, 5 or 10 Hz. To modify the laser pulse energy one can vary the delay of the amplifier lamp respect to the oscillator's one, changing the population inversion level when the pulse enter in the amplifier crystal.

To study the photoemission efficiency in the metal the fourth harmonics has been employed with photons' energy of 4.66 eV. For diamond-based cathode the photon energy was extended also at sub-threshold energy using also the second and third harmonics of the laser, at photon energy of 2.33 and 3.5 eV respectively. To generate the harmonics of the fundamental wavelength an external generator is employed. The second harmonic is obtained in a 35 mm long KD*P (KD_2PO_4) crystal where it is achieved the type II phase matching. To produce the third harmonics a second KD*P crystal is added. In the second crystal the fundamental wavelength mixes with the second harmonic generating photons with energy equal to the sum of incoming photons. To obtain the fourth harmonics the second KD*P is replaced with 12 mm long BBO crystal ($\beta - BaB_2O_4$) that acts as the second harmonics crystal for the input wavelength at 532 nm. After the second non-linear medium the different wavelengths are superimposed and a Pellin Broca prism is required to deflect the frequencies along different directions. To tune the phase matching condition the temperature of the crystal is kept constantly at 40^0 by a thermostat. The double conversions process in the experimental conditions showed a efficiency of 10%.

Four mirror, two for the IR and two for the high harmonics are used for the beam steering. The laser beam illuminated the cathode area of approximately 2 mm^2 at 0° incidence angle. A DC negative voltage up to 6 kV has been applied to the cathode, a faraday cup anode collected the emitted charge [93]. The anode is wired to a 1.5 GHz oscilloscope to measure the photoelectron. The cable is a coaxial terminated on 50 Ω. The anode consists of a 100 μm mesh with wires 20 μm of thickness, installed at 3 mm from the cathode plate; the mesh is transparent to the laser beam but it intercepts the emitted electrons. Therefore the accelerating field reachs 2 MV/m.

The cathode and the anode are mounted inside a chamber at vacuum level of 10^{-6} mbar to avoid electrical discharge. The laser input port is composed by a fused silica windows, material that is transparent at the wavelengths used in the experiment. The emitted charge that are not intercepted by the mesh are collected by an aluminum cylinder behind. A permanent magnet generating a field of hundred Gauss is required to deflect all the electrons to the cylinder. For the metallic cathode measurements it has been constructed

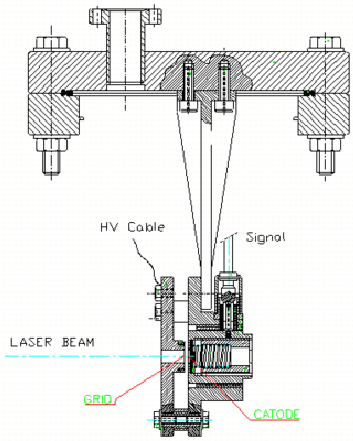

Figure 5.2: Rendering drawing of the cathode holder

a UHV (*Ultra High Vacuum*) chamber to slow down the oxidization rate of the emitter. The vacuum level is constantly below $5{\cdot}10^{-8}$ mbar in the operating conditions. Because the permanent magnet is not compatible with UHV environment, to collect all the photoelectrons a positive voltage has been applied to the anode and the signal was picked by a coaxial cable on the cathode, see Fig. (5.2). In this case the measured signal is a positive waveform and but the detected charge remains unchanged. The cathode is mounted by a spring and the layout is compatible to back illumination experiment.

The measured emitted charge has to be compared with the corresponding laser pulse energy. To accomplished this task a thin BK7 beam splitter at 4% of reflection samples part of the beam before the vacuum chamber. The reflected radiation has been directed toward a diffuser and 1GHz PIN photodiode. Because the photodiode does not gives an absolute energy value, the device has been previously calibrated using a pyroelectric Joulemeter Molectron mod. J3-05 DW placed at the vacuum chamber entrance. The energy and emitted charge waveform measurement system have bandwidth limited. The finite spectral response reduce the pulses length but doesn't change the integral of the signals. The area of the signals are the quantities required: the charge $Q = \int i(t)dt$ and the energy is defined as $E = \int I(t)dt$, where i(t) and I(t) are the current and the intensity of the laser pulse respectively. The waveform acquired by the oscilloscope are recorded by a virtual instrument developed in Labview environment. The software subtracts the bias, calculate the area of the waveforms and multiply the results for the calibration constant.

As pointed out before, the metal surfaces suffer from oxidation processes. To remove the oxide layer it was developed a cleaning procedure based on high power density laser. Practically a focus UV laser beam was used to scan the cathode's surface to remove the oxide [94]. The measurement of the photoelectron waveform was an important parameter to understand the effectiveness of the laser cleaning. In fact when the laser produce an ablation of the oxide layer, electrons and plasma are extracted. The ions contribute to lower the space charge effects and the measured electrons pulse shows a long tail. It was found that to produce an effective laser cleaning the density of 100 μJ over a spot size of 0.3 mm diameter is required. To focus the beam a 600 mm focal lens was installed on a flip mount.

To automatize the cleaning procedure the last mirror placed at 80 cm from the cathode, was mounted on a gimbal holder. Two DC motor driven by a PCI controller card were used for the positioning of the beam along the horizontal and vertical axes. It was developed a software to control the parameters of the motion system and to move independently the two motors. To check the laser centroid and to find the proportional constant between the motors' movement and the position on the emitter a virtual cathode was built. The virtual cathode is a surface placed placed at the same distance of the cathode surface from a beam sampler. To record the beam position it was used a silicon CCD digital camera connected directly to a PC trough a firewire IEEE 1394 bus. The camera was synchronized with the laser system by a TTL signal.

5.4 Diamond-based photocathodes

Poly-crystalline diamond films obtained by CVD (Chemical Vapor Deposition) have been widely investigated as photo-emitting materials for their chemical inertness, high radiation damage threshold, and relatively high yield with near-UV radiation [101, 102]. The high yield is determined by the diamond property of low or negative electron affinity (NEA) when terminated with hydrogen [103]. The characteristics of these films with regard to photoemission depend on the growth process, which determines the defects of the diamond grains and the co-deposition of non-diamond phases, such as amorphous sp2-C (a-C). The defects in the crystal create levels and even bands within the valence-conduction gap. The non-diamond phases are formed on the boundaries of the grain [104, 105].

The requirements for the emitted bunches are a high charge (nC), a short duration (a few ps), and an high stability of the characteristics from pulse to pulse. From these requirements follow the corresponding characteristics of high intensity and stability of the laser pulse. A linear curve of charge versus laser intensity is preferred for the stability of the emitted charge.

5.4.1 Diamond film deposition and structural characterization techniques

Diamond deposition was carried using a modified hot-filament CVD apparatus coupled to a powder-flowing system. The diamond films were generated through the activation of CH_4/H_2 mixtures, using a CVD apparatus [107]. They were deposited on α-Ti substrates, and the deposition runs lasted 2 h (see [93] for complete information). The filament temperature was kept at 2200 °C, the methane concentration was 1% of the H_2 amount. The film thickness were on the order of 1-2 μm. All of the films consisted of good quality poly-crystalline diamond, with a texture partially oriented towards the $\langle 110 \rangle$ direction. All of our samples are probably terminated with hydrogen, due to the intrinsic experimental conditions of the CVD process.

The deposition substrate temperature was varied between 650 and 750 °C in order to study the effect of variable amounts of the amorphous carbon (a-c) phase. At least 2 films were synthesized under each set of experimental conditions.

For diamond, the energy gap between valence and conduction band is quoted 5.5 eV for an indirect transition and 7 eV for a direct transition [108, 109]. With the aim to reduce the material work function it was introduced Nitrogen and Neodymium dopants during the deposition process [110]. For Nd-doped diamond films, Ar streams have been employed to carry Nd-acetylacetonate powder inside the reactor, across the reactive area of the substrate to where diamond was growing by activation of methane/hydrogen mixtures. For N-doped diamond films N_2 and Ar streams have been employed whit two different rates 30-50 sccm.

The choice of introducing Nd and N inside diamond was made on the basis of the following considerations. The N-doping was thought to be effective in improving the emission properties, due to the introduction of a level at 1.7 eV below the CBM (conduction band minimum) of diamond [102]. This energy level would improve the electron photoemission even with photons in the visible range. By inserting Nd, the diamond-based material becomes conductive and an acceptor level is introduced at 0.1 eV above the valence band maximum (VBM) [111]. In this case, an enhancement of the emission efficiency due to a downward band bending at the surface could be expected, as it happens with Boron doping.

Routinely scanning electron microscopy (SEM), reflection high energy electron diffraction (RHEED), and Raman spectroscopy were used to control the morphology and structure of the films produced. The Raman spectra were obtained at room temperature in the back-scattering configuration using an Ar-ion laser beam (514 nm, laser power 130mW). The RHEED analyses were performed using an electron microscope (AEI EM6G) equipped with a high-resolution diffraction stage and operating at 60 kV.

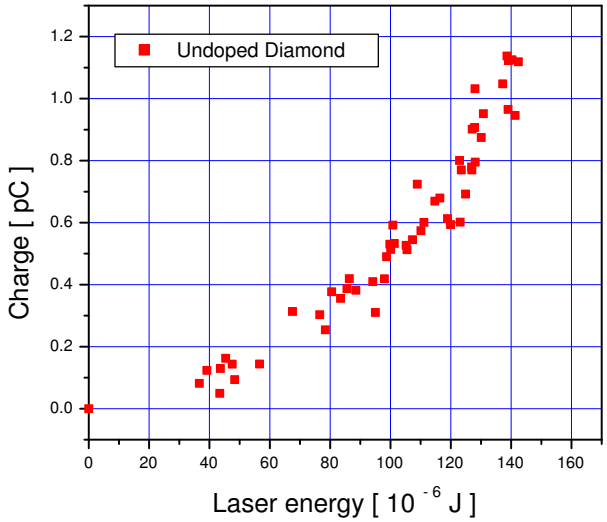

Figure 5.3: Undoped diamond charge emitted vs laser pulse energy at λ=532nm. The emission curve can be approximated with a polynomial with order higher than 2.

5.4.2 Quantum efficiency measurements

The photoemission measurements from diamond films at the green wavelength (2.3-eV photon energy) proved to be difficult, because of the very low emitted charge. Such difficulties have also been experienced in the case of diamond films containing impurities N, introduced with the aim of creating spurious levels in the diamond gap. The emission efficiency was always very low and the Fowler polynomial fitting indicated, in any case, an order of the multi-photon process larger than two. The results confirmed that the introduction of N dopant doesn't enhance the QE that is more sensible to the amorphous carbon content and the crystalline quality of the diamond. The measurement indicated that the presence of Nd doesn't change the photoemission properties of the diamond films. Beside the surface composition is one of the most important factor to obtain poly-crystalline diamond film with high quantum yield. The presence of nitrogen in the deposition process worsen the quality of the diamond matrix and increase the amount of a-C. The emitted charge vs laser pulse energy, observed for un-doped diamond film sample 1, is reported in fig. 5.3.

Because the quantity of a-C seems to have influence on the QE we tested the photoemission at 2.3, 3.5, and 4.7 eV from a variety of diamond layers containing different amounts of co-deposited amorphous sp^2-C (a-C) [112]. The results can be summarized as follows. At 3.5 eV and 4.7 eV we found both two-photon and one-photon emission, the predominance of either pro-

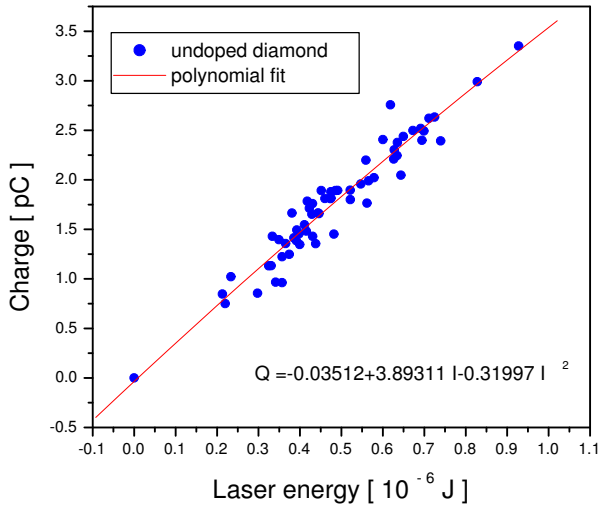

Figure 5.4: Undoped diamond charge emitted vs laser pulse energy at λ=266nm.

cess being dependent on the amount of a-C in the films, and obtained rather high values for QE. At 3.5 eV we measured efficiencies up to 0.01 pC/μJ^2 in the two-photon regime [93]. More linear curves were obtained at 4.7 eV, with a linear emission coefficient on the order of 4 pC/μJ. A plot of the emitted charge vs. radiation energy at 4.7 eV for the diamond film sample 1 is shown in fig. 5.4. Here it is reported the second order polynomial fit that shows the first linear term is the most important. Instead the second order term is negative and takes in account the space charge saturation effect. The zero order hasn't physical interpretation and comes out from measurement's error.

A structural investigation was performed by Raman spectroscopy and RHEED in order to correlate the yield and the order of the emission process with the relative abundance of the a-C phase with respect to the diamond phase. In fact the Raman spectroscopy allows to deduce the amount of the C phase and the RHEED result indicate the level of C in crystal form (diamond). For all of the samples, the decomposition of the Raman spectra gave the diamond peak centered at about 1332 cm^{-1}(diamond peak), two broad Raman bands at 1550 (G band) and 1350 cm^{-1} (D band) associated with diamond-like or a-C, and a broad band at about 1480 cm^{-1}, also ascribed to the presence of amorphous C phases [113, 114]. In the Raman analysis the amount of the a species must be normalized to its scattering efficiency. In our case the diamond scattering efficiency at 1332 cm^{-1} is 50 times smaller than a-C phases [115].

To obtain film with different diamond/a-C ratio we deposited the film at different substrate temperature. In Table 5.1 are reported the Fowler co-

T (°C) (sample)	a-C	M_1 [pC/μJ]	M_2 [pC/μJ^2]
650 (2)	1	$6 \cdot 10^{-7}$	$2.6 \cdot 10^{-3}$
650 (3)	1.012	$7 \cdot 10^{-7}$	$2.6 \cdot 10^{-3}$
700 (4)	1.022	$5 \cdot 10^{-3}$	$4 \cdot 10^{-3}$
700 (5)	1.028	$1.1 \cdot 10^{-1}$	$6 \cdot 10^{-3}$
750 (6)	1.054	$1.7 \cdot 10^{-2}$	$6 \cdot 10^{-3}$

Table 5.1: Photoemission behavior for different amount of amorphous carbon obtained by varying the deposition temperature.

efficients M_1 and M_2, representing the efficiencies of one and two photon processes, for cathodes with various a-C content illuminated by 4.7-eV radiation. In the same table one can find the corresponding content of a-C, as evaluated from the Raman analysis. The a-C amounts reported are given normalized to the a-C content of sample 2, taken as the reference value. The data indicate that both the efficiency and linearity of the process increase with increasing a-C content up to a certain value, but tend to strongly decrease for further increases of the a-C phase.

The correlation between photoemission behavior and a-C content has been tested by performing experiments on homogeneous layers of amorphous carbon, generated by electron beam irradiation of hydrocarbons. The emission curves at 4.7 eV from these carbon layers indicated a net two-photon process and a low efficiency on the order of 10^{-4} pC/J^2.

In order to evaluate the effect of the diamond/a-C surface ratio on the photoemission properties of the diamond films, systematic measurements were carried out on a number of samples submitted to a process of selective etching of the surface a-C phase. For these experiments we chose the samples grown at 700 °C, characterized by the best photoemission performances, and a sample grown at 750 °C containing a higher amount of a-C. The treatments were performed for periods ranging from 2 to 12 hours at room temperature using a 20 wt.% HNO_3 solution, which is known to remove carbonaceous species without damaging the diamond crystallites. The etched samples were thereafter submitted to Raman and RHEED analysis, in order to probe the material at different depth scales. The Raman spectrum for the diamond sample 7, before and after 12 hours etching, is shown in fig. 5.5 and corresponding QE measurement is reported in fig. 5.6.

The comparison of the Raman spectra taken before and after the etching procedure reveal for all of the samples a significant decrease of the signals ascribed to non-diamond phases and an increase of the diamond/a-C ratio. The RHEED analysis allowed better definition of the structural modifications at the surface, probing the depth to about 50 Å. The RHEED patterns shown in fig. 5.7 reveal for the treated samples a strong decrease of the

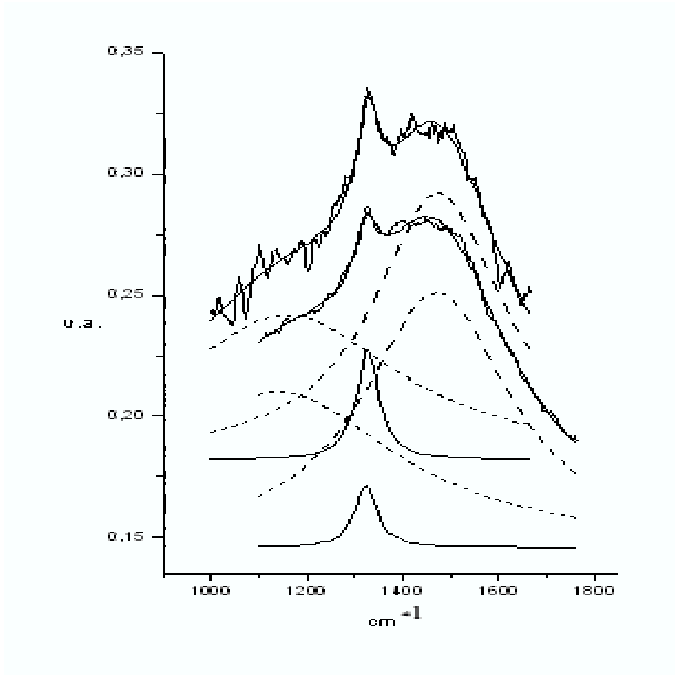

Figure 5.5: Raman analysis on sample 7 before (lower curve) and after 12 hours etching treatment (higher curve).

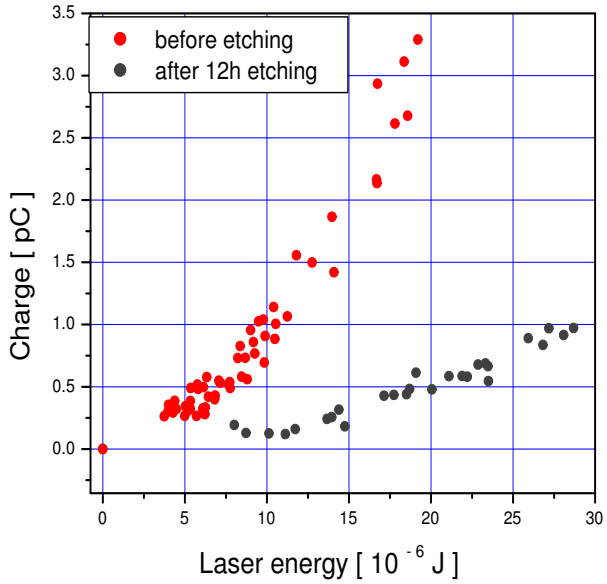

Figure 5.6: Sample 7 charge emission vs laser pulse energy at λ=266nm before and after 12 hours etching treatment.

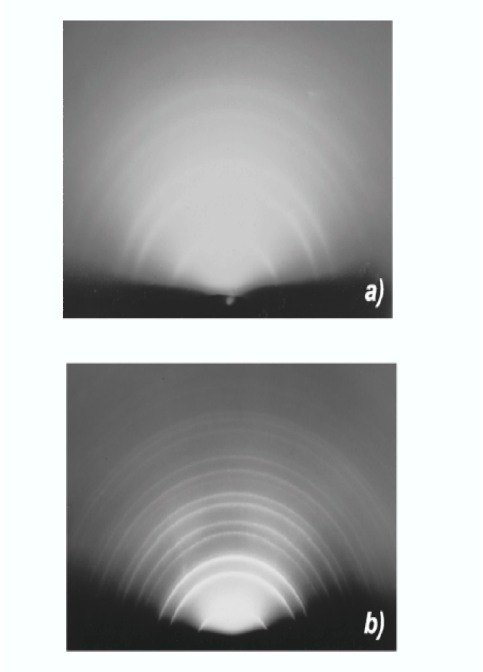

Figure 5.7: Sample 7 RHEED analysis before and after the etching process: upper and lower figure respectively. The more evident rings testify the more regular crystalline structure due to larger amount of diamond.

diffuse background due to the presence of amorphous material and an evident increase of the relative intensity of the Debye rings belonging to the diamond phase.

The effect of the etching procedures on the photoemission properties of our films can be appreciated by comparing in Table 5.2 the Fowler coefficients M_1 and M_2 for the as-grown films and for the same films after HNO_3 treatments carried out for different times. As one can see, the etching by acid of the diamond films grown at 700 °C resulted in a net decrease of both the one- and two-photon emission processes. Conversely, in the case of the sample produced at 750 °C, we noticed after the post-synthesis treatment a slight improvement of the one-photon regime with respect to the two-photon one.

5.4.3 Discussion of the experimental results

The rather high QE values ($\approx 10^{-5}$) obtained for dominant one-photon processes at 4.7 eV indicate both a high absorption efficiency and low affinity of the diamond films. However, it must be considered that an ideal diamond crystal does not allow the one-photon process because of its band gap of 5.5-eV. On the basis of the present results it can be stated that diamond films with a little amount of a-C, as well as those completely covered by an

T (°C)	Sample (hours)	M_1 [pC/μJ]	M_2 [pC/μJ^2]
700 (1)	5	$11 \cdot 10^{-2}$	$6 \cdot 10^{-3}$
	5 (2h)	$2 \cdot 10^{-2}$	$2.5 \cdot 10^{-3}$
	5 (4h)	$9.7 \cdot 10^{-3}$	$1.6 \cdot 10^{-3}$
700 (4)	7	$4.6 \cdot 10^{-2}$	$5 \cdot 10^{-3}$
	7 (12h)	$9 \cdot 10^{-4}$	$1 \cdot 10^{-4}$
700 (5)	8	$6 \cdot 10^{-2}$	$1 \cdot 10^{-4}$
	8 (12h)	$9 \cdot 10^{-4}$	$3.5 \cdot 10^{-3}$
750 (5)	9	$1.7 \cdot 10^{-2}$	$6 \cdot 10^{-3}$
	9 (12h)	$1.5 \cdot 10^{-2}$	$9 \cdot 10^{-4}$

Table 5.2: Photoemission behavior for different amount of superficial a-C obtained by progressive HNO_3 atching of the amorphous phase

a-C layer, emit poorly. The fact that an excess of amorphous C inhibits the process has been confirmed also by photoemission measurements from homogeneous layers of amorphous carbon.

The present results support the hypothesis that photoemission from diamond films is connected to a suitable combination of amorphous carbon and diamond structure and suggest that there is an optimal ratio between the two species that maximizes the QE. Moreover, the strong correlation between the amount of surface a-C and the emission yield leads us to assign the emission to zones of amorphous carbon located on the surface of the crystal grains, and to consider surface processes related to an appropriate distribution of a-C patches.

The possibility of emission from surface zones with different structure has already been illustrated by other researchers [104]. They have described a non-homogeneous emission model, in which emission is attributed to surface patches of graphitic material having a semi-metallic density of states.

Graphite has a high absorption coefficient but its work function of 5 eV does not allow one-photon emission with 4.7-eV light. Diamond, instead, has a very low absorption coefficient at this photon energy (in principle coming only from levels in the gap due to defects) and therefore a very low quantum efficiency (QE) but it can assume negative affinity when H-terminated. Hence the photoelectrons generated in the graphitic zones can easily leave the material (as required by a high QE) via the diamond vacuum level, with an effective work function that can be lower than 4.7 eV. In our case the Raman analysis shows that the amorphous phase responsible for emission is not graphite but a-C. However the features of photoemission from diamond films at 2.3, 3.5, and 4.7 eV can still be explained on the basis of the band diagram of a-C, which presents a gap of about 2 eV between the conduction

and valence band [109].

The yield is high when the a-C zones are on the front surface and surrounded by diamond having low or negative affinity due to hydrogen termination. All of our samples were indeed terminated with hydrogen, due to the experimental conditions of the CVD process employed. The amount and the distribution of the a-C patches on the film surface seem to represent the key factors governing the photoemission performances. As the data in Table 5.1 show, for diamond films with an intrinsic appropriate presence of surface a-C, the removal of the amorphous component always leads to a worsening of the emission and decreases of the M_1 coefficient. The slight increase of the one-photon emission detected after the etching of the film with the highest a-C amount can be rationalized if one considers that the etching process favors the disruption of the larger patches into smaller domains and therefore the formation of an increased number of a-C/diamond junctions. In this picture of the photoemission process, the active surface is very small. For a single-crystal diamond sample, the fraction of the surface area occupied by the a-C patches is reported to be less than 1% [104]. In our case the area of the a-C zones is larger due to the contribution of the grain boundaries. We can reasonably assume it to be on the order of a few percent. It must however be remarked that the active emitting surface is only the portion of the patches close to the borders. Therefore the active area can be much smaller than that of the a-C patches, depending on their size.

The high QE values (10^{-6}) measured over an area of 4 mm^2 and a low accelerating field of 10 kV/cm, indicate that the localized yield should be very high. Considering the small a-C area and the triple-point border effect, we might estimate that the local quantum efficiency is several orders of magnitude higher than that resulting from the integral measurement. The triple-point diamond a-C vacuum creates a very favorable field configuration for the expulsion of photoelectrons from the surface.

The above results suggest that the appropriate strategy for obtaining a high photoemission yield at sub-band gap photon energies is a compromise between increasing the active a-C area with respect to the diamond crystal surface and keeping the effective work function dominated by the diamond phase.

As conclusive remark we may say that diamond based films are robust photoemitters. They do not require laser cleaning and they withstand high radiation density. However their QE at λ=266 nm is too low to make it competitive with metals photocathode. They can become interesting if future developments in optics lead to an efficient generation of wavelength around 200 nm.

5.5 Metal photocathodes

We measured the QE of two metals: copper and magnesium. The copper was commercial purity material and the Mg samples were film deposited using two techniques: the sputtering and the pulsed laser ablation PLA [117].

Mg has been identified, since long time ago [118, 119] as a metal photocathode with relatively high QE, $\sim 0.5\%$. The features of efficiency, robustness, promptness and good emittance of bulk Mg have been investigated with a certain success within rf electron guns. Mg disks installed in rf-gun with the press fitting technique [120] had problems of RF breakdown at the joint between the Mg disk border and the Cu embedding structure. Frictional welding technique did not solve completely the breakdown problems [120] and the maximum electric gradient is limited at 110 MV/m [17]. Moreover the distribution of QE shows large variations over the spot irradiated by the laser [32]. This non uniform distribution causes a deterioration of the brilliance of the source [46]. In comparison, cathodes constituted by thin films are expected to present a better emission uniformity and a lower discontinuity at the border. With the aim of obtaining tightly bounded films with optical finish surfaces to overcome those problems we prepared Mg photocathodes with the pulsed laser ablation technique (PLA) and tested Mg film obtained by sputtering technique.

Film preparation

The sputtered films were deposited onto copper substrates material that are used to build the rf guns. Prior to sputtering with Mg, the copper substrates were cleaned by ion bombardment. A 20 mm thick layer of commercially pure Mg was then ion sputtered (Koral Labs., Inc. MN) on to copper in a system pressure of $2{\cdot}10^{-7}$ Torr. The coated substrate was then shipped in a sealed container filled with Nitrogen. During installation into our test chamber, the samples were briefly exposed to the ambient air.

The PLA films were obtained by deposition of material ablated by a pulsed laser beam of 308 nm wavelength, delivered by an excimer laser. The 1 μm Mg films were covered with a 20 nm graphite thin layer with protective purpose. This cathode arrangement made the cathode of safe maintenance and easy handling. The Mg bulk target where the laser beam was focused rotated at a frequency of 1 Hz. The impinging angle of the light beam with respect the target surface was 55°. The target was arranged as a cylinder with a 12 mm diameter graphite, inner core fitted within a the high purity Mg (25 mm external diameter). This special target configuration allowed us to perform the deposition of the Mg film and in succession (within a unique process) the protective graphite coating. In fact, the laser beam was first launched onto the Mg external ring and in succession onto the graphite core by a simple small rotation of the target. The depositions were performed at laser fluences between 6 and 10 J/cm^2 inside an high-vacuum chamber

set at 10^{-6} Pa pressure. For the substrate we used the oxygen free copper because in a rf-gun the cathode is bonded on this kind of metal. During the deposition the distance between target and substrate was set at 4.5 cm.

The characteristics of the deposited film depend on the ablation rate, the plume deflection and the morphological changes of target surface created by prolonged laser irradiation. The right set of parameters for a compact and smooth film was chosen via systematic tests on the result with different apparatus arrangements. In order to deposit one Mg film, $3{\cdot}10^4$ subsequent laser pulses were applied. Then, $2{\cdot}10^3$ more laser pulses were applied to deposit a thin layer of graphite. Before each successive deposition run, the target surfaces were cleaned by applying $5{\cdot}10^3$ and $1{\cdot}10^3$ laser pulses for Mg and graphite, respectively. During these cleaning processes, a shutter was interposed between the target and the Cu substrate to avoid the deposition of the ablated material from the first layers of the targets, which are the most contaminated.

5.5.1 Mg film photocathode

The measurement for the metal PC ware performad in UHV (pressure less than $5{\cdot}10^{-8}$ mbar) with an extracting electric field of 1MV/m. The measurement were done after the laser cleaning procedure. For the ablation of superficial contaminants in copper and sputtered Mg and the protective graphite layer in PLA Mg a laser cleaning technique was developed.

The laser was focused by 60 cm lens into a spot with diameter of 0.3 mm corresponding to a peak power density of about 4 GW/cm^2 and was scanned over the cathode area. The scanning was realized by controlling a gimbal mirror with two DC motors. The control software developed in Labview environment allowed to set the an independent movement in x and y, and read as feedback, the centroid position from a CCD camera focused on the virtual cathode. Because the wavelength response of the camera is limited between about 350 nm and 850 nm it was used a 100 μ m Ce:YAG scintillator film ($Y_3Al_5O_{12} : CeO_2$ 0.15%), that adsorbs the UV radiation and emits in the visible wavelength at 550 nm, with a decay time constant of 70 ns [121]. Portion of the beam is split using a beam splitter (BS) at 45°.

To find the operating condition to perform an effective laser cleaning, we measured the temporal waveform of the emitted charge by the oscilloscope. In fact with the extracting field applied it is possible to determine the laser power density that starts the formation of the plasma and therefore the removing of surface contaminants. In this case the ablated positive ions from the cathode surface cancel the effect of the space charge saturation and the electron temporal duration, that in normal condition is as long as the laser pulse, lengthen up to hundreds of ns.

The laser cleaning resulted effective on the first copper cathode we tested. In this case the QE was increased by a factor 2 and the final value of $3{\cdot}10^{-6}$. The QE observed is more than a order of magnitude lower than what is

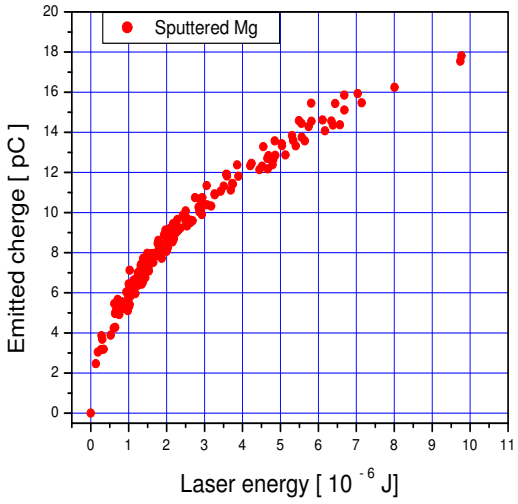

Figure 5.8: Sputtered Mg charge emission vs laser pulse energy at λ=266nm, E_{bias}=3kV and laser diameter equals to 1 mm, after the laser cleaning treatment.

reported in literature because of the poor quality of the copper tested.

In fig 5.8 is reported the emission charge of the sputtered Mg film after the laser cleaning with 1500 shots of energy of 100 μJ and focused on 0.3 mm diameter spot. After the laser treatment the laser beam diameter was then enlarged to 1 mm to occupy the scanned area. The QE measurements were made with much lower power densities to reduce space charge saturation and an accelerating electric gradient of 1 MV/m. The saturation is visible from the bending of the emitting curve. In theory the curve should be linear because the photon energy is larger that the Mg work function (4.3 eV). The correct estimation of the QE must be done at lower charge value by linear fitting in this case we can state that the QE is larger $5{\cdot}10^5$. To have a better estimation the energy measurement resolution should be increased or the saturation effect should be reduced by enlarging the laser spot size.

The fig 5.9 shows the tens nm resolution, superficial morphology analysis performed with atomic force microscope (AFM) at the Dep. of Energetics at the University "La Sapienza" in Rome. The picture indicates good crystallinity structure, it's clear the hexagonal borders of the Mg crystals. The AFM analysis show that less than 0.6 μm has been removed by laser cleaning treatment.

The emission from the PLA films before the laser cleaning is dominated by the graphite protective layer, see fig. 5.10. After the laser removing of the superficial layer, (with 5,000 laser pulses of 100 μJ=mm^2), the QE shown an huge increase. Because of the high density charge emitted the plot is dominated by saturation effect.

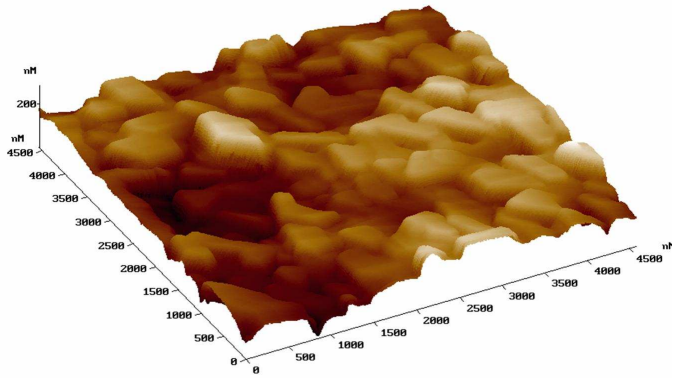

Figure 5.9: AFM Analysis on sputtered Mg surface after the laser cleaning treatment.

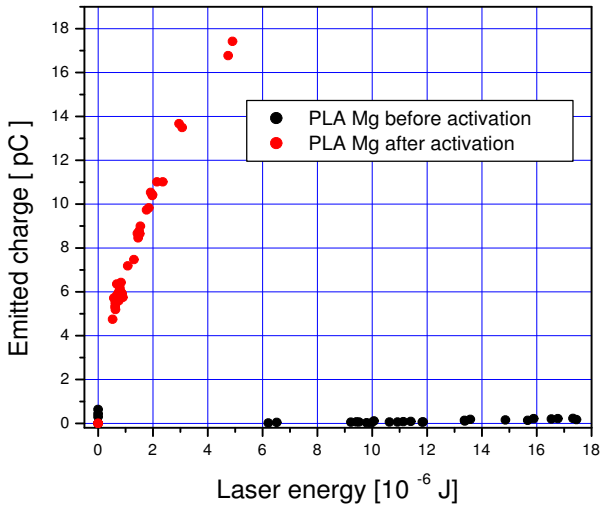

Figure 5.10: PLA Mg QE before and after the laser activation at λ=266nm, E_{bias}=3kV and laser diameter equals to 1 mm.

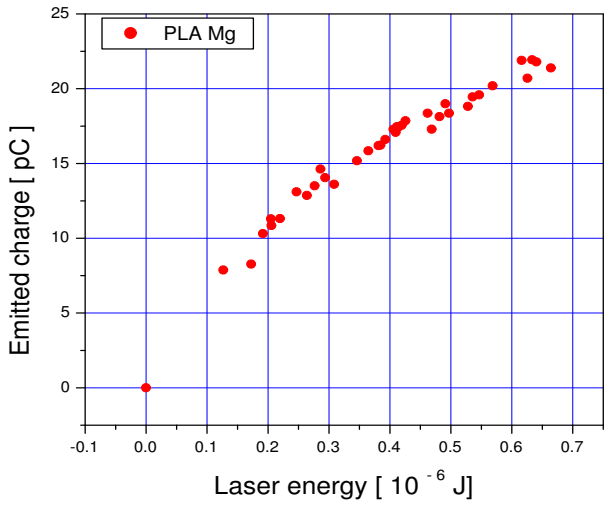

Figure 5.11: PLA Mg charge emission vs laser pulse energy at λ=266nm, E_{bias}=3kV and laser diameter equals to 2 mm, after the laser cleaning treatment.

To increase the QE resolution we increased the resolution of the energy measurement devices and enlarged the laser spot size to 2 mm at the cathode.The quantum yield measured was $4{\cdot}10^{-4}$ as shown in fig. 5.11.

A 20 nm graphite film seems a completely efficient protective film even for long exposure to atmospheric pressure (we did not observed contamination after few weeks). It is a simple technique for conserving spare photocathodes at atmospheric pressure and therefore it allows an easy photocathode handling.

The measured QEs obtained for sputtered and PLA film at low dc field (1 MV/m) were less than that obtained with a sputtered Mg [94]. The first reason can be caused by resolution limits of our apparatus at high emitted charge density. Beside it is possible that the laser cleaning process produced micro-fractures on the Mg film. In this case the Cu substrate contributes with its lower QE to emitted current. Another explanation can be that the protective graphite layer has not completely removed. Finally we think that the lower performance of our PLA films compared with other published results could likely be due to voids in the crystallinity and to some MgO molecules which most likely form during the deposition process (the deposition was performed n moderate high vacuum and the presence of O_2 cannot be excluded). This conjecture is supported by structural analysis that points out the presence of nanometric MgO droplets and fragments on the surface spots irradiated for the laser cleaning. To understand better the result more morphological and composition analysis are required.

Anyway the results indicate the PLA Mg film as a very efficient pho-

toemitter. Moreover the measured yield is of high interest because an order of magnitude enhancement is expected at the high fields of rf-guns. The emission uniformity and film adhesion on the substrate should be verified with more systematic measurements. The effect of high accelerating field requires test directly in an rf-gun.

Chapter 6

High peak current production by magnetic chicane compressor

6.1 Introduction

The electron beam brightness is proportional to the beam peak current and inversely dependent on the transverse emittance. In the previous chapters we discussed the key issues to obtain very low emittance. Here we discuss the techniques to increase the beam current. In particular we report the activities done on a magnetic chicane compressor installation and simulations.

The compression experiment is under development at the Accelerator Test Facility (ATF) of the Brookhaven National Laboratory [122]. To achieve the electron beam compression a magnetic chicane has been installed downstream the linear accelerator of the facility.

The ATF is a users photo-injector facility based on a 1.6-cell RF gun working at 2856 MHz, which serves as an injector into the two consecutive 3 meter long, SLAC-type linear accelerating structures. A frequency quadrupled Nd:YAG drive laser produces 10-15 ps spatial uniform pulses at 266 nm, of up to 30 μJ energy. The quantum efficiency of the magnesium cathode stays well above 10^{-3} electrons per incident photon, allowing generation of electron beam bunches up to 2 nC in charge. A cathode laser cleaning procedure was developed at ATF to periodically remove cathode contaminants and maintain the high QE level.

The peak RF field at the cathode surface is typically about 100 MV/m, which allows generation of high brightness 4-5 MeV beam out of the gun. A pair of emittance compensation solenoids focus the beam into the linac. The linac exit energy is in excess of 70 MeV. A 30 MW Triton 8840 klystron tube allows to achieve the required gradient in the in the accelerating structures.

In the picture 6.1 is reported the plan of ATF accelerator and the experimental beamlines.

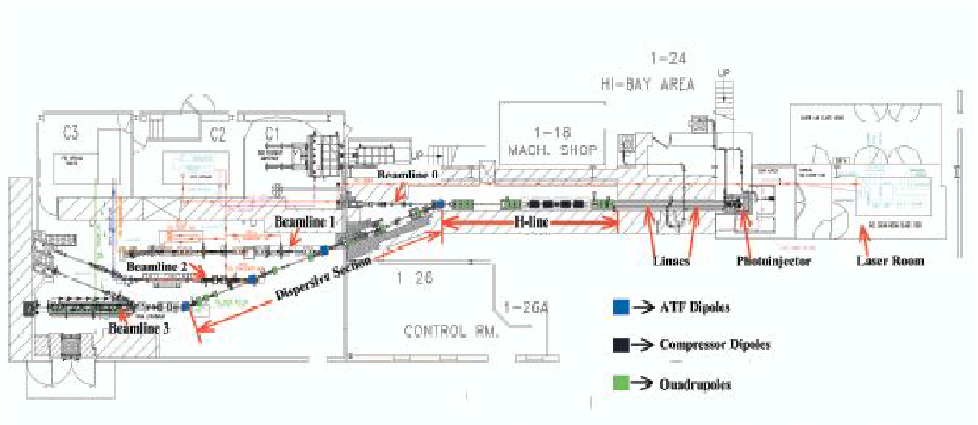

Figure 6.1: ATF layout including the laser rooms. the accelerator bunker and the experimental hall.

6.2 Magnetic chicane compressor techniques

One of the most straight forward methods to significantly increase the beam brightness is by shortening or compressing the electron beam longitudinally, and therefore increase the peak current. The bunch compressor can be accomplished by variety of techniques. Pulse compression ratios in the 2-5 range are common. Extreme pulse compression using non-linear dispersion chicane have been measured and give compression ratio approaching 40 [123].

Velocity bunching is an effective compression method and it is based on a position phase-energy correlation in the electron beam. This correlation can be introduced by the accelerating radio frequency field at a phase far for the sinusoidal crest. In this scheme the head of the beam is accelerated less that the tail producing a gradient of the velocity and therefore the charge is longitudinally compacted. For instance RF electron gun can be and usually are phased to achieve pulse compression. At high energy velocity bunching should be implemented using dedicated and nontrivial dispersive schemes [124].

In this work we will focus on the magnetic compression techinique and we will describe the magnetic chicane compressor that has been installed in the ATF facility within the activities done for this thesis.

Magnetic pulse compression can be achieved by arranging two conditions to be met:

- the beam must have a appropriate phase-energy correlation;
- particle at the head of the bunch must take longer path than those at the tail.

The scheme resembles the technique used for laser pulse compression, where frequency chirped pulses are compressed by two parallel gratings. This

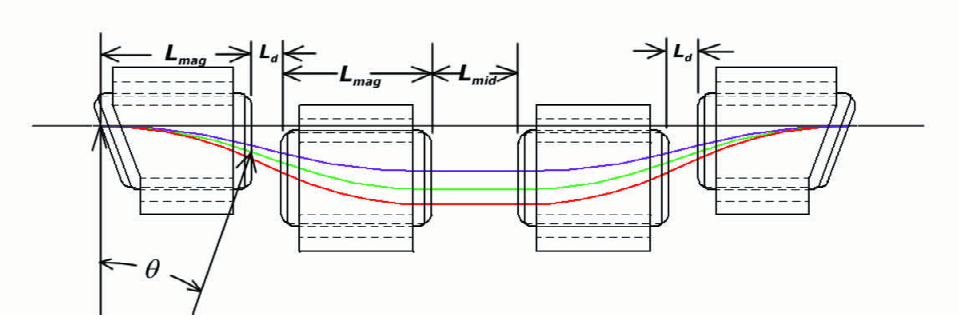

Figure 6.2: Representation of varying paths within a chicane compressor system. The middle green path is the design trajectory and the upper red and lower blue paths represent the low and high energy portions of the beam, respectively.

system introduces an optical path function of the wavelength and that delays the leading wavelengths respect to the tail wavelengths.

Three magnet configurations are commonly used to achieve group velocity dispersion for the electron beam: 180° non-zero momentum compaction arc scheme [125], a chicane [126] and modified dipole called an "α-magnet" which bends the beam at 270 ° and it is generally limited at low energy.

However, without exception, all the above configurations utilize a longitudinal energy correlation imparted on the beam to effect the final longitudinal distribution and it is not uncommon for the various compression methods to affect the quality of the electron beam during the compression process. In the Fig. 6.2 is represented how in the dispersive chicane the compression occurs. The magnets generate correlations between the energy and transverse positions of a particular particle within a bunch, consequently spreading out (dispersing) the beam transversely, according to the Lorentz law. This correlation is mediated by an additional correlation between the longitudinal position and energy for a particle imparted off-crest acceleration in the linear accelerator. In essence, since particles of differing energies traverse different radii under the influence of identical dipole magnetic fields, a notable increase in the transverse beam dimension is observed within this portion of the system. Theoretically for linear models of chicane compressors, this transverse beam size increase is naturally eliminated at the exit of the system. However, for real systems that are influenced by non-linear forces such as space charge, coherent synchrotron radition (CSR) or interactions with significant higher order multipole fields, a residual dispersion will exist which must be minimized, if not cancelled, in order to maintain beam quality.

The basic physics that underly this system can be understood by examining the path lengths that a particle i^{th} takes as it traverses the system (see the side view of the ATF chican in Fig. 6.2):

$$S(i) = 4R(i)\theta(i) + 2\frac{\cos\theta(i)}{L_d} + L_{mid} \tag{6.1}$$

From Eq. 6.1 we can derive the total change in particle position δZ, expressed in the transport matrix representation, for a bunch compressor to be:

$$\delta Z = R_{56}\frac{\partial p}{p} + T_{566}\frac{\partial^2 p}{p^2} + \dots \tag{6.2}$$

where $R_{56} = \partial(\delta Z)/\partial(\delta p/p)$ is the transport matrix element that maps the energy of a particle, p is the particle momentum, or an energy distribution onto its longitudinal position or distribution, for reference see [127]. For a bunch compressor with four equal length magnets this element is,

$$R_{56} \cong 2\theta^2\left(L_d + \frac{2}{3}L_{mag}\right) \tag{6.3}$$

Further, a second order term is included in equation 2.23, the T_{566}. This term is an element in the second order transport tensor and for a standard four dipole magnetic chicane bunch compressor configuration, can be calculated to be [128]:

$$T_{566} \cong -\frac{3}{2}R_{56} \tag{6.4}$$

Therefore, this contribution will always increase the amount of curvature already imparted on the beam by the RF wave from the linac.

The compression process comes at a price, however, of collective fields that may severely distort the vertical (y, bend plane) phase space. This distortion arises directly through transverse forces, or indirectly when a longitudinal force changes the electron energy during bending, giving rise to a subsequent trajectory error.

The operation that has been described should include also some effects that can limit the compression operation. We assumed the longitudinal distribution of the particles' momenta are linear with the position. Instead there are several factors that induce non linearity in the longitudinal phase space. For instance the curvature of the radio frequency produces a non linear momenta distribution versus the position. Besides the space charge fields can generate energy modulations. This is true especially for not flat current distribution. Moreover one should take in account eventual imperfections in the chicane construction that lead to asymmetry behavior. Finally there are some collective effects like the coherent synchrotron radiation and the wake-fields that contribute to alter the energy distribution within the electron bunch.

The chicane for its inherent nature based on bending and production of short charged bunch it natural tool to explore the CSR. In fact if this synchrotron radiation is emitted at wavelengths longer than the bunch length, the radiation from the individual particles will be emitted at nearly the same

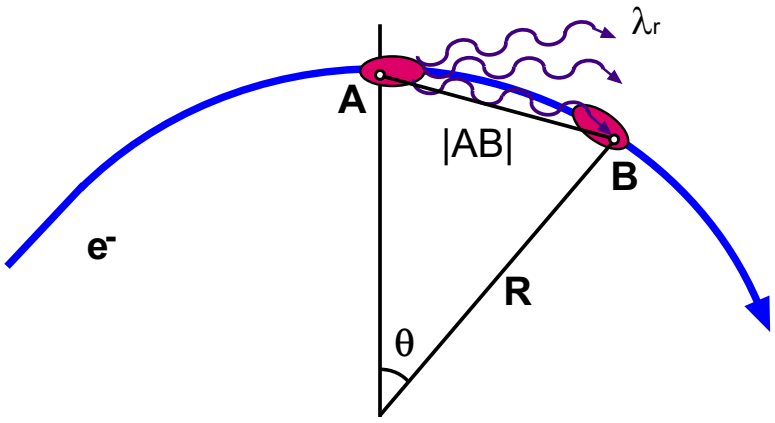

Figure 6.3: Geometric description for the visualization of the slippage length within a bending beam section.

phase and considered coherent. This coherent synchrotron radiation, first observed by Nakazato 1989 [129], will be emitted with an opening angle $1/\gamma$ and an intensity proportional to the square of the number of particle N within the bunch [130].

This is a significant increase over the N dependence of the intensity for incoherent synchrotron radiation, and the total steady state CSR power generated for a particular bunch length σ_z, bend radius ρ and angle θ is given by:

$$P_{csr} \propto \frac{N^2\theta}{\rho^{2/3}\sigma_z^{4/3}2\pi} \tag{6.5}$$

Additionally, this CSR power generated will experience an exponential drop off in the presence of the vacuum chamber for wavelengths greater than the shielding cutoff. In the case of the ATF compressor beam pipe geometry the cut-off can be expressed as:

$$\lambda_c \leq 2^{3/2}h\left(\frac{h}{\rho}\right)^{1/2} \tag{6.6}$$

h is the aperture size of the vacuum chamber modelled as a pair of infinite plate.

Further, the fundamental condition for the CSR emission to affect the beam can be understood by examining Fig. 6.3. Basically, the CSR emitted from the rear of the beam can effect the particles at the front of the bunch only if the CSR is emitted by particles less than a slippage length behind it. The slippage length is defined as the difference in length between the chord AB (that the radiation takes) and the path length along the arc from A to B (that the electron beam takes) as seen in Fig. 6.3. The particle is also known to radiate in a characteristic opening half angle $1/\gamma$ that set a limit to the cord length. This emission and absorption of the radiated energy then effects

the energy of the particle, which in turn affects the transverse position and angle of the particle upon exiting the system. Therefore, in the CSR emission regime, where the N^2 dependance of the energy applies, this can produce a notable effect on the transverse emittance. These energy changes may be so pronounced that a newly predicted microbunching instability develops [131, 144].

6.3 Accelerator Test Facility chicane compressor

To improve the performance of the ATF photo-injector in particular in term of peak current a magnetic chicane has been built (Fig. 6.4). The compressor has been installed into the high energy line after the 72 MeV linear accelerator [128] at the ATF . The chicane is composed of 4 dipoles and has been optimized to preserve as much as possible the emittance of the beam. The vacuum chamber has been design with two parallel pipes to operate the compression or to don't interfere with the beam dynamics. In fact it can allow two paths for the electrons: the straight one for normal operation and the bent path for beam compression. The first dipole works as a switch for select the two operation. The lower pipe has been designed with large vertical trajectories acceptance to allocate the spatial dispersed electrons. The middle of the chicane will be used for diagnostic purpose by inserting two scintillator screens into the two pipes.

The chicane will be used for the compression and for the measurement of the emitted coherent synchrotron radiation: in the Fig. 6.4 it is visible the radiation exit port. This measurement will be done with the aim to understand the properties of the emitted radiation and the effect it induces in the electron beam quality.

For the ATF compressor, $\delta p/p \cong 0.43\%$ and using Eq. 6.3 and 6.4 we can calculate that this T_{566} term is responsible for a path length difference of about 13.7 microns, a mere 3.8% of the R_{56} contribution. Therefore for the compressor the contribute of non-linear dispersion term has been minimized.

Further, the effects on the beam that are felt in the transverse phase planes can be uncoupled, in the linear approximation. For example, the vertical focusing can be understood by considering the relatively differing distances the particles interact with the magnetic field, depending on their vertical position within the bunch upon entrance and exit of the individual magnets. This can been seen when we examine what happens at the entrance/exit of a magnet as the particle enters/exits a dipole at an angle $\neq 90°$. According to the Fig. 6.2 the lower part of the electron beam experience a shorter interaction with the magnetic field and therefore leaves the magnet with a positive angle respect to the nominal trajectory, instead the upper part because of the longer interaction emerges with a negative angle.

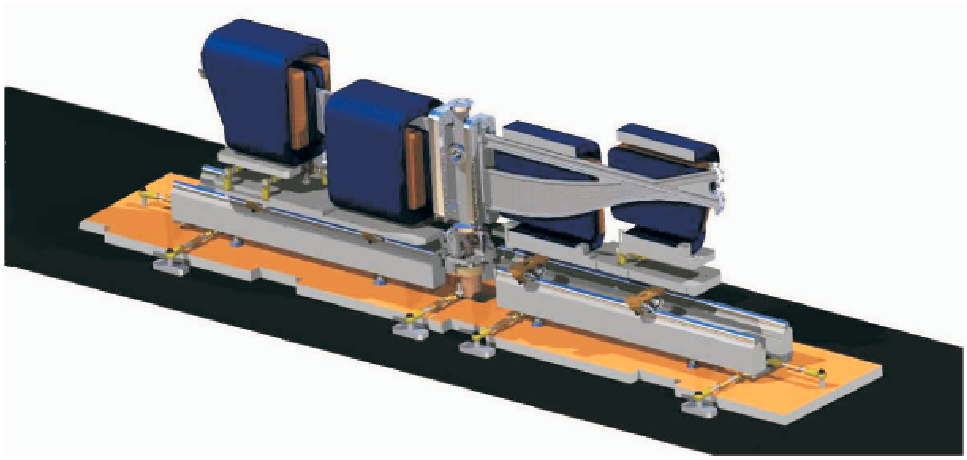

Figure 6.4: Rendered drawing of the chicane installed at ATF.

PARAMETER	VALUE	UNITS
B-field	2015	Gauss
Bend angle	20	degrees
Bend radius	1.2	m
Geometric length	41	cm
Magnetic length	44.7	cm
Magnet gap	2.1	cm
Nominal current	13.95	A
Current density	1.6	A/mm
Winding per coil	143	
L_d	8	cm
L_{mid}	24	cm

Table 6.1: ATF dipole magnet parameters

Additionally, the horizontal effects can be understood by examining what happens to a particle that enters the magnet at an angle other than normal to the poles. Essentially, the particle will experience a component of the fringe field which is normal to its trajectory that will cause a horizontally focusing or defocusing effect depending on the angle between the design trajectory and the pole face normal along with its horizontal position within the beam. The angles cut on the entrance and exit faces of the compressor system have been designed to optimize the focusing within the system. The design parameter for ATF compressor's dipoles are summarized in the table 6.1.

A systematic analysis of the expected compressor performance was undertaken. The numerical calculation have been carried-out using ELEGANT beam dynamics numerical code. The major feature of this code is that it includes the CSR computation in bending magnets and drifts. The CSR

	Before Compression	Output without CSR	Output with CSR	Units
RMS bunch length	400	25	24	μm
Peak current	50	1200	1700	A
Energy spread	0.4	0.4	0.4	%
Vertical ε_n	1.5	3.1	5.8	mm-mrad
Horizontal ε_n	1.5	1.5	1.5	mm-mrad

Table 6.2: Magnetic compression beam parameters according to ELEGANT simulations (courtesy of R. Augustsson)

calculations in ELEGANT are based on the 1-D line charge treatment of the electron beam in the thin layer beam approximation [133]. The input properties of the electron bunch are the nominal energy 72 MeV, the bunch charge 200 pC, the R_{56} =-9.27 cm and the T_{566}=1.53 cm. The input bunch length and the other input parameter have been evaluated with numerical simulation. Numerical simulations show that using the chicane one can increase the peak current in the electron beam by more than an order of magnitude without the need to use nonlinear properties of the dispersive section, see table 6.2.

As reported in the Fig. 6.5 the bunch length when enters in the chicane increases slightly and after an oscillation it reaches a very small value if compared with the input. The emittance is strongly effected by the CSR. In the plot on the left is evident the emittance envelope difference with and without the CSR.

Slice emittance analysis shown that the lower emittance in the beam is localized in the higher charge density region of the beam. If a band pass filter that cuts off the high and low energy portions of the beam is utilized, the majority of the core of the beam will remain, providing a high density and high quality beam.

Additional comment is that the overall output emittance even for the CSR case, is only 5.8 mm-mrad, and it corresponds approximately to 4 times increase. We recall that the definition of the electron beam brightness is inversely proportional to the transverse emittance, but directly proportional to the beam peak current. Therefore the degradation of the emittance in the y-plane is countered by the significantly greater gain in the beam current resulting in a higher brightness electron beam.

The ATF chicane has been installed and it is fully operating. In the next future it is foreseen to use the high brightness electron beam obtained to drive SASE-FEL VISA experiment that will be described in the next chapter. Preliminary simulation indicates that the saturation length with such beam quality can be achieved at 3/4 of the undulator length required for the saturation for uncompressed beam.

The second research field is focused on the study of the compression pro-

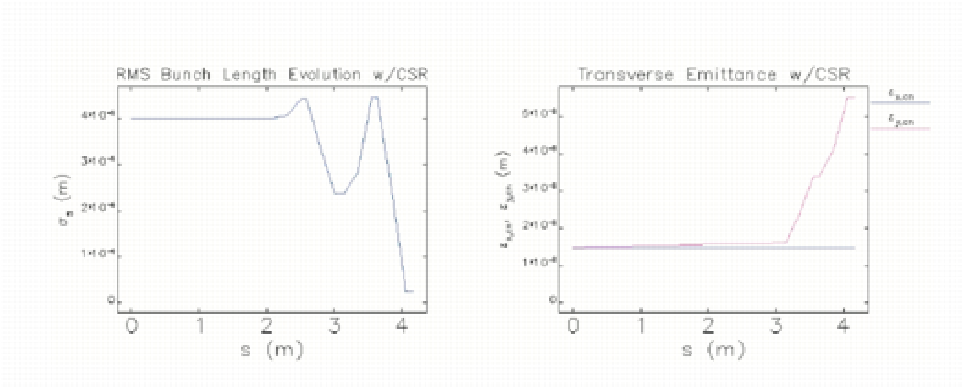

Figure 6.5: Simulated current and emittance results with ELEGANT CSR included.

cess itself by the measuring of the CSR emitted. For this measurement it is foreseen the use of a Helium-cooled silicon bolometer. This cold detector allows the roughly reconstruction of the spectrum irradiated. In fact the detector has a broadband spectral response in the far IR and for sub-millimetric wavelengths and it is provided by a spectral cut-on filters at 13, 27, 45, 103 and 285 μm. The emitted spectrum is related to the bunch length by the equation:

$$E(\omega) \approx E_0(\omega) N^2 \left(\frac{1}{Q} \int_{\infty}^{\infty} I(t) e^{i\omega t} dt \right) \tag{6.7}$$

The reconstruction of the CSR spectrum permits to define the rms bunch length. From the Eq. 6.6 it is possible to calculate the maximum emitted cutoff wavelength (h = 1 cm and ρ = 1.2 m) $\lambda_c \approx 1.8mm$. The presented simulations gave 6.2 the shortest bunch length expected that fixes the lower wavelength with coherent property.

The design and the installation of the optical transfer line has been concluded. The detector is placed at about 5 m from the chicane exit outside the linac bunker. The transfer line consists of 2 lenses with 125 cm focal length made with a special plastic, the picarin. This material has a broad spectral transmission up to sub-millimeter wavelengths. The radiation is steered by high quality gold coated mirror. Before the detector has been installed a 15 cm focal length parabolic mirror to focus the beam at the bolometer entrance. The detector's input port has a extra focal element obtained by a conic metallic waveguide called Winston cone.

The longitudinal electron beam diagnostics will be integrated with a coherent transition radiation (CTR) interferometer. This apparatus will be mounted downstream the chicane and allows to measure the bunch temporal features with a resolution of the bunch length. This diagnostic consists of a polarizing Michelson interferometer, [134], which analyzes coherent transition radiation emitted from the electron beams impact on a metal foil [135].

At ATF the benefits of the high peak current can be adopted also for other beam physics experiment for instance the plasma-beam interactions, laser beam interaction, wakefield acceleration and inverse Compton scattering.

Chapter 7

High bandwidth SASE-FEL experiment at VISA

7.1 Visa experiment overview

The concept of an unseeded, single pass, self-amplified spontaneous emission free-electron laser (SASEFEL) was introduced in early 80s [3, 7]. A series of successful experiments demonstrated high gain SASE operation, and agreement between the main elements of theory and experiments, in the IR [12], visible [19], and ultraviolet [136] spectral ranges. These results have led to the design of the Linac Coherent Light Source (LCLS) X-ray FEL project at SLAC [17] and similar project at DESY; which operation will significantly enhance research capabilities on the molecular and atomic level.

The VISA Visible to Infrared SASE project (VISA) [137], was designed to achieve saturation at 840 nm within a single-pass 4-m undulator.

The VISA SASE-FEL experiment is installed at the ATF facility. The AFT layout has been described in the previous chapter.

VISA experiment is located at Beamline III of the ATF experimental hall (see Fig. 6.1. Since ATF is a multi-user facility, a double-bend 20° dispersive section is used to share the beam between different beamlines. To deflect the beam to different experiments several dipoles are used. Past the dispersive section a matching quadrupole triplet is used in Beamline 3 to focus the beam into the VISA undulator.

The ATF electron beam for the VISA experiment is 1 nC charge to produce up to 200 A at 1.5 Hz repetition rate. The nominal energy is 72 MeV with energy spread of 0.18%. It is noteworthy to point out, that the beam of such brightness is the state of the art to drive a SASE FEL.

The original VISA-I experiment in 2001 demonstrated SASE high gain and saturation within 4-m undulator at 840nm [138, 137].

The VISA beamline is equipped with the multiple beam diagnostics. Faraday cups determine the charge right after the gun, at the dispersive section and in beamline 3. The basic beam quality measurements are performed

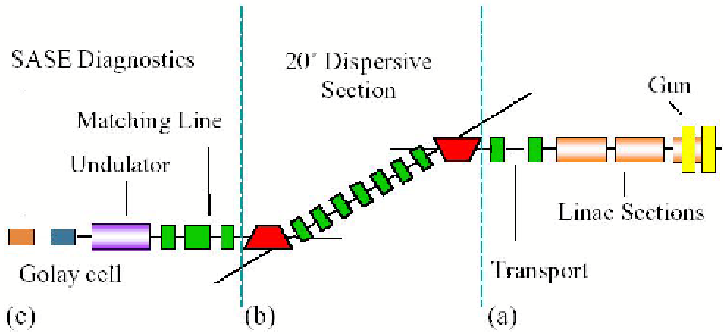

Figure 7.1: ATF beam line Experimental layout of the ATF Beam line III: gun and linac area (a); 20° double-bend dispersive section (b); and VISA experimental area (c), including the undulator and diagnostics.

at the linac exit. The quadrupole scanning technique is used to determine the electron beam emittance. The high energy slit in the dispersive section allows measurement of the longitudinal bunch profile and energy spread. The slit is placed after a bending dipole and determines the energy limits to send in the dispersive beam line. After the slit there is a scintillator and a CCD to analyze the energy distribution within the beam. Along the VISA beamline, almost after each magnet, there are several beam position monitor to measure the centroid and tranverse size of the beam.

The VISA undulator includes strong focusing magnets in both axis by a set of quadrupole with magnetic gradient of 33.3 T/m. The undulator period is 1.8 cm and undulator parameter is 1.26. The undulator frame has 4 independent solid segments, each 0.994 m long. The design on-axis field strength $B_0 = 0.75$ T is based on a Halbach array of $Nd_2Fe_{14}B$ permanent magnets and a fixed undulator gap of 6.0 mm. To decrease the beam size inside the undulator, a strong focusing scheme was implemented. Beside 8 magnetic steering magnet pair allow to control the trajectory in the undulator.

For the FEL experiment has been implemented a intra-undulator diagnostics system which (a) allow matching the beam trajectory and envelope into the undulator with the designed accuracy; (b) enable SASE radiation measurements throughout the undulator length.

The intra-undulator diagnostic allows, in 8 equal spaced position, to measure the trajectory of the electron beam and to extract the radiation. Along the undulator the growing extracted radiation is characterized in the angular distribution, in the spectral and in the temporal domain.

A double side 45° mirror is attached to the aluminum frame, and can be inserted into the beam path in 2 positions. In the outer position, the right side of the mirror intercepts the electron beam and generates optical transition radiation (OTR) for electron beam transverse measurement. The OTR signal is directed through an imaging optics located on the side of the

vacuum chamber into CCD camera. When probe is in the inner position, the SASE radiation can be reflected off the outer side of the mirror and transported towards the FEL diagnostics outside the vacuum chamber. The CCD is connected to a frame grabber system that allows the synchronization of the sensor and the acquisition of the measurement.

To achieve position measurement high accuracy first of all it is required the presence of the reference points; in this case it was natural to use an alignment HeNe laser as a straight line referenced. The laser is injected at the last dipole of the dispersive section.

The FEL measurements include intensity, spectrum and angular distribution of SASE radiation. Hence, it is desirable that one can multiplex between the spectrometer, joulemeter and CCD camera to measure various properties of the radiation coming out of any given diagnostic port. Considering the fundamental wavelength of 800 nm, the joulemeter of choice was Molectron J3S-10, a high sensitivity silicon detector with the dynamic range 0.2 pJ - 0.2 μJ. Near infrared coated lens is used to focus the beam into the detector window, and an iris in front of the lens controls the angular acceptance of the system. Due to the large range of measured intensities, a set of factory calibrated neutral density filters was used in front of the detector for high gain measurements.

For the CCD camera however, the two different approaches are taken. For the near field measurements, no lens is used, so the photon beam directly illuminates the CCD chip; the range of signal intensity was controlled with neutral density filters. On the other hand, for far field diagnostics of SASE angular distribution the camera is equipped with a lens and focused on a white paper target to which the photon beam is redirected.

For spectral measurement a fiber coupled spectrometer (Ocean Optics S2000) was used. It has 1.5 nm resolution, and dynamic range is between 350 and 1050 nm.

To bring the radiation from the 8 ports to only one diagnostic station a Fourier relay optics was used. With the lens focal distance choice of f = 50 cm, the radiation signal from each even port enters the lens array in the same phase. Remote controlled New Focus optical flippers are used to inject the beam into the lens array at the given location, which allows not to block the optical path when measurements at other ports are being performed. The same type of flippers were installed to multiplex between the spectrometer, joulemeter and a CCD camera at the diagnostic station.

7.2 Chirped beam SASE measurements at VISA FEL

With the prospects of the X-ray free electron laser (FEL) becoming a reality within the next decade, there is a great interest in a broader scientific com-

munity towards shortening the pulse duration of the anticipated X-ray FEL pulses down to 10-femtosecond range. For example, it would allow singular molecule diffraction experiments in the time interval shorter than it takes for the Coulomb explosion to destroy the sampled molecule [139]. Recently it was proposed [140] to use a chirped electron bunch to drive the self-amplified spontaneous emission (SASE) FEL so that the resulted SASE frequency modulation could allow separating single lasing spike from the rest of the bunch, or even using the optical gratings to longitudinally compress the X-ray beam. The limits associated with the chirped electron beam based SASE process have been studied theoretically and through simulations [141, 142], and one can approximately state, that the characteristic chirp value of interest is given by:

$$\frac{\Delta p}{p} \cdot \frac{\lambda_c}{L_c} \sim \rho \tag{7.1}$$

where λ_c and L_c are the FEL cooperation length [143] and the electron beam bunch length respectively, and ρ is the 3-D FEL parameter. The amount of electron beam chirp indicated in Eq. 7.1 is sufficient to separate individual spikes in time and frequency domain, while still preserving high gain SASE operation (which gain length generally increases with the higher uncorrelated energy spread).

The experiment at VISA-FEL has been conducted to demonstrate a proof of principle, that the efficient chirped SASE amplification is possible with the electron beam chirp value of interest as is indicated in Eq. 7.1.

To achieve high gain SASE lasing, an unusual bunch compression mechanism is used, utilizing nonlinear properties of the long dispersive section, see fig. 7.1, which is taking advantage of the large negative second order compression coefficient, that corresponds to the second order transport matrix's element T_{566}. The initial electron bunch (table 7.1) with the current of 55 A is compressed longitudinally up to the peak current of 300 A. The beam longitudinal compaction is obtained by manipulating the beam line tune settings, electron beam RMS linear chirp, σ_y, and central momentum offset of the electron bunch, Δp/p. In fact the pulse length variation $\Delta\zeta$ can be related to the above quantities by the equality:

$$\Delta\zeta = \left(T_{566} \cdot \frac{\Delta p}{p} \right) \sigma_y \tag{7.2}$$

The typical energy chirp value to obtain a moderate compression was of the order of $\sigma_y \sim$0.17%, during previous experiment [137]. Even though such a compression process allowed obtaining short FEL gain length and corresponding studies of the SASE properties at saturation, it had significantly restricted controllability of the electron beam parameters.

On the other hand, in accordance with the Eq. 7.1, an electron beam chirp of about 2% is required to demonstrate chirped beam amplification of interest, which is an order of magnitude larger value than used during VISA-

	Setting A	Setting B
Charge Q	300 pC	300 pC
Beam Energy E	71.2 MeV	70.6 MeV
Horizontal emittance	2.1±0.2 mm-mrad	∼4 mm-mrad
Peak current	55 A	∼300 A
Sliced energy spread	0.05%	0.45%
FEL gain length	∼30 cm	∼20 cm

Table 7.1: Electron beam characteristics and FEL gain length measured without compression (A) and with compression (B).

I. The carried out experiments [144] optimized the beam line tune and beam running conditions to achieve SASE operation with the large chirp.

One of the challenges of running a strongly chirped electron beam through the ATF beam line is to control the size of the beam, through the dispersion section of the beam line. The chirped beam transmission through the beam line is controlled by the high-energy slit (HES), which is an adjustable collimator located at the beginning of the dispersive section. In the recent experimental round, the 500 pC electron beam (Fig. 7.2.a) has a 2.8% energy chirp after the linac exit, of which only 1.7% (330 pC) can propagate through the fully open HES (fig. 7.2.b). The compression process in the dispersive section is monitored by the Golay cell installed in front of the undulator to measure the coherent transition radiation (CTR) intensity [22].

When the beam central momentum is chosen to optimize the compression in the dogleg, the CTR energy is peaked. Then, by closing the HES one can determine the part of the beam that contributes to the compression process (Fig. 7.2.c). The start-to-end PARMELA-ELEGANT simulations reproduced the compression process as observed by the combined slit and Golay cell measurements showing that the bunch peak current enhancement can reach up to 300A. This peak is very short in duration (∼200 fs FWHM), containing only 25-30 pC of charge and the slice energy spread is 0.45% [145].

With such a current very high SASE gain is achieved, despite the large sliced energy spread and degraded sliced emittance in the compressed part of the beam. The average SASE radiated energy around 2 μJ was recorded, which is within the order of magnitude from the saturation level. We measured the physical characteristic of the SASE signal of the highly chirped beam. The far field radiation distribution was recorded with a CCD camera at 3 meters from the undulator exit. In fig 7.3 is reported the SASE signal grabbed by the camera, the inner spot is due to the HeNe alignment laser. The unusual spiral shape of the FEL radiation was very repeatable and the angle of emission is up to 2.1 mrad.

The spectrum of the FEL radiation (fig. 7.4) have ultra large width of up

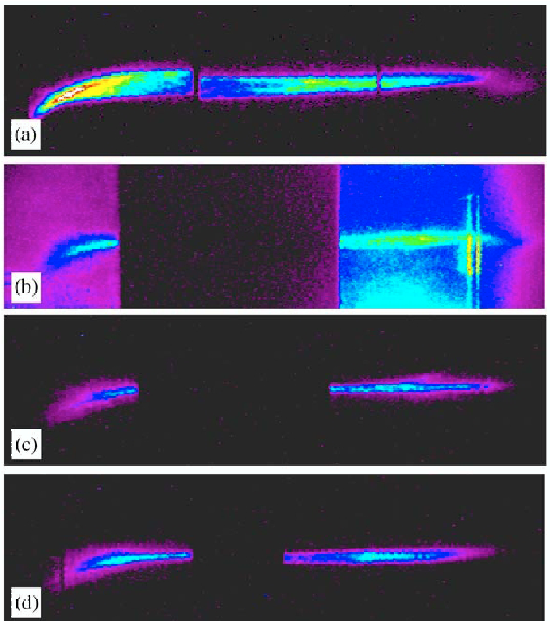

Figure 7.2: The chirped electron beam at the high-energy slit monitor: [a] closed slit (500 pC), 2.8% chirp); [b] fully open slit (60% transmission); [c] compressed fraction of the beam (1.5% chirp); and [d] the fraction of a beam generating a single SASE spike (0.8% chirp).

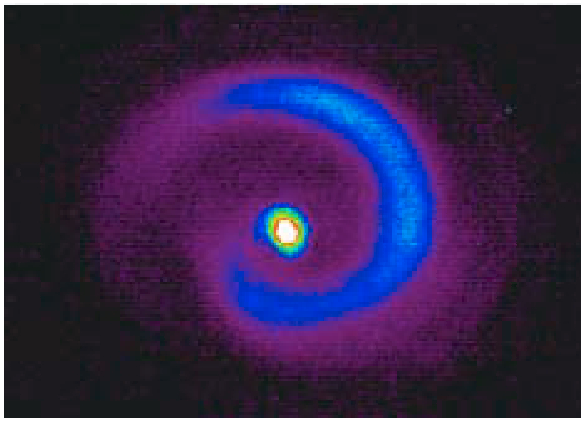

Figure 7.3: SASE far field angular distribution with HeNe reference laser.

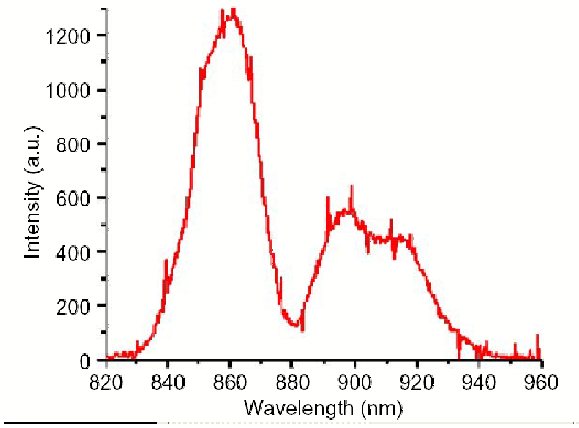

Figure 7.4: SASE spectrum with the chirped beam.

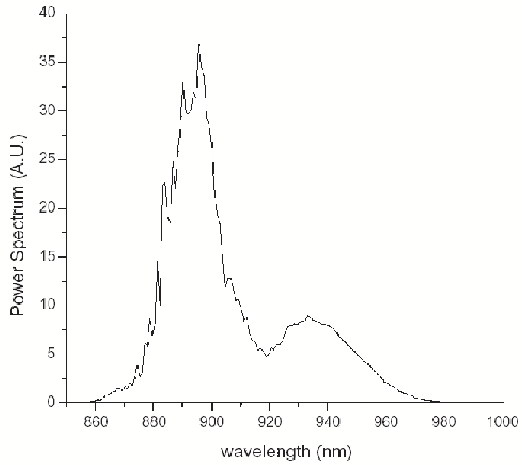

Figure 7.5: Wide FEL bandwidth experimentally observed is numerically reproduced (GENESIS Simulation)

to 10% of the central wavelength, and a characteristic dual spike structure, indicating two lasing modes.

It should be noted, that by closing the HES, one could eliminate one of the spectral spikes, without degrading the second spike intensity (in the condition reported in fig. 7.2.d), indicating longitudinal mapping of the SASE wavelength to the electron beam chirp.

Because the beam chirped is quite linear and only 60% propagates through the HES, the FEL performance becomes insensitive to the RF phase jitter and thus to beam misalignment after the bending dipole. In the reported large energy chirp regime, the same beam charge propagates through HES, regardless of the beam centroid jitter, thus making the lasing much more stable.

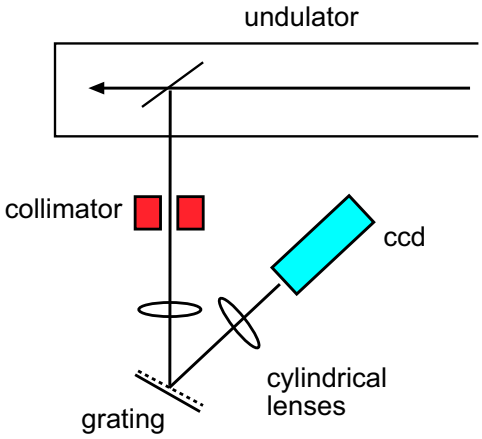

Figure 7.6: Set-up for the measurement of the near field intensity as function of the emitted angle and the spectrum.

Simulation performed with GENESIS were able to partially reproduce the spectral distribution experimentally observed [145]. In particular they reproduced the key facets of the observed spectrum, namely the large bandwidth and double spiked structure as shown in fig. 7.5. The simulations are consistent with the measurement when it is included the non-linear compression mechanism of the dog-leg. Because of these effects, the beam distribution at the undulator entrance also has a highly distorted distribution in the horizontal direction versus time configuration space. The shorter wavelength peak was very stable because it was produced by high current spike. The second, long wavelength peak is attributed to the amplification of a parasitic mode that is excited when the beam is off-axis in the undulator, the numerical calculation indicate a charge distribution up to 300 μm from axis. The calculation shows that the misalignment effect is in position and angle.

We recall that the emitted SASE-FEL wavelength is related observation angle by the equation:

$$\lambda_r \cong \frac{\lambda_u}{2\gamma^2}(1 + K^2 + (\gamma\theta)^2) \tag{7.3}$$

where λ_u is the undulator period, K_u is the undulator parameter and θ is the angle of observation respect to the axis of the wiggler. The emitted spectrum is broadened by three factors: the energy spread ($\Delta\gamma$), the off axis interaction of the beam with the focusing quadrupoles of the undulator, and the emission angle θ that takes in account the Doppler shift toward larger wavelength.

To relate the emitted spectrum with the radiation angular distribution we developed a diagnostics that is reported in the figure 7.6. The diagnostics consists of a collimator and a grating mirror. The collimator select 0.5 mm vertical slice of the SASE-FEL radiation. The grating mirror has 1200

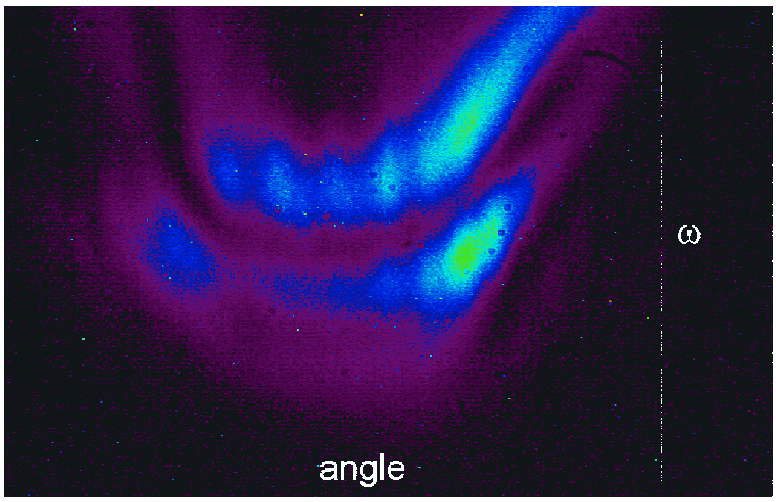

Figure 7.7: SASE intensity distribution vs the angle of emission (horizontal axis) and the spectrum (vertical axis) for the input chirped electron beam.

grooves per mm. Therefore the radiation shines the grating at 15° and it is reflected at about 50°. The two cylindrical lenses have a focal length of 5 mm in the horizontal plane. These optics are used to image the slit illumination on the grating and from the grating on the CCD sensitivity area. We didn't use objective lenses for the CCD but we sent the radiation directly on the silicon detector.

The grating disperses in angle the different components of the spectrum and in the vertical we obtained the angular distribution. For wavelength calibration we used Kr lamp that gives a series of spectral lines around 800 nm. In the Fig. 7.7 is reported the image recorded by the camera. The image is rotated because the camera has been mounted rotated by 90°.

As shown in the picture 7.7 the spectrum has a shift for larger angle. This result can be explained by Eq. 7.3. The double curve demonstrate a complex spectral structure and the presence of a parasitic mode from off-axis interaction in the undulator's field.

The results shown require more detailed analysis. It is under construction an optical diagnostic based on the FROG technique [59]. This measurement can help to reconstruct the temporal intensity and phase of the pulse.

We demonstrated the SASE-FEL operation of high chirped beam. The intrinsic layout of the ATF optics allowed an high compression. The unusual large bandwidth FEL radiation can be an useful tool for the future development of ultrashort FEL pulses.

Chapter 8

Conclusion

The aim of this work has been the study of the key issues for high brightness beam photo-injector for application in SASE-FEL experiment.

The drive laser is the first element of a photo-injector; we presented the study by beam dynamics simulations of its ideal parameters and their tolerances. The results are used for the definition of the laser system scheme for SPARC photo-injector. The optical transport from the laser to the cathode and the real time diagnostics has been also determined.

One of the most important feature to achieve very low emittance is the use of laser flat top temporal intensity with duration up to 12 ps. This pulse time profile has been obtained using an acousto-optics programmable dispersive filter. The device allows to modify the spectral phase and amplitude of the incoming pulse. The duration of the output pulse is limited to 6 ps by the finite length of the acousto-optic crystal. To produce longer pulse we used the filter in double passages configuration and in single pass with an additional external dispersive glass. This technique demonstrated the ability to produce the required temporal features: the rise time was shorter than 0.8 ps rms and the ripple below 20% peak to peak.

The acousto-optics filter have to pre-compensate the effect of the successive pulse manipulations. In fact the pulse manipulation devices has to be mounted upstream the amplification, the UV conversion and the transport to the cathode. We tested this configuration on the laser source at the Source Development Laboratory at the Brookhaven National Laboratory. Amplified pulse that are very close to the required intensity profile has been obtained. Further studies are going on to obtain the required pulse after the ultraviolet conversion.

One of the most critical component of the photo-injector is the photocathode. We studied the photoemission properties of poly-crystalline diamond film. We found a very repeatable high quantum efficiency behavior at low extracting gradient. The experimental results indicated that the photoelectric process is determined by the emission from not diamond C compounds between diamond and vacuum. The presence of the good crystalline diamond is important because it induces a negative electron affinity to the cathode.

This hypothesis has been confirmed experimentally with a large set of measurement. The diamond based photocathode quantum efficiency is $2 \cdot 10^{-5}$, a value too low for direct photo-injector application. This motivated the study of Mg film photocathode deposited by pulsed laser ablation (PLA) and sputtering techniques. To protect the PLA films we used a layer of 20 nm of graphite. This termination demonstrated the ability to avoid cathode contamination. We developed a laser cleaning procedure to remove the graphite and the oxides on the sputtered films. The results shown a quantum efficiency in excess of $4.7 \cdot 10^{-4}$ at an accelerating field of 1 MV/m. This value correspond to the maximum measurable quantum efficiency for the experimental apparatus. The emission uniformity and film adhesion on the substrate should be verified with more systematic measurements. The robustness to high accelerating gradient requires test directly in an rf-gun.

The study and the installation of the magnetic chicane compressor has been carried out at the Accelerator Test Facility (ATF) at BNL. The chicane has been studied with the aid of beam dynamics simulations which indicated that the peak current can be increased of a factor larger than 30. According to the simulations the emittance increase is only a factor 4. Therefore the compression should produce a net increase of the electron beam's brightness. In the next future the simulated results will be experimentally verified. The study and the implementation of an electron beam diagnostics and the CSR radiation measurement system have been carried out.

Finally we reported the measurement conducted at the VISA SASE-FEL experiment at ATF. We achieved high gain FEL with 2 μJ of radiated energy per pulse corresponding, one order of magnitude below the saturation energy. Simulation indicated that the SASE was driven by with high peak current up to 300 A distributed on very short duration about 200 fs. The compression was realized by propagation of a large chirped electron bunch (1.7% of the nominal value) in the ATF dispersive section. The compression induces non-linear correlation between the energy and the transversal position. We measured the radiated spectrum the angular distribution and the correlation between the two quantities. Driven by the chirped electron beam the SASE radiation showed very large bandwidth up to 80 nm and emission angle up to 2.1 mrad. The broad bandwidth is of interest for future generation of ultrashort FEL radiation. The spectrum is broadened by the amplification of a parasitic mode derived by off axis (300 μm)and off angle interaction in the undulator. This experiment required further studies to understand the mechanism of the high gain SASE process for the parasitic mode.

Appendix A

Addendum to section 4.4

The DAZZLER experiment at SDL has been extended also in the early months of 2005 with the aim to study the effect of UV conversion on the flat top IR profile and to observe the produced electron beam's properties. The good results in the near infrared, in fact, justified this further step. We replaced the second BBO usually employed with a thinner crystal of 100 μm to preserve all the bandwidth and to reduce the effect of phase mismatching along the crystal. In fact we have observed an increase of the modulation on the top of the harmonics due to phase mismatching.

For low resolution temporal measurements in the UV we used the ps streak camera and for the spectral domain characterization we employed the high resolution spectrometer. In the Fig. A.1 are compared the spectral intensities of the fundamental wavelength the second harmonic and the third harmonic when the DAZZLER filter is applied. To increase the resolution at second and third harmonics we used the second and third diffraction order of the spectrometer's grating. Therefore the wavelengths and the bandwidth of the blue and the UV spectra should be divided by two and three respectively. As shown in the Fig. A.1 the IR spectrum has a flat top distribution that according to the simulations corresponds to flat top time profile. The second harmonic shows a reduction of the relative bandwidth and an enhancement of the oscillations on the top. These observations can be explained by too thick second harmonic crystal of 1 mm. The third harmonic reproduces the 400 nm spectrum without a large bandwidth decreasing and the oscillations are not enhanced.

We approached the target profile by progressive reduction of the pulse's length. For 20 ps pulses we observed a cross-correlation trace with the same profile of the measured spectrum. This correlation has been lost when we compressed the pulse to 10 ps. In fact for flat top spectrum in the UV the temporal profile appeared almost triangular. Instead, for at the 800 nm wavelength the time and spectral intensity profile were very similar. The effect of the distortion can be caused only by phase order higher than the second that are likely produced within the chirped pulse amplification process. This effect is visible for the more compressed pulse when the relative contribution

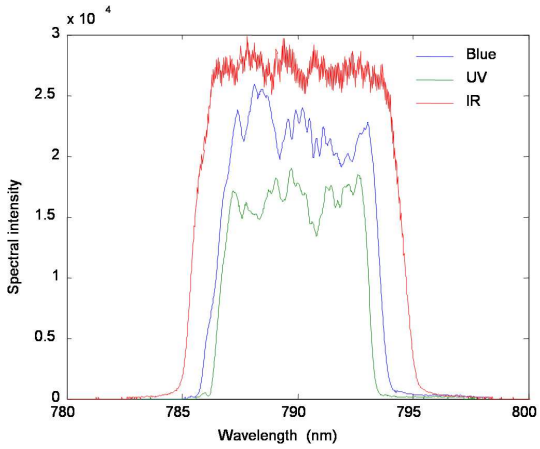

Figure A.1: Spectral intensities of the fundamental, the second and the third harmonic when the DAZZLER filter is used to produce the flat top profile.

of the second order phase term is reduced. The distortions have been limited by reducing the pump level for the regenerative amplifier to 10 mJ and by optimizing the compressor set-up. The higher order phase were introduced by non-linear phenomena in the amplification, like self phase modulation and by compressor aberration.

The main advantage of UV measurements is that, for this wavelength, it was available a temporal diagnostic with 150 fs resolution. This diagnostic is based on multishot cross-correlation of the UV pulse and the 100 fs IR oscillator's pulse. The two pulse overlap in a 100 μm thickness BBO non-linear crystal in non-collinear geometry. A delay line driven by a stepper motor, is used to shift the IR pulse in time respect to the UV one. The non-linear crystal is cut to produce the difference frequency of the input beams generating a pulse centered at λ=400 nm. The IR beam acts as a gate of the UV and the output reproduce the UV time profile.

The measurement of the emerging signal is performed with a fast photo-diode and a ADC connected to a computer. In general at each position of the delay line the cross-correlation is recorded for several pulses to calculate the mean and the standard deviation. In the Fig. A.2 is reported the UV cross-correlation trace of the experimental points with the relative error bars.

As shown in the figure the rise and fall time are about 1.1 and 1.5 ps and ripples are within 20% rms. The duration is about 7.5 ps but it would be quite simple to reduce the compression factor and to get 10 ps pulse. The first measurements appeared very promising. The cross-correlation has two drawbacks: it requires few minutes and the signal to noise is quite large because of the low energy for the IR pulse (few nJ). Therefore it not possible to have a fast and reliable optimization procedure.

To have a single shot temporal profile of the laser we measured directly the e-beam time distribution. The UV pulse obtained has been sent to the

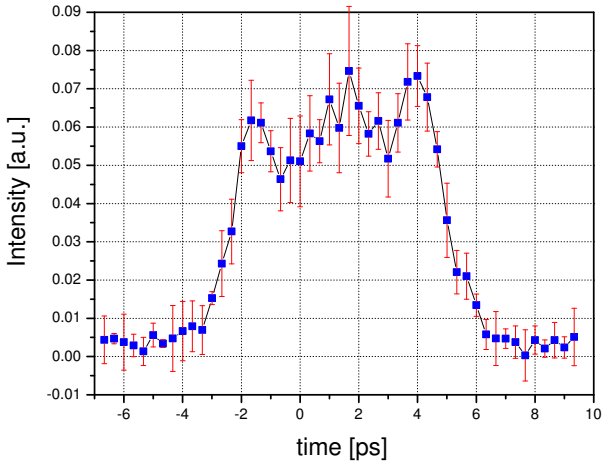

Figure A.2: UV pulse time distribution measured by cross-correlation technique with the relative error bars.

SDL photo-injector. The photoinjector consists of a copper cathode RF-gun with 5 S-band linac sections to achieve an energy up to 300 MeV.

The temporal distribution of electron bunch after the first two acceleration tanks has been measured using the RF zero-phasing method [146]. A large time-correlated energy spread (linear chirp) was induced on the electron beam by setting the phase of third or forth linac section to zero phase (non-accelerating). The beam was then dispersed by a dipole magnet where the different time slices of the beam travelled different trajectories and thus intercepted different positions on a scintillator screen. The electron beam diagnostic is single shot diagnostic and is more useful than the cross-correlation measurement as a feedback on the AO filter. In the figure A.3 is reported the energy distribution and therefore the temporal shape of the electron beam measured after the dazzler optimization. The beam charge was limited to 70 pC to limit the effect of the space charge forces. The energy distribution, that corresponds directly to the time profile of the e-beam shows a square distribution with well defined edges.

We performed also the measurement of the temporal distribution of 300 pC electron beam, see Fig. A.4. In this case the charge profile shows less sharp edges and in the central slice is concentrated a peak. This effect can be explained taking into account the larger space charge forces and the beam dynamic.

Preliminary measurements, adopting the quadrupole scan technique, indicated that the transverse projected emittance is reduced from 2 to less than 1.5 mm-mrad from gaussian profile to flat top one. This measurement requires detailed analysis but it is important to point out the trend in the

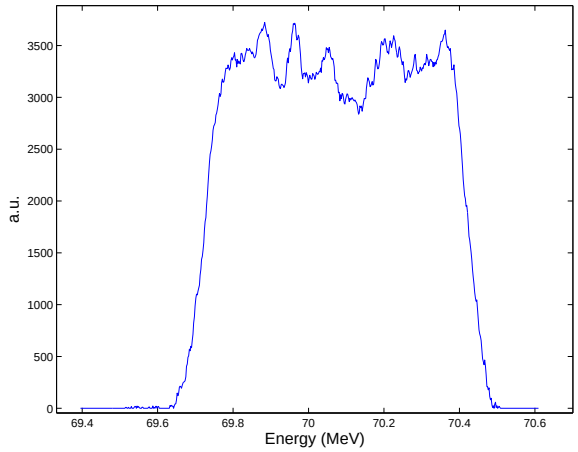

Figure A.3: Electron beam energy distribution after the zero phase acceleration and dipole dispersion

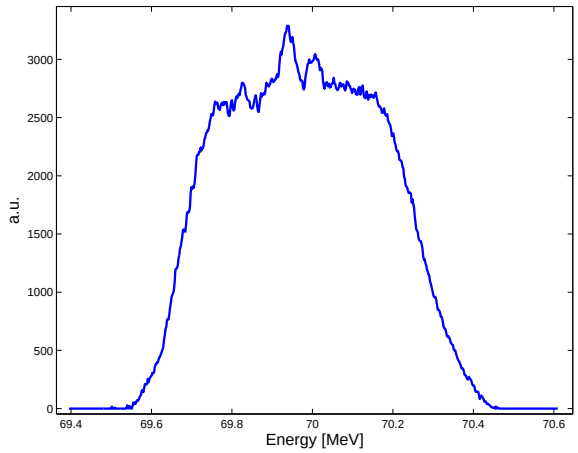

Figure A.4: 300 pC electron beam energy distribution after the zero phase acceleration and dipole dispersion

emittance reduction when the laser profile approaches the square distribution. In the measurements presented we employed the DAZZLER filter to perform only the amplitude modulation and in single passage configuration. The phase modulation can optimize the temporal profile especially if the filter is used in double passage set-up. This will be the object of future studies. The presented experiment can be considered successful but further improvements are required to generate the perfect high energy, square laser pulse, with all the properties that allows the minimum emittance.

Acknowledgments

First of all, I would like to express my deepest gratitude to the professor Luigi Palumbo who gave me the opportunity to work on the accelerator research and the SPARC project. He provided intellectual guidance for all the experiments. I would like also to thank Andrea Ghigo who has been always available for advices, discussions on physics and he was quickly getting into the essence of every problem. Franco Tazzioli deserves a special thank because he has guided me since I was an undergraduated student. Professor Jamie Rosenzweig offered me the opportunity to work in the VISA project and gave me useful suggestions and stimuli.

Marco Rossi and Maria Letizia Terranova gave me a great help in the cathode research program.

I have worked with many people who contributed to my work with suggestions and advices. Thanks a lot to Michele Castellano, Silvia Orlanducci, Massimo Ferrario, Simone Cialdi, Alessandro Cianchi and Luciano Catani.

I am grateful to have shared experiences at work and in the cold evenings in Long Island with Alex, Gerard and Ron from PBPL.

Other SPARC members, whose company made my PhD work a great experience are: Enrica Chiadroni, Marco Bellaveglia, Daniele Filippetto, Giancarlo Gatti, Massimo Petrarca, Rossano Sorchetti and Luciano Cacciotti.

Special thank should be extended to all the other people who work on the SPARC project for their guide to the all the young students.

Other people and laboratories contribution is most valuable for this thesis. For me it was an honor to work with several groups: the ATF team at BNL, the SDL group at BNL, the PBPL at UCLA and the researchers of the ULTRAS lab of the politecnico of Milan.

This work has been partly supported by Ministero Istruzione Università Ricerca, Progetti Strategici, DD 1834, Dec,4,2002.

I acknowledge also the support of the European Community-Research Infrastructure Activity under the FP6 "Structuring the European Research Area" programme (CARE, contract number RII3-CT-2003-506395)

Bibliography

[1] D. Alesini, C. Vicario et al., "Technical design report for the SPARC advanced photo-injector", *LNF report*, Frascati, April 2003.

[2] R. Sheffield, *Proc. AIP Conf. Phys. of Part. Acc.* , New York, (1989) 184.

[3] R. Bonifacio, C. Pellegrini, and L. Narducci, *Opt. Commun.*, **50**, (1984) 373.

[4] C. Pellegrini et al., *Nucl. Instr.&Meth. In Phys. Res. A*, **331**, (1993) 359.

[5] L. H. YU et al., *Phys. Rev. Lett.*, **64**, (1990) 3011.

[6] S. Reiche, *Nucl.Instr.&Meth.InPhys.Res.A*, **429**, (1999) 243.

[7] A.M. Kondratenko and E. L. Saldin, *Part.Accel.*, **10**, (1980) 207.

[8] J. S. Fraser et al., *IEEE Trans. Necl. Sci.*, **32**, (1985) 1791.

[9] B. E. Carlsten, *Nucl. Instr.&Meth. In Phys. Res. A*, **285**, (1989) 313.

[10] K.-J. Kim, *Nucl. Instr.&Meth. In Phys. Res. A*, **275**, (1989) 201.

[11] L. Serafini and J. B. Rosenzweig, *Phys. Rev. E*, **55**, (1997), 7565.

[12] M. Hogan et al., *Phys. Rev. Lett.*, **81**, (1998), 289.

[13] M. Babzien et. al., *Phys. Rev. E*, **57**, (1998), 6093.

[14] D. C. Nguein et al., *Phys.Rev.Lett.*, **81**, (1998), 810.

[15] M. Hogan et al., *Phys. Rev. Lett.*, **81**, (1998), 4867.

[16] A. Tremaine et. al., *Phys. Rev. Lett.*, **81**, (1998) 5816.

[17] "Linac Coherent Light Source (LCLS)Conceptual Design Report" *SLAC publication R593*, April 2002, UC-414.

[18] "Linear Collider Conceptual Design Report" *DESY print*, 97-48 (1997).

[19] S.V. Milton et al., *Science*, **292**, (2001) 2037.

[20] L.-H. Yu et. al., *Nucl. Instr.&Meth. In Phys. Res. A*, **445**, (1999) 301.

[21] J. Andruszkow et. al., *Phys. Rev. Lett.*, **85**, (2000) 3825.

[22] A. Murokh, et al., *Phys.Rev.E*, **67**, (2003) 066501.

[23] D. Alesini, C. Vicario et al., *Nucl.Instr.&Meth.InPhys.Res.A*, **507**, (2003) 345.

[24] R. Gomer, *Field emission and field ionization*, Harvard Univ. Press, Cambridge, (1961).

[25] W. A. Barletta et al., *Nucl. Instr.&Meth. In Phys. Res. A*, **250**, (1986) 80.

[26] C. Travier, *Proc. Short Pulse High current Cathode*, Ed. J. Le Duff, Bendor (1990).

[27] J.Adamaski et al., *IEEE Trans. Nucl. Scie.*, **5**, (1985), 2994.

[28] G. Suberlucq "Technological challenging for high brigthness photoinjector", *Proc. of EPAC − 2004*, Lucerne, July 2004.

[29] S. Schreiber et al. *Proc. of EPAC − 2002*, Paris, June 2002.

[30] J. Smedley et al. "Emittance measurements with a pulsed power photoinjector", *Proc. of PAC − 2003*, Portland, May 2003.

[31] C. Travier *Nucl. Instr.&Meth. In Phys. Res. A*, **340**, (1994), 26.

[32] D.T. Palmer, "The next generation photoinjector", Ph.D.Thesis, Stanford University (1998).

[33] M. Ferrario et al., *Proc. of ICFA Adv. Acc. Workshop*, "The Physics of High Brightness Beams", UCLA (1999), see also SLAC-PUB-8400.

[34] M. Ferrario et al., "Conceptual Design of the TESLA XFEL Photoinjector", *TESLA − FEL*, 2001-3.

[35] M. Ferrario et al., *Particle Accelerators*, **52**, (1996), 1.

[36] F. Ciocci, et al., "Insertion Devices for Synchrotron Radiation and FEL", *WorldScienti.c*, Singapore, 1980.

[37] P. Villoresi, *OpticsLetter*, **29**, (2004) 207.

[38] A. H. Compton, *Phys.Rev.*, **21**, (1923) 483.

[39] J. N. Bahcall, *Phys.Rev.Letters*, **12**, (1964) 300.

[40] D.A. Reis, Ph.D.Thesis, Univ. Rochester, Dept. of Physics and Astronomy, June 1999,UR-1573.

[41] A. Cianchi et al., *Proc.ofEPAC − 2004*, Lucerne, July 2004, 2622.

[42] C. Vaccarezza et al., *Proc.ofEPAC − 2004*, Lucerne, July 2004, 2616.

[43] S.G. Anderson, *Phys.Rev.Lett.*, **91**, 7, (2003) 074803.

[44] W. Koechner, *Solid State Laser Enginneering*, Springer-Verlag, Berlin, Heidelberg 1999.

[45] J.Yang et al., *J. Appl. Phys.*, **92**, (2002), 1608.

[46] M.Quattromini et al., "Spectral analysis of charge emission spatial inhomogeneities", *Proc. FEL Conference 04*, (2004),Trieste, Italy.

[47] F. Zhou et al., *Phys. Rev. ST Accel. Beams*, **5**, (2002), 094203.

[48] J. Billen, $LA - |UR$, **96**, (1996), 1835.

[49] M. Ferrario et al., *Particle Accelerators*, **52**, (1996), 1.

[50] L. Giannessi and M. Quattromini, to be published in *Phys. Rev. Spec. Top. Accel. Beam*, (2003).

[51] C. Rulliere, *Femtosecond Laser Pulse*, Springer-Verlag, Berlin, Heildeberg, 2000.

[52] J. C. Diels and W. Rudolph, *Ultrashort Laser Pulse Phenomena*, Academic, San Diego, Calif., 1996.

[53] C. Vicario et al., *Proc. Scie. World : Adv. Acc. Workshop Phys.*, Chia Laguna Sardinia, 2002.

[54] P. Maine et al., *IEEE J. Quant. Electr.*, **24**, (1988), 398.

[55] C. Le Blanc at al., *Opt. Commun.*, **131**, (1996), 391.

[56] M. Born and E. Wolf, *Principles of Optics*, Cambridge Univ. Press, Rochester, New York, 1999.

[57] P. Di Lazzaro et al. *Proc. SPIE*, **5120**, (2003), 150.

[58] J. A. Hoffnagle and C. M. Jefferson, *Appl. Opt.*, **39**, (2000), 5488.

[59] D. J. Kane and R. Trebino, *Opt. Lett.*, **18**, (1993), 823.

[60] C. Iaconis and I. A. Walmsley, *Opt. Lett.*, **23**, (1998), 792.

[61] V. Ayvaziyan et al., *Phys.Rev.Lett.*, **88**, (2002) 104802.

[62] A. Murokh, Ph.D. thesis, UCLA Dept. of Physics and Astronomy,(2002).

[63] A. Tremaine, et al., *Phys.Rev.Lett.*, **88**, (2002) 204801.

[64] C. Pellegrini, unpublished technote, 1999.

[65] C. Schroeder, et al., *J.Opt.Soc.Am.B*, **19**, (2002) 1782.

[66] S. Krinsky, Z. Huang, *Phys.Rev.STAB*, **6**, (2003), 050702.

[67] R. Bonifacio, et al., *Phys.Rev.Lett.*, **73**, (1994), 70.

[68] M. James et al., *IEEETrans.Nucl.Sci.*, **30**, (1983), 2992.

[69] F. Verluise and al., *Opt. Lett.*, **25**, (2000), 572.

[70] A. M. Wiener et al., *Opt. Lett.*, **15**, (1990), 326.

[71] A. M. Wiener and J. P. Heritage, *Rev. Appl. Phys.*, **22**, (1987), 1619.

[72] A. M. Wiener, *Rev. Sci. Instr.*, **71**, (2000), 1929.

[73] J. F. Nye *Physical Properties of Crystals*, Oxford Univ. Press, Oxford, 1957.

[74] A. Yariv and P. Yeh, *Optical Wave in Crystals*, Wiley, New York 1984.

[75] P. Tournois et al., *Opt. Comm.*, **140**, (1997), 245.

[76] F. Verluise et al., *J. Opt. Soc. Am. B*, **17**, (2000), 138.

[77] D. Kaplan and P. Tournois, *J. Phys. IV France*, **12**, (2002), 69.

[78] V. Voloshinov, *Opt. Engineer.*, **31**, (1992), 2089.

[79] N. Uchida and Y. Ohmachi, *Appl. Phys.*, **40**, (1969), 4692.

[80] A. Papoulis, *The Fourier Integral and Its Application*, MacGraw-Hill 1962.

[81] C. Vicario et al., *Proc. of EPAC 2004*, Lucerne, July 2004.

[82] L. M. Frantz and J. S. Nodvik, *J. Appl. Phys.*, **34**, (1963), 2346.

[83] W. Spicer and A. Herrera-Gómez, SLAC-PUB-6306, 1993.

[84] X.J. Wang et al., "Mg cathode and its thermal emittance", *Proc. EPAC 2000*, Vienna, June 2000.

[85] A.H. Sommer, *Photoemissive materials*, Robert E. Kreiger Publiching Company, N-Y 1980.

[86] E. Chevallay et al., *Nucl. Instr.& Meth. Phys. Res. A*, **340**, (1994), 146.

[87] I. Ben-Zvi et al., "Secondary emission enhanced photoinjector", *BNL − C − AP#149*, April 2004.

[88] S. Schreiber et al., "On the photocathodes used at the TTF photoinjector", *Proc. PAC 2003*, Portland, May 2003.

[89] H.H. Braun et al., "The photoinjector option for CLIC: Past experiments and future developments", *Proc. PAC 2001*, Chicago, June 2001.

[90] C. Ghosh and B.P. Varma, *J. Appl. Phys.*, **49**,(8), August 1978.

[91] S. I. Asinimov, V. A. Bendereskii, G. Farkas, *Sov. Phys. Usp.*, **6**, (1977), 20.

[92] 5. C. N. Berglung, W. E. Spicer, *Phys. Rev. A*, **136**, (1964), 1030.

[93] I. Boscolo, et al, *Opt. Comm.*, **187**, (2001), 179.

[94] T. Srinivasan-Rao, J. Schill, I. Ben Zvi, and M. Woodle *Rev. Sc. Instrum.*, **69**, 6, (1998), 2292.

[95] R. H. Fowler, *Phys. Rev.*, **38**, 45, (1931).

[96] L. A. Dubridge, *Phys. Rev.*, **43**, 727, (1933).

[97] J. H. Bechtel, *J. Appl. Phys.*, **46**, (1975), 1585.

[98] W. Schottky *Annalen der Physik*, **44**, (1914), 1011.

[99] J. P. & C. Girardeau-Montaut *J. Appl. Phys.*, **65**, (1989), 2889.

[100] E. R. Colby, Ph.D.Thesis, UCLA, Dept. of Physics and Astronomy, (1997).

[101] Muggli, R. Brogle, S. Jou, H.J. Doerr, R.F. Bushah, C. Joshi, *IEEE Trans. Plasma Sci.*, **24**, (1996), 428.

[102] L. Diederich, O.M. Kttel, P. Ruffieux, T. Pillo, P. Aebi, L. Schlapbach, *Surf. Sci.*, **417**, (1998), 41.

[103] F.J. Himpsel, J.K. Knapp, J.A. van Vechten, D.E. Eastman, *Phys. Rev.*, **20**, (1979), 624.

[104] J.B. Cui, J. Ristein, *Phys. Rev. B*, **60**, (1999), 16135.

[105] J.P.Dismukes *Synthetic Diamond*, Wiley, (1994).

[106] I. Boscolo, P. Michelato, *Nucl. Instr. & Meth. Phys. Res. A*, **445**, (2000), 389.

[107] M.L. Terranova, M. Rossi, G. Vitali, *J. Appl. Phys.*, **80**, (1996), 3552.

[108] J. Robertson, M.J. Rutter, *Diamond And Relat. Mater.*, **7**, (1998), 620.

[109] J. Robertson, *Mater.Res.Soc.Symp.Proc.*, **621**,R1.1.1 (2000),

[110] S. Orlanducci, C.Vicario et al., *Diam. And Relat. Mat.*, **12**, (2003), 2186.

[111] M.L. Terranova, et al., *Appl. Phys. Lett.*, **75**, (1999), 379.

[112] I. Boscolo, C.Vicario et al., *Appl. Phys A Mat. And Scie. Proc.*, **77**, (2003), 805.

[113] F. Tuinstra, J.L. Koenig 53, 1126 (1970) *J. Chem. Phys.*, **53**, (1970), 1126.

[114] R.E. Shroder, R.N. Nemanich, J.T. Glass, *Phys. Rev. B*, **41**, (1990), 3738.

[115] R. Saito, M.S. Dresselhaus, G. Dresselhaus, M.A. Pimenta and P.C. Eklund , "Raman Scattering in Carbon materials", edited by M.J. Pelletier *Blackwell Science Ltd.*, Chapter 9, (1999).

[116] A.C. Ferrari and J. Robertson, *Phys. Rev. B*, **61**, (2000), 14095.

[117] L.Cultrera, C. Vicario et al., *Proc. 4th Conf. ICPEPA*, September 2004 Lecce (Italy).

[118] T. Srinivasan-Rao, J. Fisher, T. Tsang, *J. Appl. Phys.*, **77**, (1995),1275.

[119] T. Srinivasan-Rao et al., *Proc PAC − 97*, **3**, (1997),2790.

[120] X.J. Wang at al., *Nucl. Instrum. & Meth Phys. Res. A*, **356**, (1995),159.

[121] M. Moszynski et al., *Nucl. Instrum. & Meth. Phys. Res. A*, **345**, (1994), 461.

[122] X. J. Wang, X. Qiu, and I. Ben-Zvi, *Phys.Rev.E*, **54**, 1996), R3121.

[123] B. Carlsten, *Nucl. Instr.&Meth. In Phys. Res. A*, **3**, (1996), 505.

[124] M. Ferrario L. Serafini, *Proc. ofAIP. Conf.*, **581**, (2001), 87.

[125] H.A. Enge, *Rev. ofSci. Instr.*, **34**, (1963), 285.

[126] M. James at al., *IEEE Trans. Nucl. Sci.*, **30**, (1983), 2992

[127] J. B. Rosenzweig. *Fundamentals of beam physics*. Oxford, UK: Univ. Pr. (2003).

[128] R. B. Agustsson, Master thesis, UCLA Dept. of Physics and Astronomy, (2004).

[129] T. Nakazato et al., *Phys. Rev. Lett.*, **63**, (1989), 1245.

[130] J.S. Nodvick and D.S. Saxon, *Phys. Rev.*, **96**, (1954), 180.

[131] S. Heifets et al., *Phys. Rev. ST Acc. Beam.* , **5**, (2002), 064401.

[132] S. G. Anderson et al., *Phys. Rev. Lett.* , **91**, (2003), 074803.

[133] E. L. Saldin et al., *Nucl. Instr.&Meth. In Phys. Res. A*, **398**, (1997), 373.

[134] U. Happek et al., *Phys. Rev. Lett.*, **67**, (1991), 2962.

[135] A. Murokh et al., *Nucl. Instr.&Meth. In Phys. Res. A*, **410**, (1998), 452.

[136] V. Ayvaziyan et al., *Phys.Rev.Lett.*, **88**, (2002), 104802.

[137] A. Murokh, Ph.D. thesis, UCLA Dept. of Physics and Astronomy,(2002).

[138] A. Tremaine, et al., *Phys. Rev. Lett.*, **88**, (2002) 204801.

[139] R. Neutze, et al., *Nature*, **406**, (2000) 752.

[140] C. Pellegrini, unpublished technote, 1999.

[141] C. Schroeder, et al., *J. Opt. Soc. Am. B*, **19**, (2002) 1782.

[142] S. Krinsky, Z. Huang, *Phys. Rev. STAB*, **6**, (2003), 050702.

[143] R. Bonifacio, et al., *Phys. Rev. Lett.*, **73**, (1994), 70.

[144] G. Andonian, C. Vicario et al., *Proceedings of PAC 2003*, Portland, April 2003.

[145] G. Andonian, C. Vicario et al., *Proceedings of FEL conf. 2004*, Trieste, August 2004.

[146] D. X. Wang, and G. A. Krafft, *Proc. of PAC 1997*, Vancouver, May 1997.